

# Multidimensional Multirate Sampling and Seismic Migration

Erik Stangeland Karlsen

MASTER'S THESIS IN  
PETROLEUM GEOSCIENCE



DEPARTMENT OF EARTH SCIENCE  
UNIVERSITY OF BERGEN  
NORWAY

JUNE 1, 2010



## **Abstract**

Seismic data are usually recorded in time and space on rectangular lattices. Seismic wave propagation is described by the wave-equation, which yields a Fourier spectrum with smaller bandwidth than the rectangular periodicity allows for. Using non-rectangular, multirate, sampling lattices, it is possible to sample only the points which corresponds to propagating waves. For 2D data this technique can sample the wavefield with half the data points without introducing alias. Seismic migration is the process of inverting the recorded wavefield in time to depth. The wavefield has circular bandwidth, which is also less than the rectangular periodicity allows for.

It is also shown that the linear and parabolic Radon transform have a bandwidth which is smaller than the rectangular periodicity.

Fourier filtering and seismic migration algorithms are modified and performed on multirate lattices. Gazdag phase-shift and Reverse Time Migration (RTM) are implemented with multirate sampling, which makes the calculations more efficient.



## **Acknowledgements**

First of all I wish to thank my supervisor Professor dr. philos Einar Mæland for always being available for help and for guiding me through this thesis.

I also thank my fellow students at the Department of Earth Science for meaningful discussions on the subjects.

Erik Stangeland Karlsen  
Bergen,  
June, 2010



# Contents

<b>1</b>	<b>Introduction</b>	<b>1</b>
<b>2</b>	<b>The Fourier Transform</b>	<b>3</b>
2.1	Definition of Sampling Grids and Lattices . . . . .	3
2.2	2D Discrete Fourier Transform on Rectangular Grids . . . . .	4
2.3	2D Discrete Fourier Transform on General Grids . . . . .	5
2.4	Calculating the 2D DFT on General Grids . . . . .	7
2.5	The Fourier Transform and Reciprocal Lattices . . . . .	8
2.6	Upsampling and Downsampling of Functions . . . . .	10
2.7	Multidimensional Discrete Fourier Transform . . . . .	11
<b>3</b>	<b>Some Special Cases</b>	<b>13</b>
3.1	Different Periodicity Matrices Covering the Exact Same Region . . . . .	13
3.2	Hexagonal Sampling . . . . .	17
3.2.1	Hexagonal Fourier Transform with Rectangular Output . . . . .	19
3.2.2	Assuming Hexagonal Periodicity in Fourier domain . . . . .	23
3.2.3	Hexagonal Filtering . . . . .	27
3.3	Special Sampling Patterns . . . . .	31
3.3.1	Quincunx Sampling . . . . .	31
3.3.2	Diamond Sampling . . . . .	32
3.4	2D Sampling and Filtering of a Signal . . . . .	34
<b>4</b>	<b>Seismic Waves</b>	<b>37</b>
4.1	The Acoustic Wave Equation . . . . .	37
4.2	Sampling and Aliasing . . . . .	38
4.2.1	Example of 2D Sampling . . . . .	41
4.3	Bow-Tie Filter and Sampling . . . . .	43
4.4	Filtering in $(k_x, \omega)$ -domain . . . . .	45
4.5	The Radon Transform and Slant Stacks . . . . .	47
4.5.1	The Linear Radon Transform . . . . .	49
4.5.2	The Parabolic Radon Transform . . . . .	52
4.5.3	Comments . . . . .	52

<b>5</b>	<b>Seismic Migration</b>	<b>55</b>
5.1	Seismic Migration by Extrapolation . . . . .	55
5.1.1	3D Seismic Migration . . . . .	58
5.2	Reverse Time Migration . . . . .	63
5.2.1	Stability of the RTM . . . . .	66
5.2.2	Hexagonal Sampling . . . . .	70
5.2.3	Synthetic Examples . . . . .	74
<b>6</b>	<b>Summary and Conclusions</b>	<b>83</b>
<b>A</b>	<b>Diagonalization of the Periodicity Matrix</b>	<b>85</b>
A.1	Smith Normal Form . . . . .	85
A.2	Solving the Diophantine Equation . . . . .	87
A.3	Diophantine Equations and Smith Normal Form . . . . .	88
A.4	Different Diagonalizations of the Same Matrix . . . . .	90
A.5	The Smith Normal Form in $n$ -Dimensions . . . . .	90
A.6	Bricklaying over Lattices . . . . .	92
A.7	The $n \times n$ Smith Normal Form Algorithm . . . . .	94
A.7.1	MATLAB codes . . . . .	95
<b>B</b>	<b>Voronoi Diagrams</b>	<b>99</b>
<b>C</b>	<b>Interpolation</b>	<b>101</b>
C.1	Fourier Interpolation . . . . .	102
C.2	Dirichlet Kernel . . . . .	105
	<b>Bibliography</b>	<b>107</b>



# Chapter 1

## Introduction

A signal  $s(t)$  is most often sampled by defining a constant interval between each sample,  $\Delta t$ , and a finite period  $T$ . Furthermore, the signal has a finite number of points  $N = T/\Delta t$ , and is given  $s_n = s(n\Delta t)$  for  $n = 0, 1, 2, \dots, N - 1$ . By the discrete Fourier transform (DFT) the signal is periodic, hence also the Fourier spectrum. This yields the Nyquist-Shannon theorem, which introduces a limit for  $\Delta t$ . To avoid alias this theorem states that a signal with maximum frequency,  $\nu_{\max}$ , should have sampling interval  $\Delta t \leq 1/(2\nu_{\max})$ .

2D and 3D functions or images are generally sampled by using 1D theory. When acquiring data rectangular periodicity is assumed. To avoid alias, the conventional approach is to apply the Nyquist-Shannon theorem for all variables. Many physical problems have a Fourier spectrum where another periodicity would be preferable. Choosing another periodicity than the rectangular, often result in lattices where the sampling points are not regularly spaced.

To find an optimal sampling geometry for a 2D or 3D signal without introducing alias, it is important to analyze the Fourier spectrum. If a non-rectangular sampling grid is chosen, the alias pattern becomes more difficult to analyze, there are Nyquist frequencies in other directions.

In this thesis the sampling on non-rectangular lattices will be referred to as multirate sampling. Important lattices often mentioned in the literature, the hexagonal and Quincunx lattice, will be treated.

Seismic waves are described by the wave equation which gives an effective bound for the Fourier spectrum, and conventional sampled seismic data is oversampled. Sampling the seismic data on non-rectangular grids can reduce the data points by a factor 2. If the processing algorithms can be implemented on these lattices it could also reduce the computation time.

Multirate sampling has many physical applications. Rattey and Lindgren (1981) shows that a hexagonal lattice is most efficient for sampling the Radon transform in tomographic imaging. Murphy and Gallagher (1982) shows that it can be used on Fourier and Fresnel digital holograms.

Woodward and Muir (1984a,b) present a summary of the hexagonal sampling lattices and constructs finite difference operators for 3D wave equation migration. They show that the hexagonal symmetry results in a more accurate 2D Laplacian than rectangular sampling, hence also the 3D paraxial wave equation. Woodward (1986) shows that a hexagonal lattice

allows for three-pass Stolt and paraxial migration.

Bardan (1989) presents a bandwidth of both the wavefield and the linear Radon transform, and suggests that a hexagonal sampling scheme would be preferable. The Peterson-Middleton theorem gives weaker sampling requirements than the Nyquist sampling and therefore a hexagonal recording spread would be preferable for acquisition (Bardan, 1997, 2008).

A final migrated image have circular bandwidth and Mersereau (1979) shows that regular hexagonal sampling for circular band limited signals are 13.4% more efficient. Gesbert et al. (2007) performed Kirchhoff migration on a seismic data set sampled hexagonally. Further modifying other known processing algorithms to such lattices may make the processing more efficient.

This thesis is arranged as follows.

Chapter 2 covers the 2D discrete Fourier transform (DFT) on general sampling grids, calculating the transform with fast Fourier transform (FFT) using the Smith normal form theorem, a matrix representation of sampling grids and lattices in more than 2D.

In Chapter 3, some examples of using different periodicity matrices, some specific sampling patterns which later will be used with seismic data and different algorithms for calculating the Hexagonal discrete Fourier transform are presented.

Chapter 4 presents an optimal sampling theory for seismic waves and 2D filtering. A bandwidth for the Radon transform used in tomography, the (geophysical) linear and parabolic Radon transform is presented.

Chapter 5 covers seismic migration and modifications of known algorithms for non-rectangular sampling grids. The Gazdag phase-shift and reverse time migration are performed on multi-rate sampling grids.

Finally, Chapter 6 offers some concluding remarks.

The appendix covers some important results on the Smith normal form, a brief overview of Voronoi diagrams and interpolation methods.

## Chapter 2

# The Fourier Transform

The 2D Fourier transform is a powerful tool for image processing and for solving partial differential equations. One of the major problems in the discrete case is how to choose the sampling grid. This chapter presents a matrix representation of sampling grids and defines the 2D discrete Fourier transform for general sampling geometries. Theory for upsampling and downsampling of functions are presented, and a generalization to multidimensional grids.

### 2.1 Definition of Sampling Grids and Lattices

When sampling a function in 1D the sampling points are given as a finite set of integers, denoted by  $\mathbb{Z}_N = \{0, 1, 2, \dots, N - 1\}$ . In 2D the Cartesian discrete grid with  $N_1$  samples in one direction and  $N_2$  in the other, can be given as the product of two finite sets,  $\mathbb{Z}_{N_1} \times \mathbb{Z}_{N_2}$ .

In 2D it is possible to define more general lattices for sampling than in 1D, since it is possible to rotate and skew the coordinate axes. A general sampling lattice can be represented by two linearly independent column vectors  $\mathbf{u}_1 = (a, b)^T$  and  $\mathbf{u}_2 = (c, d)^T$  for  $a, b, c, d \in \mathbb{Z}$ , where  $\mathbb{Z} = \{0, \pm 1, \pm 2, \pm 3, \dots\}$  is the set of integers. The sampling points,  $\mathbf{n}$ , on this grid can then be written as

$$\mathbf{n} = i\mathbf{u}_1 + j\mathbf{u}_2 = \mathbf{A} \begin{pmatrix} i \\ j \end{pmatrix}, \quad (2.1)$$

where  $i, j \in \mathbb{Z}$ . The vectors  $\mathbf{u}_1$  and  $\mathbf{u}_2$  generate a basis for a lattice. The span of two column vectors are shown in Figure 2.1.

The range of the matrix  $\mathcal{R}(\mathbf{A})$  is defined as the parallelogram from the vectors  $\mathbf{u}_1$  and  $\mathbf{u}_2$ . The points which are contained in this will be written as  $\mathbf{n} \in \mathcal{R}(\mathbf{A})$ . An observation from Figure 2.1 is that the sampling points inside one parallelogram have equivalents in another. The triangles here represent equivalent points, also called congruent points. They can be defined by using modular arithmetics. If  $\mathbf{x}'$  is a random point, its equivalent in the range of  $\mathbf{A}$  is given

$$\mathbf{x} = \mathbf{x}' \pmod{\mathbf{A}}, \quad (2.2)$$

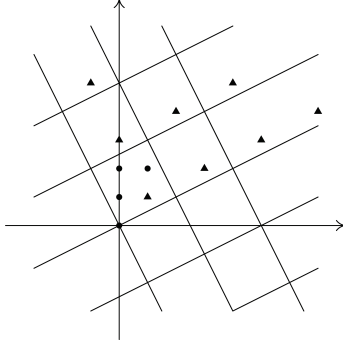


Figure 2.1: The range of a random matrix, the triangles represent equivalent sampling points

or more explicitly

$$\mathbf{x} = \mathbf{x}' - \mathbf{A} \lfloor \mathbf{A}^{-1} \mathbf{x}' \rfloor, \quad (2.3)$$

where  $\lfloor \times \rfloor$  is the “floor function” which gives the nearest integer towards minus infinity. This can be defined as

$$\lfloor \times \rfloor = \max\{n \in \mathbb{Z} | n \leq \times\}, \quad (2.4)$$

which will be used later when mapping from one lattice to another.

## 2.2 2D Discrete Fourier Transform on Rectangular Grids

The 2D discrete Fourier transform (DFT) of a function  $f = f(n_1, n_2)$  is given as

$$F(k_1, k_2) = \mathcal{F}[f] = \sum_{n_1=0}^{N_1-1} \sum_{n_2=0}^{N_2-1} f(n_1, n_2) e^{-2\pi i \left( \frac{n_1 k_1}{N_1} + \frac{n_2 k_2}{N_2} \right)}, \quad (2.5)$$

where  $n_1, k_1 \in \mathbb{Z}_{N_1}$  and  $n_2, k_2 \in \mathbb{Z}_{N_2}$ . This sampling grid can be given as  $\mathbb{Z}_{N_1} \times \mathbb{Z}_{N_2}$ , and defines a rectangular grid. Using vector notation, defining  $\mathbf{n} = (n_1, n_2)^T$  and  $\mathbf{k} = (k_1, k_2)^T$ , equation (2.5) can be written

$$F(\mathbf{k}) = \sum_{\mathbf{n}} f(\mathbf{n}) e^{-2\pi i (\mathbf{k}^T \mathbf{N}^{-1} \mathbf{n})} \quad (2.6)$$

where

$$\mathbf{N} = \begin{pmatrix} N_1 & 0 \\ 0 & N_2 \end{pmatrix}. \quad (2.7)$$

The range of the matrix  $\mathbf{N}$  defines the sampling grid. Figure 2.2 is an example of a rectangular

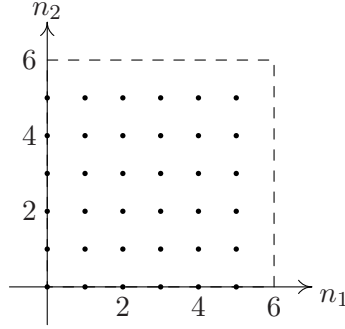


Figure 2.2: Example of rectangular sampling

sampling grid where  $N_1 = N_2 = 6$ . The exponential functions are orthogonal with respect to the inner product, given as

$$\sum_n e^{2\pi i(\mathbf{k}'^T \mathbf{N}^{-1} \mathbf{n})} e^{-2\pi i(\mathbf{k}^T \mathbf{N}^{-1} \mathbf{n})} = \begin{cases} \det(\mathbf{N}) & \text{if } \mathbf{k} = \mathbf{k}' \\ 0 & \text{otherwise} \end{cases}, \quad (2.8)$$

and the total number of samples is  $\det(\mathbf{N}) = N_1 N_2$ . This yields the inverse discrete Fourier transform (IDFT)

$$f(\mathbf{n}) = \frac{1}{\det(\mathbf{N})} \sum_{\mathbf{k}} F(\mathbf{k}) e^{2\pi i(\mathbf{k}^T \mathbf{N}^{-1} \mathbf{n})}. \quad (2.9)$$

There are several algorithms for computing these transformations, the most popular is the Fast Fourier Transform algorithm (FFT), presented by Cooley and Tukey in 1965. This algorithm can compute the transformation in  $\mathcal{O}(N \log N)$  operations whereas the naive implementation (summation) costs  $\mathcal{O}(N^2)$  arithmetic operations. The FFT is developed for 1D functions with equidistant sampling points, but for the 2D case with a rectangular sampling grid there has been developed an algorithm called Vector-Radix Fast Fourier Transform. This uses much the same rearranging of the samples as the 1D FFT, for more extensive treatment of this, see Dudgeon and Mersereau (1990).

### 2.3 2D Discrete Fourier Transform on General Grids

The range of the matrix

$$\mathbf{A} = \begin{pmatrix} a & b \\ c & d \end{pmatrix} \quad \forall a, b, c, d \in \mathbb{Z} \quad (2.10)$$

defines a general sampling grid. Sampling with this matrix, and using equation (2.9), gives

$$\begin{aligned}
f(\mathbf{n} + \mathbf{A}\mathbf{l}) &= \frac{1}{\det(\mathbf{A})} \sum_{\mathbf{k}} F(\mathbf{k}) e^{2\pi i(\mathbf{k}^T \mathbf{A}^{-1} \mathbf{n})} e^{2\pi i(\mathbf{k}^T \mathbf{A}^{-1} \mathbf{A}\mathbf{l})} \\
&= \frac{1}{\det(\mathbf{A})} \sum_{\mathbf{k}} F(\mathbf{k}) e^{2\pi i(\mathbf{k}^T \mathbf{A}^{-1} \mathbf{n})} \\
&= f(\mathbf{n})
\end{aligned} \tag{2.11}$$

for any vector  $\mathbf{l} \in \mathbb{Z} \times \mathbb{Z}$ . The function  $f(\mathbf{n})$  is periodic with period  $\mathbf{A}$ . This matrix is referred to as the periodicity matrix.

A similar argument can be made in Fourier space or dual space using equation (2.6), the periodicity is given

$$F(\mathbf{k} + \mathbf{A}^T \mathbf{l}) = F(\mathbf{k}). \tag{2.12}$$

This shows that using a general sampling grid  $\mathcal{R}(\mathbf{A})$  results in a sampling grid in dual space given by  $\mathcal{R}(\mathbf{A}^T)$ . If the matrix  $\mathbf{A}$  is diagonal, as in Section 2.2,  $\mathbf{A} \equiv \mathbf{A}^T$  and the periodicity are the same in both domains.

It is often convenient to move the sampling points to a rectangular period, for example to the Nyquist interval. This can be done with the simple coordinate transformation  $\boldsymbol{\kappa} = \mathbf{A}^{-T} \mathbf{k}$  and the periodicity becomes

$$\mathcal{R}(\mathbf{A}\mathbf{A}^{-T}) = \mathcal{R}(\mathbf{I}) \tag{2.13}$$

where  $\mathbf{I}$  is the identity matrix. An example of a periodicity matrix, its transpose and the coordinate transformation is given

$$\mathbf{A} = \begin{pmatrix} 3 & 2 \\ 1 & 4 \end{pmatrix}, \quad \mathbf{A}^T = \begin{pmatrix} 3 & 1 \\ 2 & 4 \end{pmatrix}, \quad \mathbf{A}^{-T} = \frac{1}{10} \begin{pmatrix} 4 & -1 \\ -2 & 3 \end{pmatrix}. \tag{2.14}$$

This sampling matrix has  $\det(\mathbf{A}) = 10$  data points, these are plotted in Figure 2.3. In Figure 2.3(c) the sampling points are not integer, this is a general problem and it is necessary with interpolation for plotting these images.

For a given periodicity matrix it is often possible to find another matrix which covers the exact same sampling points. In general, these sampling grids will have different periodicity in dual space, which results in a different image on the Nyquist interval. This because different sampling lattices yields different sampling of the transformation itself.

The 2D FFT can only be used when the periodicity matrix is diagonal, on rectangular periodic functions, but in the next section a method for calculating a 2D FFT on general grids is presented.

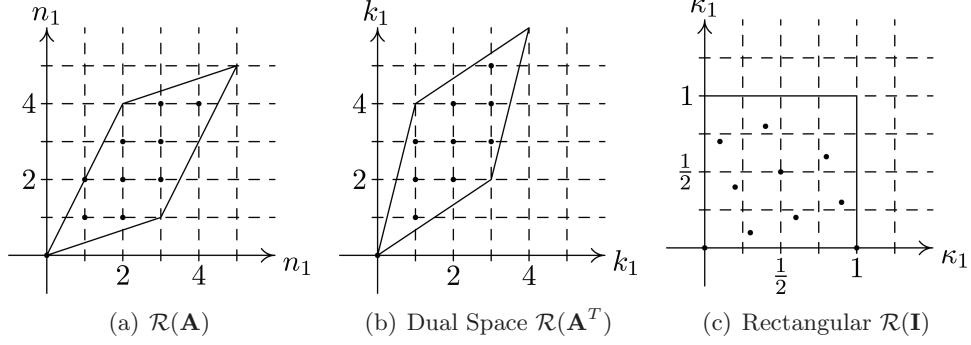


Figure 2.3: Dual sampling grids

## 2.4 Calculating the 2D DFT on General Grids

To calculate the discrete 2D DFT on a general grid the naive implementation would be to sum over the indexes in equation (2.6). Guessoum and Mersereau (1986); Bernardini and Manduchi (1994) suggests a method based on the Smith normal form theorem for integer matrices. Any integer matrix can be written as a product of three matrices where one is diagonal. The periodicity matrix can then be written as

$$\mathbf{A} = \mathbf{P}\mathbf{D}\mathbf{Q} \tag{2.15}$$

where  $\mathbf{P}$  and  $\mathbf{Q}$  are unimodular matrices,  $\det(\mathbf{P}) = \det(\mathbf{Q}) = \pm 1$ , and  $\mathbf{D}$  is diagonal. This and the Fourier transform from equation (2.6) yields

$$\begin{aligned} F(\mathbf{k}) &= \sum_{\mathbf{n}} f(\mathbf{n}) e^{-2\pi i(\mathbf{k}^T \mathbf{A}^{-1} \mathbf{n})} \\ &= \sum_{\mathbf{n}} f(\mathbf{n}) e^{-2\pi i(\mathbf{k}^T (\mathbf{P}\mathbf{D}\mathbf{Q})^{-1} \mathbf{n})} \\ &= \sum_{\mathbf{n}} f(\mathbf{n}) e^{-2\pi i(\mathbf{k}^T \mathbf{Q}^{-1} \mathbf{D}^{-1} \mathbf{P}^{-1} \mathbf{n})} \\ &= \sum_{\tilde{\mathbf{n}}} f(\tilde{\mathbf{n}}) e^{-2\pi i(\mathbf{Q}^{-T} \mathbf{k})^T \mathbf{D}^{-1} (\mathbf{P}^{-1} \tilde{\mathbf{n}})}. \end{aligned} \tag{2.16}$$

Defining the coordinate transformations

$$\Gamma_n : \tilde{\mathbf{n}} = \mathbf{P}^{-1} \mathbf{n} \quad \text{and} \quad \Gamma_k : \tilde{\mathbf{k}} = \mathbf{Q}^{-T} \mathbf{k}, \tag{2.17}$$

gives the Fourier transformation over a rectangular period defined by  $\mathcal{R}(\mathbf{D})$

$$F(\tilde{\mathbf{k}}) = \sum_{\tilde{\mathbf{n}}} f(\tilde{\mathbf{n}}) e^{-2\pi i(\tilde{\mathbf{k}}^T \mathbf{D}^{-1} \tilde{\mathbf{n}})}. \tag{2.18}$$

After the transformation  $\Gamma_n$  of the sampling points, it is possible to calculate the Fourier transform with the FFT algorithm, now being in a rectangular grid. Then the transformation  $\Gamma_k^{-1}$  maps the points to the dual lattice,  $\mathcal{R}(\mathbf{A}^T)$ . A schematic view of this process is given by

$$\mathbf{n} \in \mathcal{R}(\mathbf{A}) \xrightarrow{\Gamma_n} \tilde{\mathbf{n}} \in \mathcal{R}(\mathbf{D}) \xrightarrow{\mathcal{F}} \tilde{\mathbf{k}} \in \mathcal{R}(\mathbf{D}) \xrightarrow{\Gamma_k} \mathbf{k} \in \mathcal{R}(\mathbf{A}^T) \quad (2.19)$$

All these steps are readily inverted and the 2D DFT for functions with general periodicity can be calculated in both directions by FFT. There have been developed other methods for calculating fast 2D DFT for special grid geometries. For hexagonal sampling there is one algorithm mentioned in Dudgeon and Mersereau (1990).

Finding the Smith normal form and properties of it is presented in Appendix A, an algorithm for calculating the matrices implemented in MATLAB given in Appendix A.7.1.

## 2.5 The Fourier Transform and Reciprocal Lattices

A discrete sequence of samples of a 2D continuous function  $f_c = f_c(\mathbf{x})$ , can be written

$$f(\mathbf{n}) = f_c(\mathbf{V}\mathbf{n}) = f_c(\boldsymbol{\eta}), \quad (2.20)$$

where  $\boldsymbol{\eta} = (\eta_1, \eta_2)^T$  are discrete samples of  $\mathbf{x} = (x_1, x_2)^T$ . The matrix  $\mathbf{V}$  is called the sampling matrix, and for 2D

$$\mathbf{V} = \begin{pmatrix} a_{11} & a_{12} \\ a_{21} & a_{22} \end{pmatrix}. \quad (2.21)$$

If  $\mathbf{V}$  is a diagonal matrix it generates the conventional rectangular lattice.

When sampling a continuous function a finite period is assumed, given by the matrix  $\mathbf{T}$ , and the sampling points of the function are  $\boldsymbol{\eta} \in \mathcal{R}(\mathbf{T})$ . This matrix can be expressed

$$\mathbf{T} = \mathbf{V}\mathbf{A}, \quad (2.22)$$

where  $\mathbf{A}$  is the periodicity matrix with integer entries. The matrix  $\mathbf{A}$  is the one used with Smith normal form. This yields an expression for the sampling points of the continuous function

$$\boldsymbol{\eta} = \mathbf{T}\mathbf{A}^{-1}\mathbf{n}. \quad (2.23)$$

Using the exponent in the Fourier transform, equation (2.6), and the expression  $\mathbf{n} = \mathbf{V}^{-1}\boldsymbol{\eta}$ , yields

$$\begin{aligned} 2\pi\mathbf{k}^T\mathbf{A}^{-1}\mathbf{n} &= 2\pi\mathbf{k}^T\mathbf{A}^{-1}\mathbf{V}^{-1}\boldsymbol{\eta} \\ &= 2\pi\mathbf{k}^T(\mathbf{V}\mathbf{A})^{-1}\boldsymbol{\eta}. \end{aligned} \quad (2.24)$$

Letting

$$\boldsymbol{\kappa}^T = 2\pi\mathbf{k}^T(\mathbf{V}\mathbf{A})^{-1} \quad (2.25)$$



yields

$$\boldsymbol{\kappa} = 2\pi(\mathbf{VA})^{-T}\mathbf{k} = 2\pi(\mathbf{A}^T\mathbf{V}^T)^{-1}\mathbf{k}, \quad (2.26)$$

which shows that the sampling of the continuous Fourier domain is given

$$F(\mathbf{k}) = F_c(\mathbf{S}\mathbf{k}) = F_c(\boldsymbol{\kappa}), \quad (2.27)$$

where  $\mathbf{S} = 2\pi(\mathbf{A}^T\mathbf{V}^T)^{-1}$  is the sampling matrix.

This leads to the duality

$$\mathbf{S}^T\mathbf{T} = 2\pi\mathbf{I}, \quad (2.28)$$

where  $\mathbf{I}$  is the identity matrix. Defining  $\mathbf{U} = \mathbf{V}^{-T}$  as periodicity of the dual lattice gives

$$\mathbf{U}^T\mathbf{V} = 2\pi\mathbf{I}, \quad (2.29)$$

(Mersereau and Speake, 1983). The Fourier lattice given by  $\mathbf{U}^T$  is called reciprocal lattice, or in the area of mathematics, geometry of numbers, as the polar lattice. Here it will be referred to as the dual lattice.

For a conventional rectangular lattice with Cartesian axes  $x, y$ , the matrix  $\mathbf{V}$  can be expressed

$$\mathbf{V} = \begin{pmatrix} \Delta x & 0 \\ 0 & \Delta y \end{pmatrix} \quad (2.30)$$

and periodicity matrix

$$\mathbf{A} = \begin{pmatrix} N_x & 0 \\ 0 & N_y \end{pmatrix}. \quad (2.31)$$

This has reciprocal sampling matrix

$$\mathbf{S} = 2\pi \begin{pmatrix} \frac{1}{N_x\Delta x} & 0 \\ 0 & \frac{1}{N_y\Delta y} \end{pmatrix}, \quad (2.32)$$

which is the samplings intervals for Fourier space.

Any given lattice generated by the sampling matrix  $\mathbf{V}$  could also be generated by  $\mathbf{W}$ , given as

$$\mathbf{W} = \mathbf{E}\mathbf{V}, \quad (2.33)$$

where the matrix  $\mathbf{E}$  is unimodular,  $\det(\mathbf{E}) = \pm 1$ . This shows that the sampling matrices are not unique, but the quantity  $\det(\mathbf{V})$  is unique for a given lattice.

## 2.6 Upsampling and Downsampling of Functions

In 1D discrete Fourier analysis the upsampling  $g(n)$  of a discrete function  $f(i)$  for  $i = 0, 1, 2, \dots, N - 1$ , is by filling in  $M - 1$  zeros between each sample, this can be defined as

$$g(n) = \begin{cases} f(\frac{n}{M}) & \text{if } n = 0, M, 2M, \dots, M(N - 1) \\ 0 & \text{otherwise} \end{cases}. \quad (2.34)$$

The similarity theorem states that this operation results in a packing of  $M$  periods in the Fourier domain. In the 2D discrete Fourier analysis the operation becomes fairly different.

For a 2D function  $f(\mathbf{j})$ , defined on a lattice given by  $\mathcal{R}(\mathbf{A})$ , the upsampling operation can be defined as

$$g(\mathbf{n}) = \begin{cases} f(\mathbf{L}^{-1}\mathbf{n}) & \text{if } \mathbf{L}^{-1}\mathbf{n} \in \mathcal{R}(\mathbf{A}) \\ 0 & \text{otherwise,} \end{cases} \quad (2.35)$$

where  $\mathbf{L}$  is the upsampling matrix (Evans et al., 1994). This corresponds to a mapping from the original grid to a larger grid  $\mathcal{R}(\mathbf{L}\mathbf{A})$ . In Fourier domain this operation gives

$$G(\mathbf{k}) = \sum_{\mathbf{n}} g(\mathbf{n}) e^{-2\pi i(\mathbf{k}^T \mathbf{A}^{-1} \mathbf{n})} \quad (2.36)$$

letting  $\mathbf{n} = \mathbf{L}\mathbf{j}$

$$\begin{aligned} G(\mathbf{k}) &= \sum_{\mathbf{j}} g(\mathbf{L}\mathbf{j}) e^{-2\pi i(\mathbf{k}^T \mathbf{A}^{-1} \mathbf{L}\mathbf{n})} \\ &= \sum_{\mathbf{j}} f(\mathbf{j}) e^{-2\pi i(\mathbf{L}^T \mathbf{k})^T \mathbf{A}^{-1} \mathbf{n}} \\ &= F(\mathbf{L}^T \mathbf{k}). \end{aligned} \quad (2.37)$$

This shows that upsampling any function on a given lattice to a denser, changes the functions grid in dual domain.

Downsampling can be defined as

$$g(\mathbf{n}) = f(\mathbf{M}\mathbf{n}) \quad (2.38)$$

where  $\mathbf{M}$  is the downsampling matrix. The range of this matrix defines the points on the grid which will be kept and the rest will be discarded. A similar argument as for upsampling can be made to show that as the sampling points decreases, the lattice in Fourier domain changes. The results from a Fourier transform of a function and the transform of a downsampled or upsampled function will differ with a factor  $\det(\mathbf{M})$ . This is corrected by multiplication with this factor after resampling.

These upsampling and downsampling operators have input and output on uniform sampled grids. If this is not the case interpolation is needed when mapping between lattices.

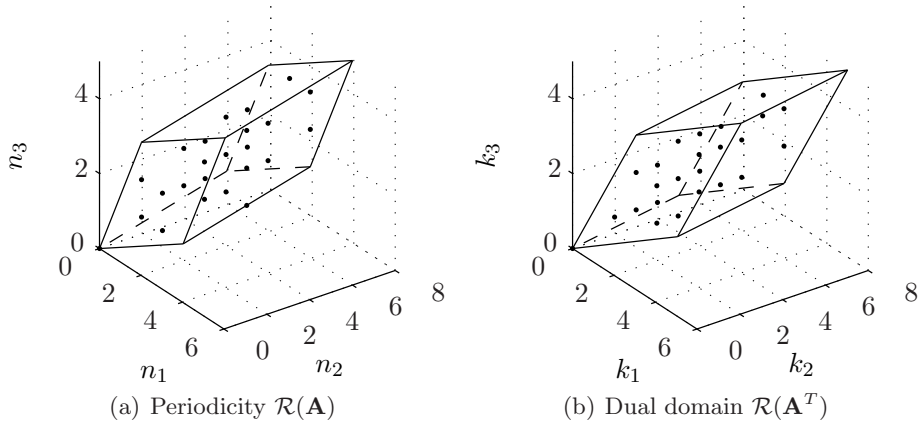


Figure 2.4: 3D sampling lattice

## 2.7 Multidimensional Discrete Fourier Transform

There are many applications where there is need for more than a 2D Fourier transformation. Examples of this are optical, acoustic and seismic waves which propagate in 3D, sometimes 4 if time is considered. It is naturally very difficult to visualize sampling grids and functions in more than 3D, even in 3D there are difficulties.

The theory presented in the previous sections is a general approach to sampling lattices. With some simple modifications it can be expanded to  $n$  dimensions. A sampling periodicity can be defined with the matrix

$$\mathbf{A} = \begin{pmatrix} a_{1,1} & a_{1,2} & \cdots & a_{1,n} \\ a_{2,1} & a_{2,2} & \cdots & a_{2,n} \\ \vdots & \vdots & \ddots & \vdots \\ a_{n,1} & a_{n,2} & \cdots & a_{n,n} \end{pmatrix}, \quad (2.39)$$

where the columns are linear independent vectors.

By defining  $\mathbf{n} = (n_1, n_2, \dots, n_n)^T$  and  $\mathbf{k} = (k_1, k_2, \dots, k_n)^T$  the Fourier transform can be written

$$F(\mathbf{k}) = \sum_{\mathbf{n} \in \mathcal{R}(\mathbf{A})} f(\mathbf{n}) e^{2\pi i (\mathbf{k}^T \mathbf{A}^{-1} \mathbf{n})}. \quad (2.40)$$

The Smith normal form theorem is valid for any  $n \times n$  integer matrices, which is discussed in Appendix A.5, and the computations of the  $n$ D Fourier transform is the same as in Section 2.4. An example of a 3D sampling grid is the range of the matrix

$$\mathbf{A} = \begin{pmatrix} 3 & 2 & 1 \\ 1 & 4 & 1 \\ 1 & 2 & 3 \end{pmatrix}. \quad (2.41)$$

The range  $\mathcal{R}(\mathbf{A})$  and the dual  $\mathcal{R}(\mathbf{A}^T)$ , is plotted in Figure 2.4, with  $\det(\mathbf{A}) = 21$  sampling points.



## Chapter 3

# Some Special Cases

In the first section of this chapter, a case where two sampling matrices covers the same sampling points is presented. The second part is an overview of algorithms to calculate the Hexagonal Fourier Transform. Thereafter two special cases of Hexagonal sampling is presented, referred to as Quincunx and diamond sampling. Finally an example of sampling and filtering a 2D signal on a Quincunx sampling grid.

### 3.1 Different Periodicity Matrices Covering the Exact Same Region

As mentioned in Section 2.3 it is often possible to find different periodicity matrices which cover the exact same sampling points in one domain and have a different sampling geometry in their dual domain.

The periodicity matrix

$$\mathbf{A}_1 = \begin{pmatrix} 5 & 3 \\ 0 & 3 \end{pmatrix}, \quad (3.1)$$

yields  $\det(\mathbf{A}_1) = 15$  sampling points, given as  $\mathbf{n} \in \mathcal{R}(\mathbf{A}_1)$ . Defining the Gaussian or Bell function,

$$f(\mathbf{n}) = e^{-\lambda \|\mathbf{n}\|^2} \quad \text{for } \mathbf{n} \in \mathcal{R}(\mathbf{A}_1), \quad (3.2)$$

on these points, results in the image Figure 3.1(a). The advantage of this function is that its Fourier transform is another Gaussian, which makes it easy to compare Fourier transforms on different grids. In this example the parameter  $\lambda = 0.1$ . To have an image for comparing the different sampling geometries, the first will be the conventional rectangular sampling. The image and the 2D DFT of the function sampled on a rectangular sampling grid given by

$$\mathbf{N} = \begin{pmatrix} 7 & 0 \\ 0 & 3 \end{pmatrix}, \quad (3.3)$$

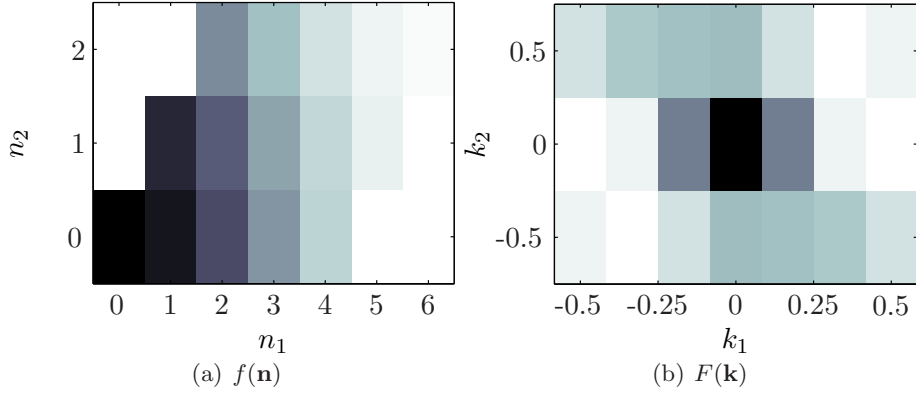


Figure 3.1: Rectangular sampling of the function  $f(\mathbf{n})$  and its Fourier transform

is plotted in Figure 3.1(a) and 3.1(b). This sampling geometry gives  $\det(\mathbf{N}) = 21$  sampling points, 6 of these will have value zero because the Fourier domain will later be compared with sampling schemes which does not cover these points. As a result of the similarity theorem these zeros corresponds to interpolation of the Fourier domain.

The matrix

$$\mathbf{A}_2 = \begin{pmatrix} 4 & 3 \\ -1 & 3 \end{pmatrix}. \quad (3.4)$$

covers the exact same sampling points as  $\mathbf{A}_1$ , i.e. the points in  $\mathcal{R}(\mathbf{A}_2)$  equals the points in  $\mathcal{R}(\mathbf{A}_1)$ . Both have the  $N = \det(\mathbf{A}_1) = \det(\mathbf{A}_2) = 15$  equal sampling points, but have different periodicity. Using one of these sampling geometries will be more efficient than sampling with the matrix  $\mathbf{N}$ . The methodology from Section 2.4 lets the DFT be calculated with FFT. The first step is to diagonalize the matrices using the Smith normal form theorem, to  $\mathbf{A} = \mathbf{P}\mathbf{D}\mathbf{Q}$ . The MATLAB code in Appendix A.7.1 gives the following matrices

$$\mathbf{P}_1 = \begin{pmatrix} 1 & 0 \\ 6 & 1 \end{pmatrix}, \quad \mathbf{Q}_1 = \begin{pmatrix} 5 & 3 \\ -2 & -1 \end{pmatrix}, \quad \mathbf{D}_1 = \begin{pmatrix} 1 & 0 \\ 0 & 15 \end{pmatrix} \quad (3.5)$$

$$\mathbf{P}_2 = \begin{pmatrix} 4 & 1 \\ -1 & 0 \end{pmatrix}, \quad \mathbf{Q}_2 = \begin{pmatrix} 1 & -3 \\ 0 & 1 \end{pmatrix}, \quad \mathbf{D}_2 = \begin{pmatrix} 1 & 0 \\ 0 & 15 \end{pmatrix}. \quad (3.6)$$

Figure 3.2 is a graphical representation of the steps in the transformation. The map from plot (a) to (b) is  $\Gamma_n : \tilde{\mathbf{n}} = \mathbf{P}_1^{-1}\mathbf{n}$ , the points then have a rectangular period  $\mathcal{R}(\mathbf{D}_1)$  which is naturally isomorphic to  $\mathbb{Z}_{15}$ . Therefore it is sufficient to calculate a 1D FFT. In Figure 3.2 (c) the map  $\Gamma_k^{-1} : \mathbf{k} = \mathbf{Q}_1^T \tilde{\mathbf{k}}$  for  $\tilde{\mathbf{k}} = \tilde{\mathbf{n}}$  has been calculated. The points from (c) is transformed by  $\kappa = \mathbf{A}^T \mathbf{k}$  to a period given by  $\mathcal{R}(\mathbf{I})$  in (d), which have the same periodicity as the output from the rectangular 2D FFT.

The same procedure is used for the periodicity matrix  $\mathbf{A}_2$ , and the results are given in Figure 3.3. In Figure 3.2(a) and 3.3(a) the same three points are marked with a red circle. After the first map the three points are not in the same position, and that is the case throughout the sequence. This illustrates that the use of different periodicity matrices results in different sampling of the transform itself.

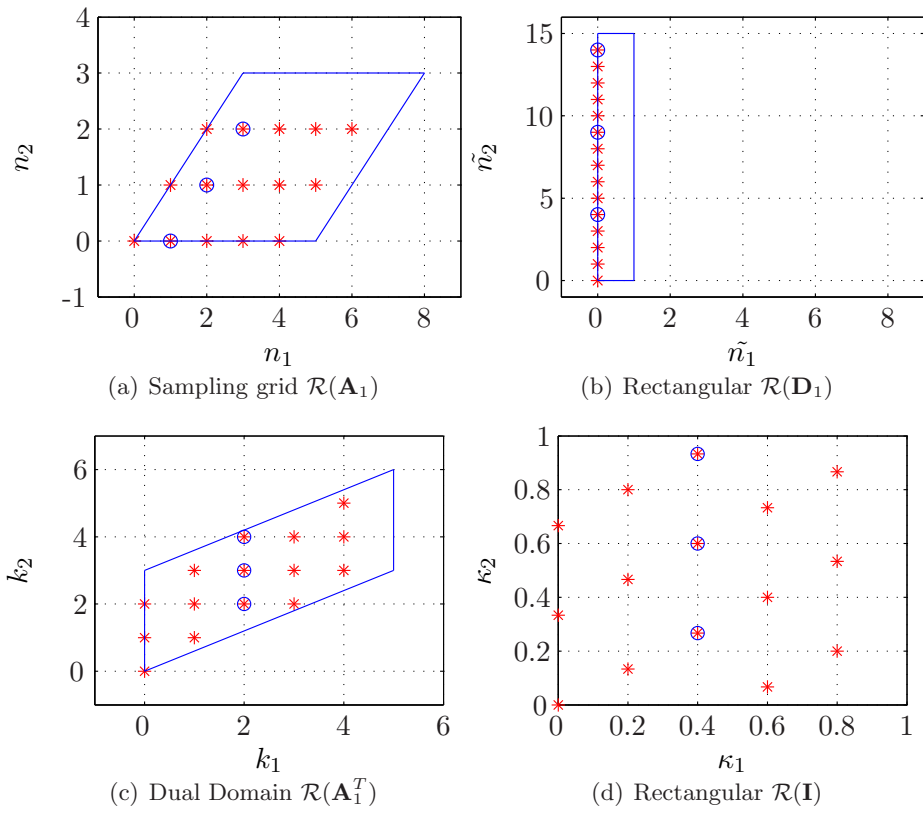


Figure 3.2: The steps in sampling with matrix  $\mathbf{A}_1$

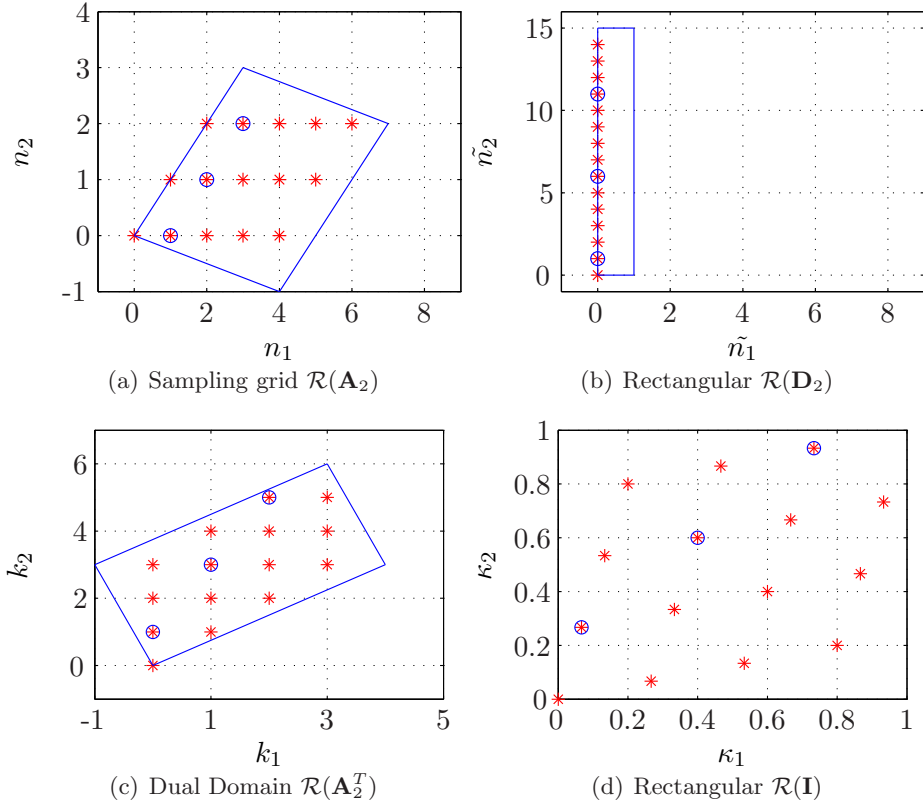


Figure 3.3: The steps in sampling with matrix  $\mathbf{A}_2$

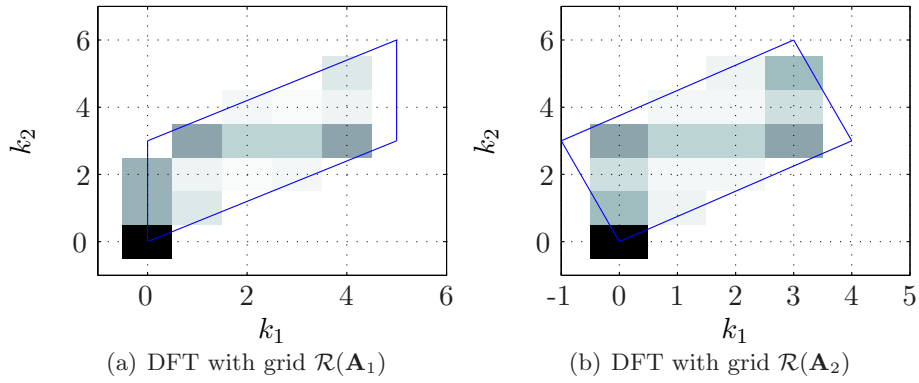


Figure 3.4:  $F(\mathbf{k})$  from different periodicity matrices



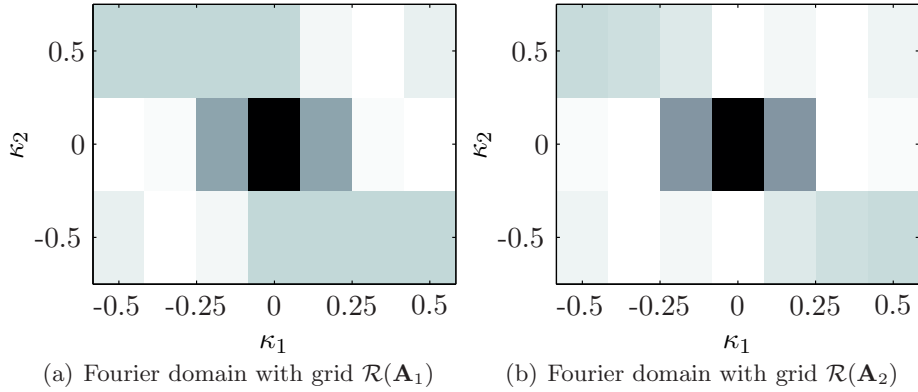


Figure 3.5:  $F(\mathbf{k})$  from different periodicity matrices interpolated to a rectangular grid on the Nyquist period

The Fourier transformation of the function sampled with periodicity matrix  $\mathbf{A}_1^T$  and  $\mathbf{A}_2^T$  is plotted, respectively in Figure 3.4(a) and Figure 3.4(b). The DC component, sample  $(0,0)$ , has the same value in both plots, because the exponential in the transformation is equal to 1. If these images are periodically expanded the images would look much the same except for differences in some of the values. This is a result of the different sampling of the Fourier transformation itself.

The final problem of this example is to plot the results of the sampling with the matrices  $\mathbf{A}_1$  and  $\mathbf{A}_2$  on the Nyquist interval. Figure 3.2(d) and 3.3(d) shows that the sampling points after the coordinate transform  $\boldsymbol{\kappa} = \mathbf{A}^{-T}\mathbf{k}$  are not integers. To create an image on a rectangular grid from these points interpolation is needed. First the points  $\boldsymbol{\kappa}$  are shifted to the Nyquist interval  $-1/2$  to  $1/2$  by modular arithmetics and then interpolated with MATLAB's v4 interpolation function, see Appendix C. The results of this are plotted Figure 3.5. The images are very similar and a comparison with the rectangular DFT, Figure 3.1(b), shows similarities.

## 3.2 Hexagonal Sampling

There are many examples of methodology for sampling and defining the Fourier Transform on hexagonal grids. Here there will be presented three possibilities. The first is regular hexagonal sampling, where the sampling points are equidistant in all directions, a hexagonal Fourier transform with rectangular output, and a method using Smith normal form.

A hexagonal sampling grid can be defined by a sampling matrix

$$\mathbf{V} = (\mathbf{v}_1 \quad \mathbf{v}_2) = \begin{pmatrix} a_{11} & a_{21} \\ 0 & a_{22} \end{pmatrix}, \quad (3.7)$$

where  $\mathbf{v}_1$  and  $\mathbf{v}_2$  is given as in Figure 3.6(a). On a regular hexagonal sampling grid, a sampling point have the same distance to its six nearest neighbors. The angle between the two vectors is then 60 degrees, and defining

$$a_{21} = \frac{a_{11}}{2}, \quad (3.8)$$

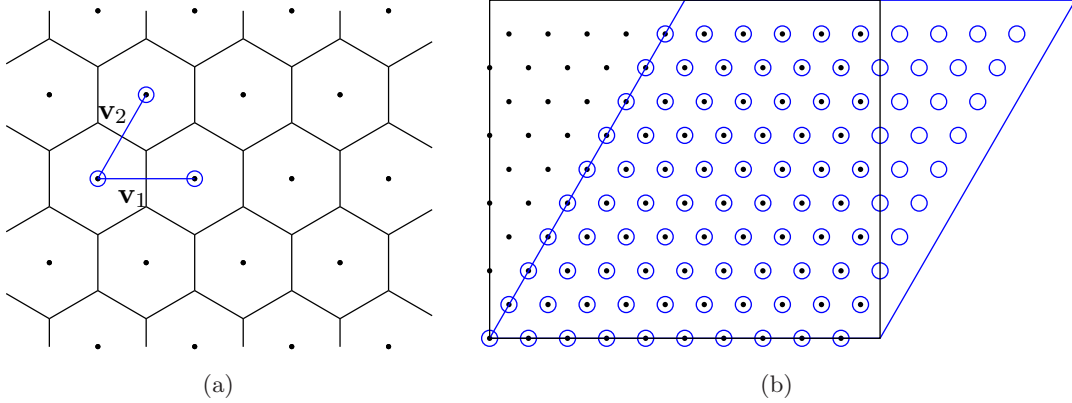


Figure 3.6: (a) Hexagonal sampling points and generating vectors, (b) Two periods with the same sampling points

gives

$$a_{22} = a_{21} \tan 60^\circ = \sqrt{3}a_{21} = \frac{\sqrt{3}}{2}a_{11}. \quad (3.9)$$

The lattice in Figure 3.6(a) is a hexagonal lattice, generated with  $a_{11} = 1$ . The lines enclosing the sampling points is a Voronoi diagram, see Appendix B. A general hexagonal sampling grid can be given

$$\mathbf{V} = \begin{pmatrix} d_1 & -d_1/2 \\ 0 & d_2 \end{pmatrix}, \quad (3.10)$$

where  $d_1 = a_{11}$  and  $d_2 = a_{22}$ .

The sampling points on a hexagonal sampling grid can be contained in two periods, Figure 3.6(b), which are equivalent. The black points illustrate hexagonal sampling points in a rectangular period, and the blue circles the equivalent in a hexagonal coordinate system. The two sampling periods can be represented by at least two integer periodicity matrices,

$$\mathbf{N}_1 = \begin{pmatrix} N_1 & 0 \\ 0 & N_2 \end{pmatrix} \quad (3.11)$$

and

$$\mathbf{N}_2 = \begin{pmatrix} N_1 & N_2/2 \\ 0 & N_2 \end{pmatrix}, \quad (3.12)$$

assuming  $N_2$  is even. The sampling period is defined by the matrix product  $\mathbf{T} = \mathbf{V}\mathbf{N}$ . Using the methodology from Section 2.5, the dual lattice when using periodicity matrix  $\mathbf{N}_2$  is given by

$$\mathbf{S} = 2\pi(\mathbf{A}^T\mathbf{V}^T)^{-1} = \begin{pmatrix} 2\pi/d_1N_1 & 0 \\ 0 & 2\pi/d_2N_2 \end{pmatrix}. \quad (3.13)$$

This is a diagonal matrix, which shows that Fourier domain for these choices of  $\mathbf{N}$  and  $\mathbf{V}$  is a rectangular lattice, this will be treated in the next section.

An example of a function sampled on a regular hexagonal grid is given in Figure 3.7(a). The function is given as

$$f(\mathbf{r}) = J_0(ar), \quad (3.14)$$

where  $J_0$  is the zero order Bessel function of the first kind,  $a > 0$ , and

$$r = \sqrt{x^2 + y^2}. \quad (3.15)$$

It can be shown by the Hankel transform that this function has a circular spectrum and the parameter  $a$  governs the radius of this circle, chosen  $a = 3/2$ . The matrix generating the sampling points is here given

$$\mathbf{V} = \begin{pmatrix} 2/\sqrt{3} & -1/\sqrt{3} \\ 0 & 1 \end{pmatrix}, \quad (3.16)$$

and the sampling points are in a rectangular period, given by  $\mathbf{N}_1$ . The periodicity matrix is diagonal, and the dual lattice is also on a rectangular period. Fourier domain is generated by the matrix  $\mathbf{V}^{-T}$ , and is shown in Figure 3.7(b). The DFT is calculated by summation over all the indexes. Both Figures are generated by filling Voronoi cells with a color corresponding to the functions value.

For the regular hexagonal sampling grid, there is developed a fast Fourier transform in Mersereau (1979).

### 3.2.1 Hexagonal Fourier Transform with Rectangular Output

Often it is convenient to get the result of a Fourier transform of hexagonally sampled function on a rectangular grid. Ehrhardt (1993) presents a method which solves this without interpolation afterwards.

The DFT is defined as in Section 2.3,

$$F(\mathbf{k}) = \sum_{\mathbf{n}} f(\mathbf{n}) e^{-2\pi i(\mathbf{k}^T \mathbf{N}^{-1} \mathbf{n})}, \quad (3.17)$$

and the integer periodicity matrix is given by equation (3.12). By direct input, the DFT is given

$$F(k_1, k_2) = \sum_{n_1=0}^{N_1-1} \sum_{n_2=0}^{N_2-1} f(n_1, n_2) e^{-2\pi i[(n_1-n_2/2)k_1/N_1+n_2k_2/N_2]}. \quad (3.18)$$

This operation can be divided in to three steps, first

$$F_1(k_1, n_2) = \sum_{n_1=0}^{N_1-1} f(n_1, n_2) e^{-2\pi i k_1 n_1 / N_1}, \quad (3.19)$$

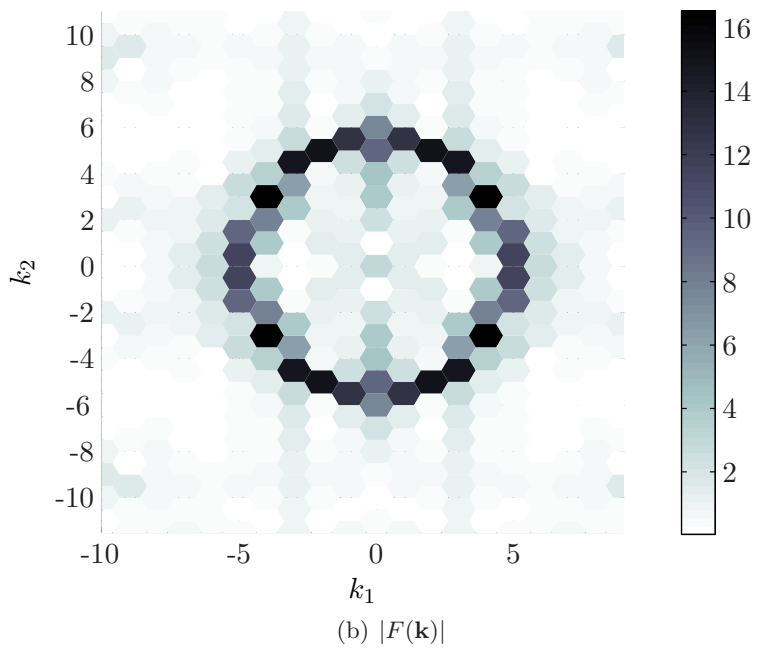
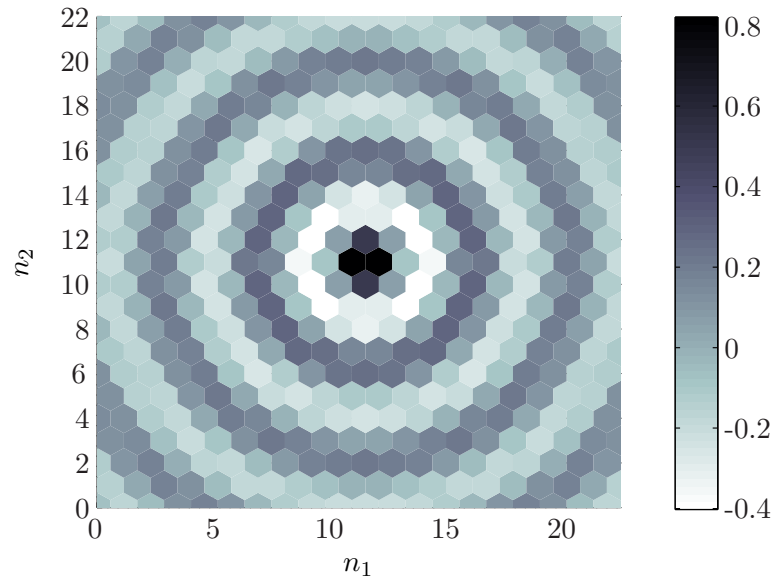


Figure 3.7: (a) The function in equation 3.14 on a regular hexagonal lattice, (b) its Fourier transform.

which is calculated with a 1D FFT. Then a filtering

$$F_2(k_1, n_2) = F_1(k_1, n_2)e^{\pi i k_1 n_2 / N_1}, \quad (3.20)$$

which is an interpolation of the points to a rectangular grid. This filtering is a special case of the interpolation method described in Appendix C.1.

Next it is possible to calculate the 1D FFT in the other direction

$$F(k_1, k_2) = \sum_{n_2=0}^{N_2-1} F_2(k_1, n_2)e^{-2\pi i k_2 n_2 / N_2}. \quad (3.21)$$

The output from this algorithm is Fourier space on a  $N_1 \times N_2$  rectangular grid. A square periodicity imply that  $N_2/N_1 = d_1/d_2$  and  $d_1/d_2$  has to be a rational number. This shows that it is not possible to calculate the DFT of a regular hexagonal grid with this method. Ehrhardt (1993) suggest to approximate the fraction  $\sqrt{3}/2$  with a rational number.

When the sampling points are spanned within a rectangle, as the black points in Figure 3.6(b), the filtering can be defined

$$F_2(k_1, n_2) = F_1(k_1, n_2)e^{\pi i k_1 \text{mod}(n_2, 2) / N_1}, \quad (3.22)$$

since it is shifting every second column of points down one half. To get a hermitian filter, and output as the rectangular FFT, the sampling points  $k_1$  should be defined

$$k_1 = \text{mod}(k_1 + \lfloor N_1/2 \rfloor, N_1) - N_1/2, \quad (3.23)$$

which is the Nyquist interval.

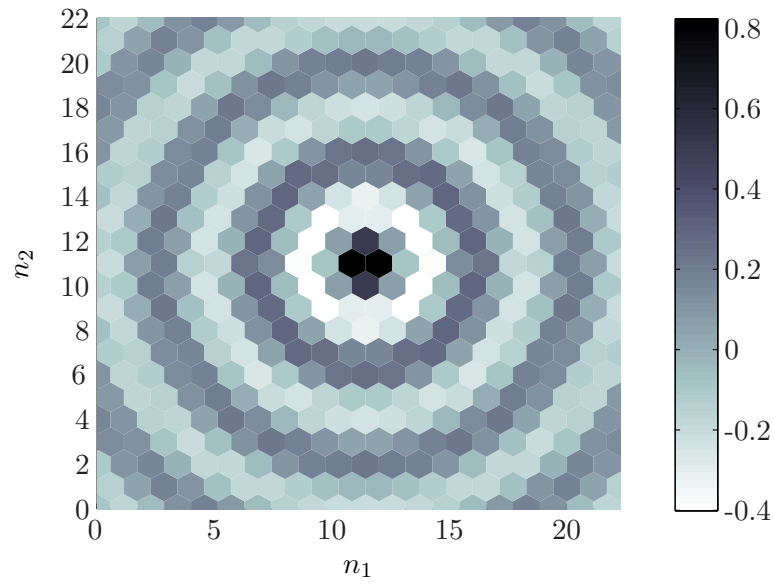
The same function as the example in the previous section is sampled on a lattice generated by

$$\mathbf{V} = \begin{pmatrix} 8/7 & -8/14 \\ 0 & 1 \end{pmatrix}, \quad (3.24)$$

with  $N_1 = 20$  and  $N_2 = 23$ , is given in Figure 3.8(a). Using the method described here, results in the image in Figure 3.8(b). The result is on a rectangular grid and conventional processing algorithms could be used directly.

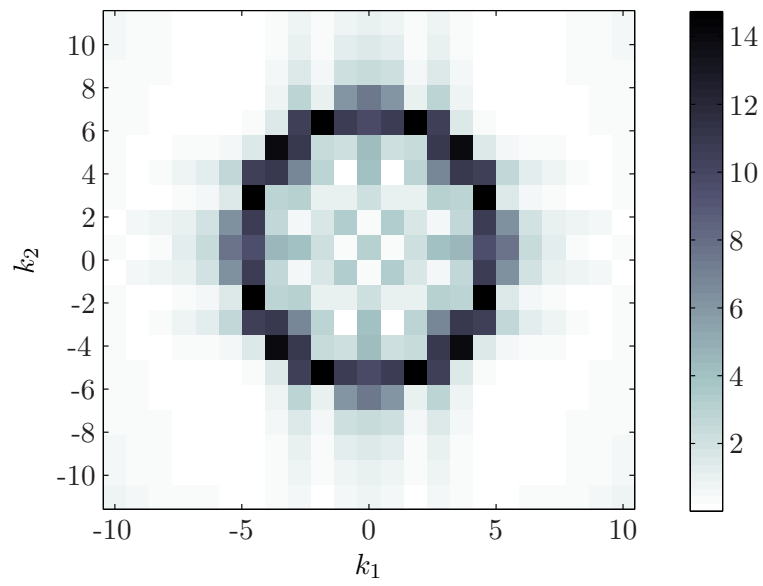
Equation (3.20) is a expression for the Fourier transform in one direction, and many (geophysical) processing algorithms are defined in the frequency-offset domain. Therefore this method could be used for these processing tasks.

The transformation is easily inverted, just changing the sign in the exponential function.



(a)  $f(r)$

abs



(b)  $|F(\mathbf{k})|$

Figure 3.8: (a) The function sampled on a hexagonal grid given by  $\mathbf{V}$ , and (b) Fourier domain on a rectangular grid.

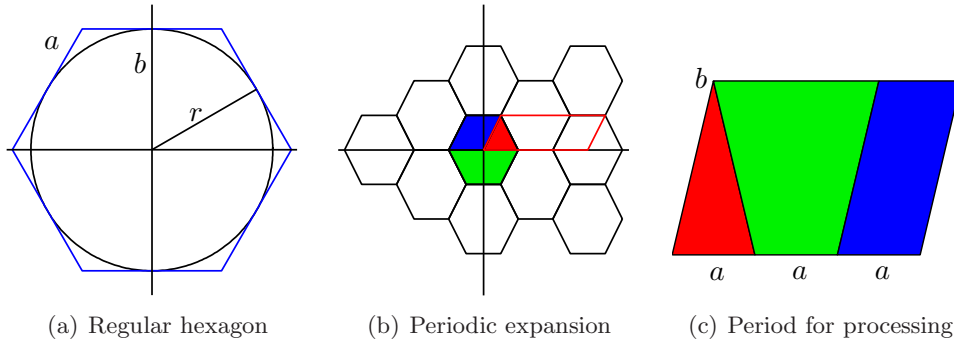


Figure 3.9: Regular hexagonal sampling

### 3.2.2 Assuming Hexagonal Periodicity in Fourier domain

Conventional 2D sampling assumes a rectangular periodicity in Fourier domain. Signals which have a circular bandwidth are then oversampled. The most efficient sampling of a circular bandwidth is hexagonal, shown in Figure 3.9(a). A regular hexagon is a six sided polygon where all six sides have same length,  $a$ . If the circle enclosed in the hexagon have radius  $r$ , which in this case is equal to the hexagons height  $b$ , the Pythagorean theorem gives

$$a = \frac{2b}{\sqrt{3}}.$$

Mersereau (1979) shows that this periodicity yields a 13.4% more efficient sampling than the conventional rectangular sampling. By periodic expansion of the hexagon, see Figure 3.9(b), the data in the hexagon can be contained in many different sampling periods. One period, which can be represented with the matrix notation from Chapter 2, is the red parallelogram in Figure 3.9(b). The range of the matrix

$$\mathbf{R} = \begin{pmatrix} 3a & \frac{\sqrt{3}}{2}a \\ 0 & \frac{a}{2} \end{pmatrix} \quad (3.25)$$

gives the hexagonal period, Figure 3.9(c).

Constructing a hexagon with an integer periodicity matrix will make it possible to calculate DFT using the Smith normal form theorem. Choosing the vertical and horizontal number of samples of the hexagon to be  $2N + 1$ , the left and right side  $2M + 1$ , where  $M, N \in \mathbb{Z}$ , gives a integer periodicity matrix. A periodic expansion of a hexagon where  $N = 2M$  and  $M = 2$  is shown in Figure 3.10. The black parallelogram is a period which covers all the sampling points and can be used with Smith normal form.

The sampling points enclosed in this hexagon is shown in Figure 3.11(a) and in Figure 3.11(b) the points have been mapped to the parallelogram for Smith normal form. The colored circles show how the points are mapped to the new period. This period can be expressed as the range of the integer matrix

$$\mathbf{H}^T = \begin{pmatrix} N & 0 \\ 3M & 2(N + M) \end{pmatrix}, \quad (3.26)$$

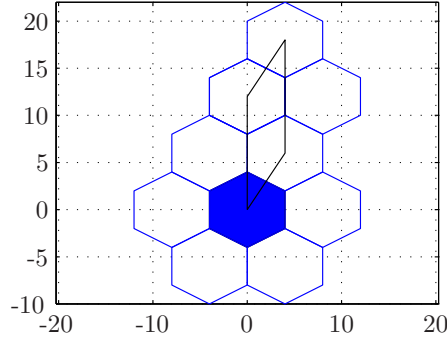


Figure 3.10: A periodic sequence of integer hexagons in the plane.

and for the example when  $N = 2M$

$$\mathbf{H}^T = \begin{pmatrix} N & 0 \\ 3N/2 & 3N \end{pmatrix}. \quad (3.27)$$

This sampling has  $\det(\mathbf{H}) = 2N(N+M) = 3N^2$  sampling points and compared to rectangular sampling of the same bandwidth which would have  $2N \times 2N = 4N^2$  number of sampling points, assuming hexagonal periodicity is 25% more efficient. The matrix is of right Hermite normal form, if the hexagon is rotated 90 degrees, as the one in Figure 3.9(a), the periodicity matrix would be of left Hermite normal form, (Appendix A.7.6). The sampling points in dual domain,  $\mathbf{n} \in \mathcal{R}(\mathbf{H})$ , is shown in Figure 3.11(c).

A function is generally sampled with a rectangular periodicity, which is best for plotting. If this rectangular period can be given by the matrix

$$\mathbf{T} = \begin{pmatrix} T_1 & 0 \\ 0 & T_2 \end{pmatrix}, \quad (3.28)$$

the sampling points on a rectangular period can be expressed

$$\boldsymbol{\eta} = \mathbf{T}\mathbf{H}^{-1}\mathbf{n}. \quad (3.29)$$

In Figure 3.11(d) a period  $T_1 = T_2 = 2N$  is assumed, and the Voronoi cells shows the hexagonal shape of the lattice.

The same function as used with the previous methods are sampled on a lattice given by  $N = 20$ ,  $M = 10$  and  $T_1 = T_2 = 20$ , Figure 3.12(a). Using the approach outlined, the hexagonal Fourier domain is shown in Figure 3.12(b).

When assuming hexagonal periodicity the alias pattern naturally changes and become more intricate. There is six directions where the spectrum folds. Choosing the radius of the circle in Figure 3.12(b) larger than the bandwidth is a good example of this. In Figure 3.13 it is clear that the circle folds around the six borders of the hexagon.

Sampling with a hexagon which is integer does not cover a circular band region, as a regular hexagon, but it is preferable in some cases, this is illustrated with the circle outside the hexagon in Figure 3.9(a).



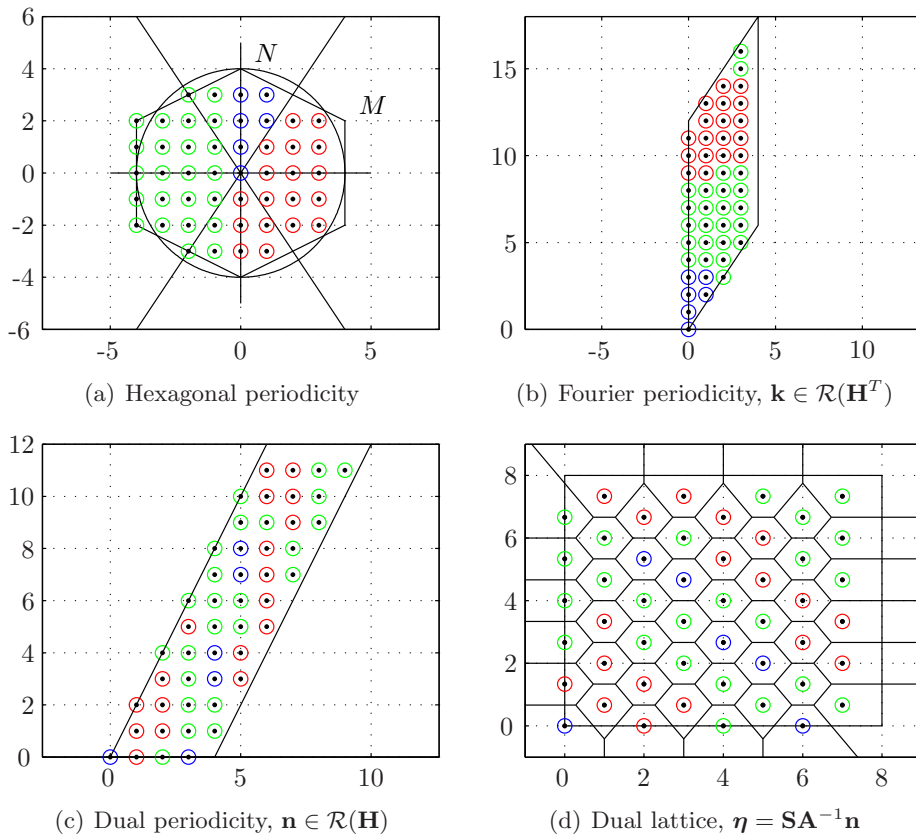
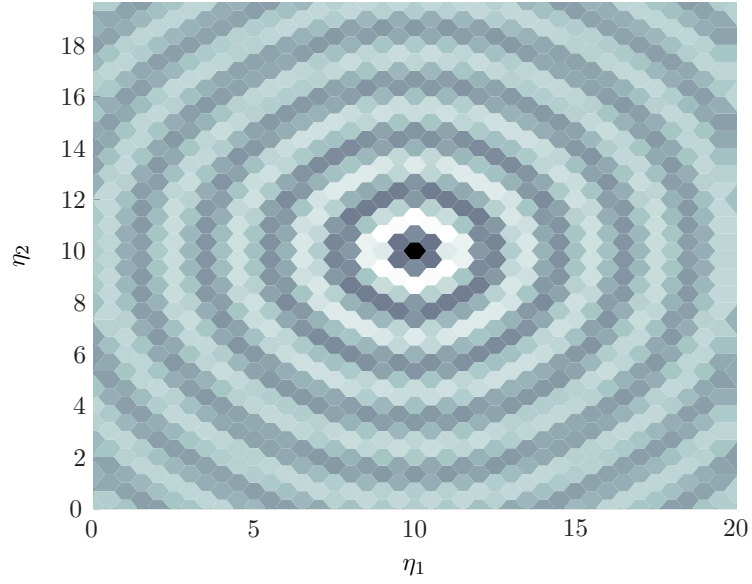
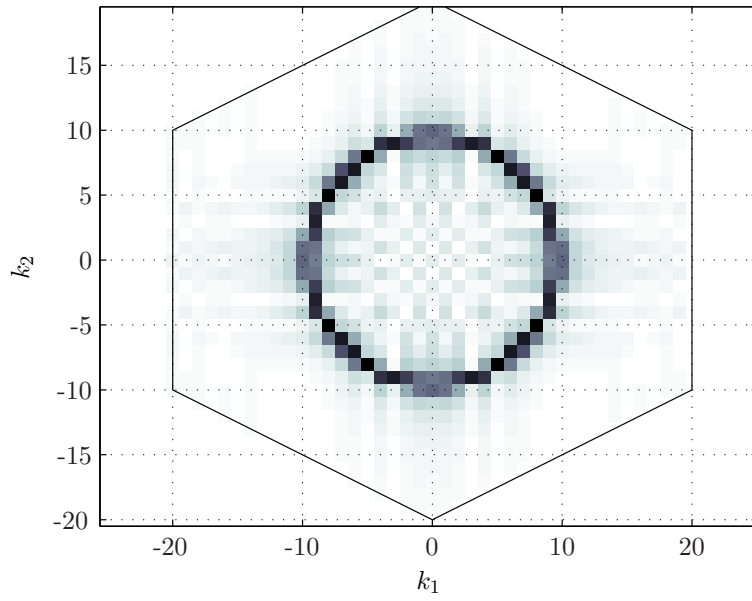


Figure 3.11: The different sampling grids in different domains, (a) The hexagonal bandwidth in Fourier domain. (b) The sampling geometry for using Smith normal form, (c) the period in dual domain and (d) the sampling grid with rectangular periodicity.



(a)  $f(r)$



(b)  $|F(\mathbf{K})|$

Figure 3.12: (a) The function  $f(r) = J_0(ar)$  sampled on a lattice given by  $N = 20$ ,  $M = 10$ ,  $T_1 = T_2 = 20$ , and (b) Fourier domain with hexagonal periodicity.

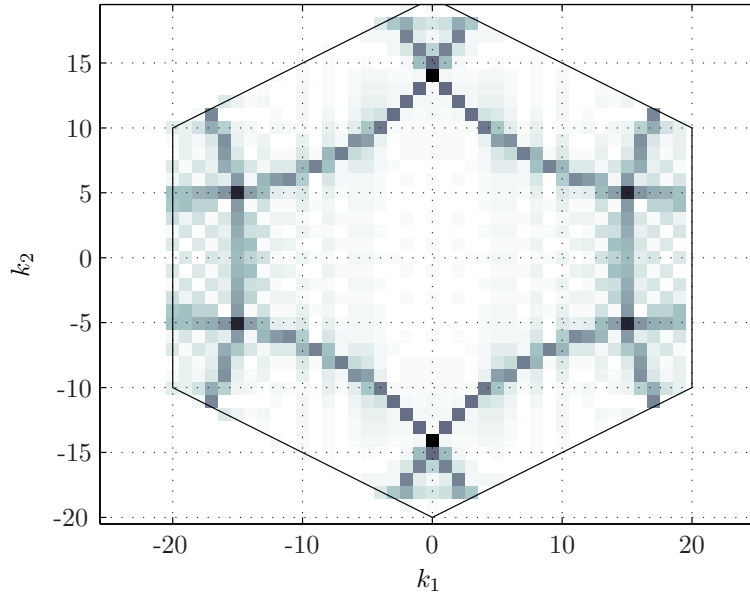


Figure 3.13: Example of alias with hexagonal periodicity

It is naturally possible to construct the hexagon with a different number of samples along the horizontal and vertical axis. But the analysis is simpler when assuming the same number of samples in both directions.

### 3.2.3 Hexagonal Filtering

Downsampling of functions is generally a low-pass filtering. Assuming hexagonal periodicity in Fourier domain and sampling a signal on this kind of lattice, is equivalent to a hexagonal low-pass filtering. Studying such a filtering gives insight to the downsampling from rectangular to hexagonal lattices. Starting with the “jinc”-function, defined as

$$\text{jinc}(r) = \frac{J_1(r)}{r}, \quad r = \sqrt{x^2 + y^2}, \quad (3.30)$$

where  $J_1(r)$  is the first order Bessel function of the first kind. The limit  $r \rightarrow 0$  is defined

$$\lim_{r \rightarrow 0} \text{jinc}(r) = \frac{1}{2}. \quad (3.31)$$

This function is the impulse response of a circular low pass filter. The function sampled on a lattice defined by

$$\mathbf{N} = \begin{pmatrix} 41 & 0 \\ 0 & 41 \end{pmatrix}, \quad (3.32)$$

is shown in Figure 3.14. The jinc-function is real and symmetric, therefore also the Fourier transform real and symmetric.

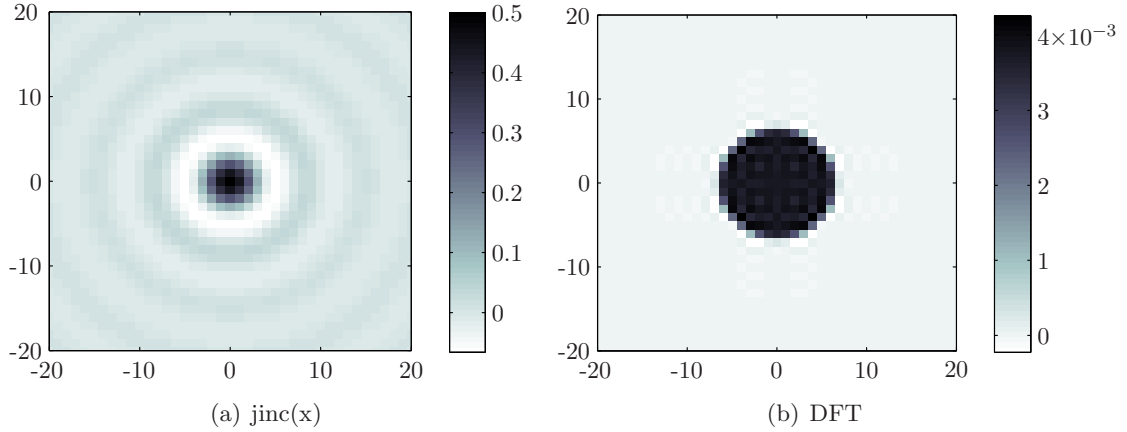


Figure 3.14: (a) The jinc-function and (b) the Fourier transform

The filter

$$\mathbf{F}(\mathbf{n}) = \begin{cases} 1 & \text{if } \mathbf{n} \in \mathcal{R}(\mathbf{H}^T) \\ 0 & \text{otherwise} \end{cases} \quad (3.33)$$

where

$$\mathbf{H}^T = \begin{pmatrix} 20 & 0 \\ 10 & 90 \end{pmatrix}, \quad (3.34)$$

is plotted in Figure 3.15(a). Multiplying the jinc-function with this filter simulates the down-sampling to the hexagonal periodicity in Fourier domain. The real, imaginary and absolute value of the filtered function is shown in Figure 3.15(b,c,d). The Fourier transform is Hermitian, because the filter real. It has an imaginary part because it is not symmetric. Constructing a filter without the asymmetric sampling points results in a real symmetric Fourier transform, see Figure 3.16.

A hexagon has six fold symmetry, and a circle is symmetric on such sampling. This example shows that downsampling a function in Fourier domain to a hexagonal periodicity results in an inverse Fourier transform with a real and imaginary part. Therefore the best interpolation method to a rectangular grid is Fourier interpolation. The processing should be done in the range of Smith normal form, and afterwards the sampling points should be transformed back to hexagonal periodicity within a rectangular period. Fourier domain will then be Hermitian and the inverse Fourier transform is real.

In general, a function should not be downsampled to a hexagonal lattice in Fourier domain, since it introduce an imaginary part. Sampling the function on the points given by  $\boldsymbol{\eta} \in \mathcal{R}(\mathbf{T})$  is preferable, but does in most cases involve interpolation.

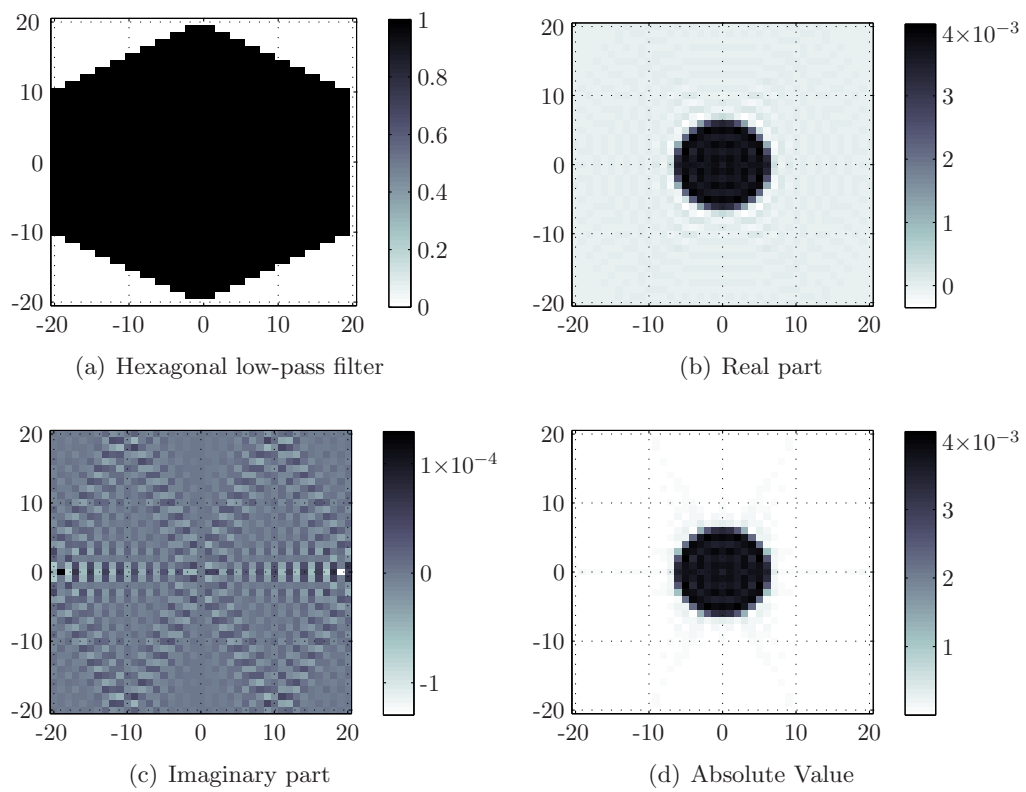


Figure 3.15: The hexagonal filter and the results from the low-pass filtering of the jinc-function.

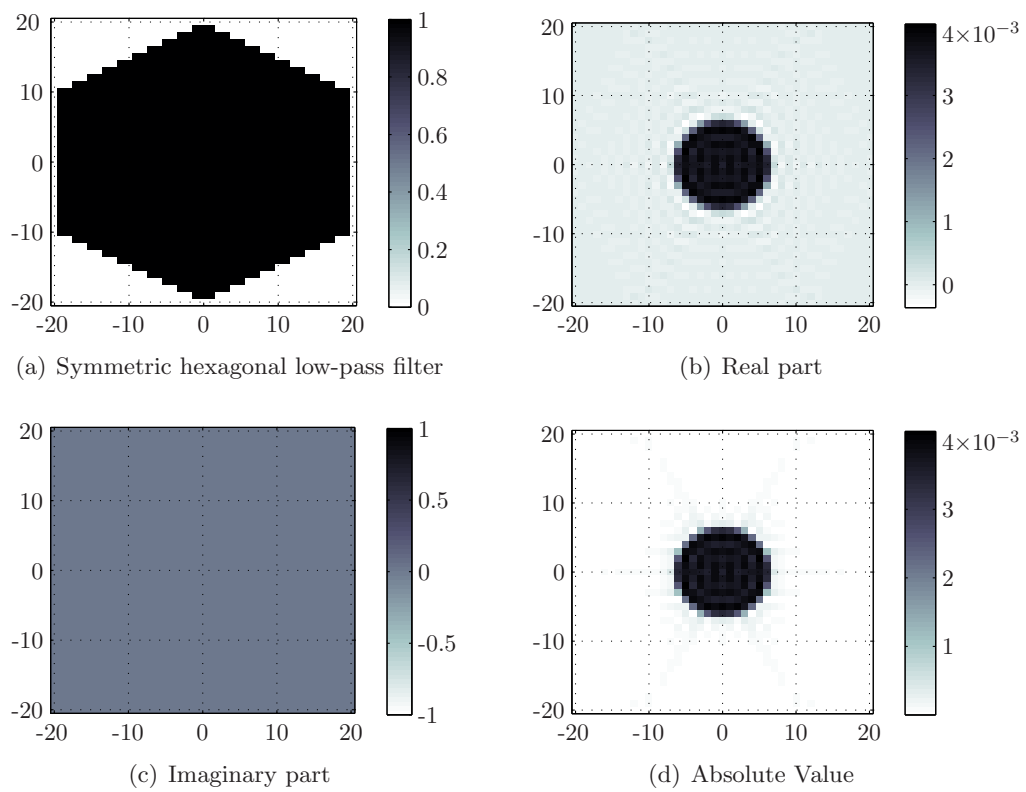


Figure 3.16: The symmetric hexagonal filter and the results from the low-pass filtering of the jinc-function.

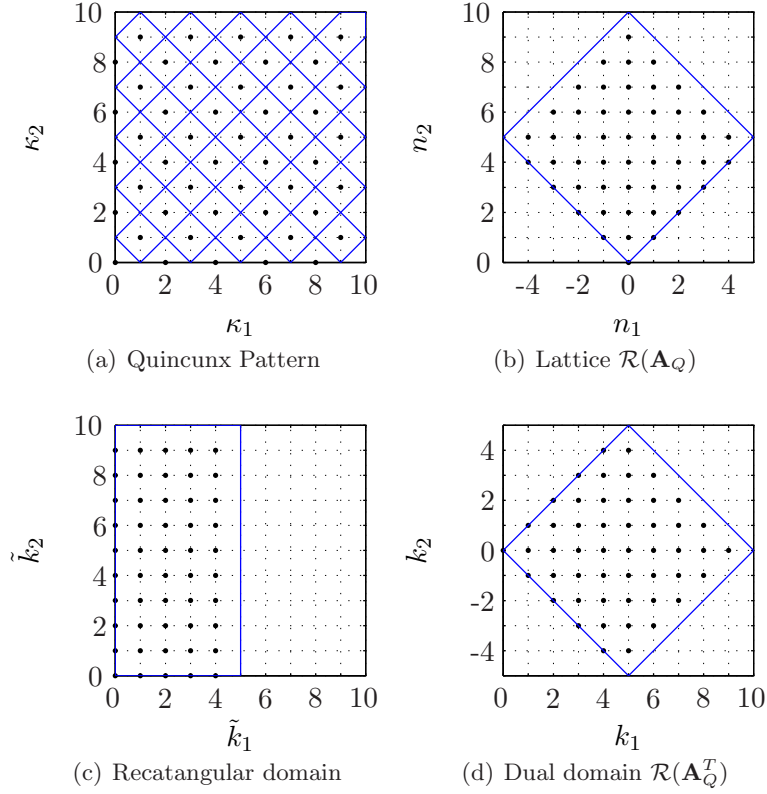


Figure 3.17: The different grids of Quincunx sampling

### 3.3 Special Sampling Patterns

Two special cases of hexagonal sampling will be presented. The Quincunx pattern which is often referred to, and a pattern which will be used for sampling seismic waves.

#### 3.3.1 Quincunx Sampling

The Quincunx sampling pattern is used in many applications, for example in televisions, because it creates just enough disorder so the eyes do not realize that the signal is discrete. The pattern has its name as the symbol for “five” on the playing dices, this pattern is shown in Figure 3.17(a). The pattern is generated by the matrix

$$\mathbf{V}_Q = \begin{pmatrix} 1 & -1 \\ 1 & 1 \end{pmatrix}. \quad (3.35)$$

In Figure 3.17(a) there are 50 points, and by multiplying these with the matrix  $\frac{1}{2}\mathbf{A}_Q$ , which is a 45 degree rotation and expansion counterclockwise, the lattice is given as  $\mathcal{R}(\mathbf{A}_{Q_5})$ , where

$$\mathbf{A}_{Q_5} = \begin{pmatrix} 5 & -5 \\ 5 & 5 \end{pmatrix}. \quad (3.36)$$

This is plotted in Figure 3.17(b) and the points fit on the rectangular lattice lying behind which makes it easy to plot functions on this lattice. The general Quincunx lattice can be expressed as

$$\mathbf{A}_{Q_N} = \begin{pmatrix} N & -N \\ N & N \end{pmatrix} = N \begin{pmatrix} 1 & -1 \\ 1 & 1 \end{pmatrix} \quad (3.37)$$

and the Smith normal form is

$$\mathbf{A}_{Q_N} = N\mathbf{A}_Q = \begin{pmatrix} -1 & -1 \\ 1 & 0 \end{pmatrix} \left( N \begin{pmatrix} 1 & 0 \\ 0 & 2 \end{pmatrix} \right) \begin{pmatrix} 1 & 1 \\ -1 & 0 \end{pmatrix} = \mathbf{P}(N\mathbf{D})\mathbf{Q}. \quad (3.38)$$

The Smith normal form gives the coordinate transformations  $\Gamma$ , and the diagonal period is plotted in 3.17(c). Moreover these points can be mapped to the dual lattice as shown in Figure 3.17(d). An advantage with this special pattern is that the rotation yield integer sampling points on a rectangular period, and interpolation is not needed. The 45 degree rotation only contracts or expands the area with a factor 2, so multiplying the rotation matrix with this factor gives integers.

### 3.3.2 Diamond Sampling

Another special case of hexagonal sampling will be referred to as Diamond sampling, because its periodicity in Fourier domain resembles the diamond on playing cards. In two dimensions this can be defined by the matrix

$$\mathbf{A}_{a,b} = \begin{pmatrix} a & -a \\ b & b \end{pmatrix} \quad (3.39)$$

where  $a, b \in \mathbb{Z}$ .

In Figure 3.18(a) the diamond lattice given by  $\mathbf{A}_{2,5}$  is plotted. This has 20 sampling points and its dual lattice  $\mathbf{A}_{2,5}^T$  is shown in Figure 3.18(b). To find the pattern in dual domain corresponding to this matrix, the coordinate transformation  $\boldsymbol{\kappa} = \mathbf{A}_{2,5}^{-T} \mathbf{k}$  results in points in  $\mathcal{R}(\mathbf{I})$ . The transformation matrix is given as

$$\mathbf{A}_{2,5}^{-T} = \frac{1}{10} \begin{pmatrix} 5 & 2 \\ -5 & 2 \end{pmatrix}, \quad (3.40)$$

and by multiplying this by a factor 10

$$10\mathbf{A}_{2,5}^{-T} = \begin{pmatrix} 2 & 1 \\ -2 & 1 \end{pmatrix}. \quad (3.41)$$

If this matrix is used for rotation, the sampling points will have the rectangular period given by the matrix

$$\mathbf{N} = \mathbf{A}_{2,5}^T 10\mathbf{A}_{2,5}^{-T} = \begin{pmatrix} 8 & 0 \\ 0 & 10 \end{pmatrix}. \quad (3.42)$$



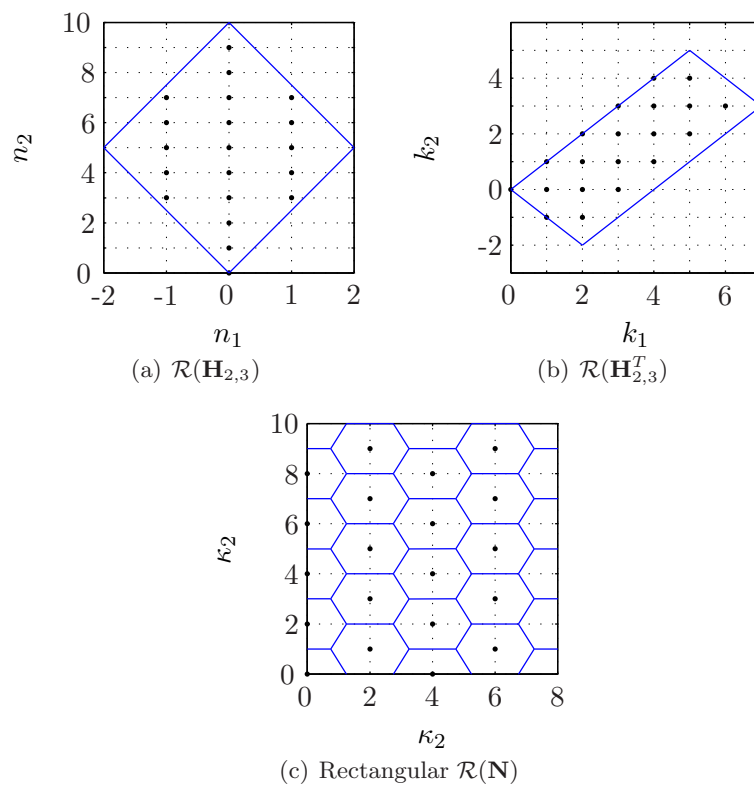


Figure 3.18: The Diamond sampling grid

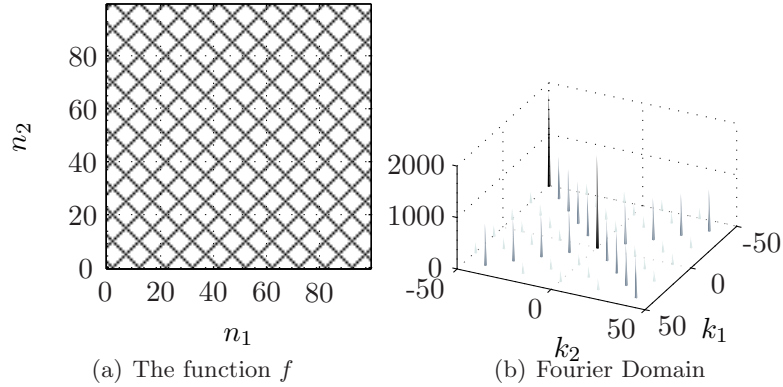


Figure 3.19: The signal and its Fourier transform

This period is plotted in Figure 3.18(c) and the points hit the integer grid lying behind this lattice. This is a special example, but in many cases this is possible, and it makes the calculations and plotting much simpler.

The Diamond sampling is equivalent to the Hexagonal sampling since any non singular integer matrix can be transformed to Hermite normal form, see A.6. This is illustrated by the blue curve enclosing the sampling points (Voronoi cells) in Figure 3.18(a). The transformation to Hermite normal form is unimodular, the determinant of the transform matrix is  $\pm 1$ , and therefore it is possible to have sampling points in a similar period as in Section 3.2.2.

### 3.4 2D Sampling and Filtering of a Signal

A function  $f$  is defined on a rectangular lattice given by  $\mathbf{N} = \text{diag}(100, 100)$ , Figure 3.19(a). Its Fourier transform is plotted in Figure 3.19(b). Fourier domain is periodic, and by shifting  $k_2$ , the horizontal axis, from  $[-50, 50]$  to the interval  $[0, 100]$ , Figure 3.20(a), it is apparent that a more efficient sampling could be the Quincunx pattern. This lattice is given by the periodicity matrix

$$\mathbf{A}_{\mathbf{Q}_{50}} = \begin{pmatrix} 50 & -50 \\ 50 & 50 \end{pmatrix}, \quad (3.43)$$

and points in dual domain has the periodicity  $\mathbf{A}_{\mathbf{Q}_{50}}^T$ . By rotating this, the Quincunx pattern is generated by the matrix

$$\mathbf{V}_Q = \begin{pmatrix} 1 & 1 \\ -1 & 1 \end{pmatrix}, \quad (3.44)$$

which gives a pattern that hits all the black lines in Figure 3.19(a). The Smith normal form is given by equation (3.38), and the map  $\Gamma_n$  yields Figure 3.20(b). This is Fourier transformed to Figure 3.20(c) and then mapped to the Quincunx period, Figure 3.20(d). By periodic expansion of Fourier domain it is observed that it is the same image as Figure 3.20(a). The rectangular grid has  $100 \times 100 = 10,000$  sampling points and the Quincunx has

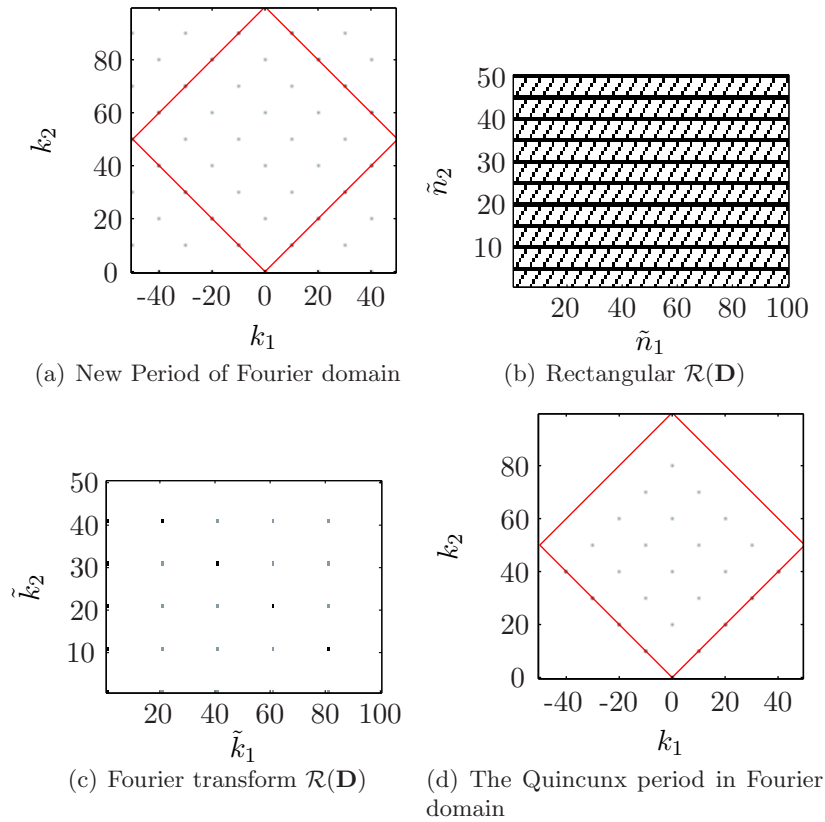


Figure 3.20: (a) The Quincunx period and (b) the rectangular space for 2D FFT. (c) The 2D FFT on rectangular period and (d) the Quincunx period

$\det(\mathbf{A}_{Q_{50}}) = 5,000$ . This shows that sampling this function with a Quincunx pattern is 50% more efficient.

Straight lines are mapped orthogonal to the initial line by the Fourier transform. Therefore the filter in Figure 3.21(a) should remove the lines in one of the directions. Transforming these points to the rectangular lattice, Figure 3.21(b), multiplication with the original Fourier domain and then inverse Fourier transform gives the image in Figure 3.21(c). Only the real part is plotted, there are some small values in between the lines, probably due to various discrete phenomena.

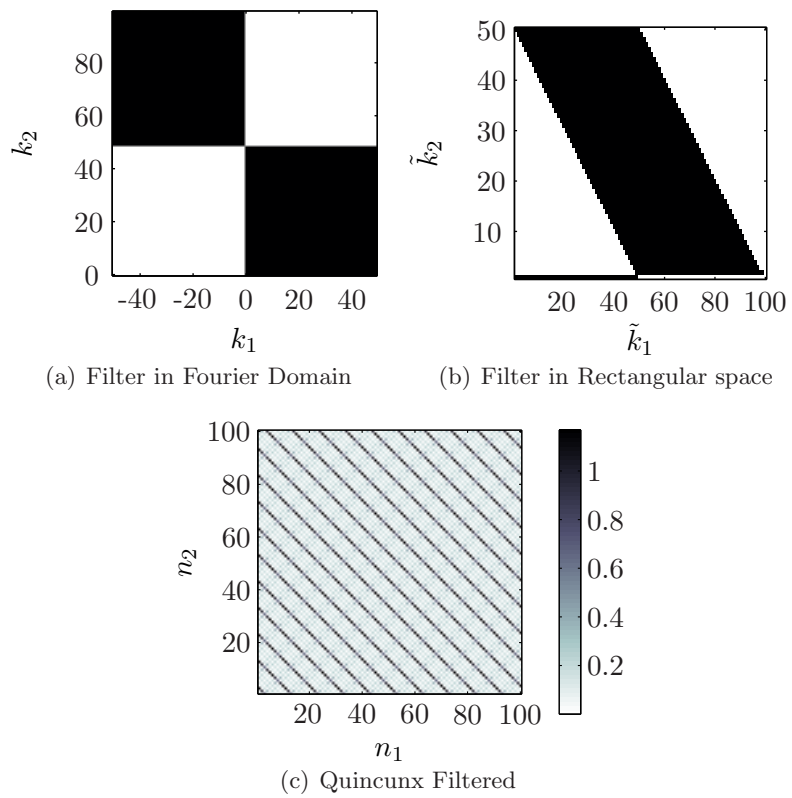


Figure 3.21: Filtering of the function  $f$

# Chapter 4

## Seismic Waves

### 4.1 The Acoustic Wave Equation

Let  $p = p(x, y, z, t) = p(\mathbf{r}, t)$  be the wavefield in 3D where  $x, y, z$  are the coordinates in space and  $t$  is time. For an isotropic medium the acoustic wave equation is given as

$$\rho \nabla \cdot \left( \frac{1}{\rho} \nabla p \right) = \frac{1}{c^2} \frac{\partial^2 p}{\partial t^2}, \quad (4.1)$$

where  $c = c(\mathbf{r})$  is the P-wave velocity and  $\rho = \rho(\mathbf{r})$  the density. Defining  $\omega$  as the angular frequency and  $\mathbf{k} = (k_x, k_y, k_z)^T$  as the wavenumber, the Fourier transform over these coordinates is defined as

$$P(\mathbf{k}, \omega) = \mathcal{F}[p(\mathbf{r}, t)] = \int \int \int \int_{-\infty}^{\infty} p(\mathbf{r}, t) e^{-i(\omega t - \mathbf{k}^T \mathbf{r})} d\mathbf{r} dt, \quad (4.2)$$

and its inverse

$$p(\mathbf{r}, t) = \frac{1}{(2\pi)^4} \int \int \int \int_{-\infty}^{\infty} P(\mathbf{k}, \omega) e^{i(\omega t - \mathbf{k}^T \mathbf{r})} d\mathbf{k} d\omega. \quad (4.3)$$

A general property of the Fourier Transformation is

$$\mathcal{F} \left[ \frac{\partial p}{\partial x} \right] = ik_x P, \quad (4.4)$$

and by assuming constant velocity  $c$  and density  $\rho$ , the wave equation can be written

$$k_x^2 P + k_y^2 P + k_z^2 P = \left( \frac{\omega}{c} \right)^2 P. \quad (4.5)$$

This results in

$$\|\mathbf{k}\|^2 = \left( \frac{\omega}{c} \right)^2 \Rightarrow \omega = c \|\mathbf{k}\| \quad (4.6)$$

where  $\|\times\|$  is the Euclidean norm. This is the dispersion relation for acoustic waves.

In a homogeneous medium with constant velocity the solution can be written

$$P(\mathbf{r}, \omega) = \frac{1}{r} e^{-i\omega r/c}, \quad \text{where } r = \|\mathbf{r}\|, \quad (4.7)$$

which is spherical waves.

## 4.2 Sampling and Aliasing

The conventional method for sampling a wavefield in 2D is by defining  $t = n\Delta t$  for  $n = 0, 1, \dots, N_t - 1$ , and  $x = m\Delta x$  for  $m = 0, 1, \dots, N_x - 1$ . The Nyquist-Shannon theorem states that to avoid aliasing the sampling interval should fulfill the inequality  $\Delta t \leq \frac{\pi}{\omega_{\max}}$ , where  $\omega_{\max}$  is the maximum angular frequency in the signal. If  $\omega_{\max} = \frac{\pi}{\Delta t}$  this frequency is called the Nyquist frequency,  $\omega_{Ny}$ . When sampling in space there is a Nyquist frequency or wavenumber in all directions.

Letting  $\Delta t = \frac{\pi}{\omega_{Ny}}$  and  $\Delta x = \frac{\pi}{k_{xNy}}$ , gives the periodicity in Fourier domain by the intervals  $\omega \in [-\omega_{Ny}, \omega_{Ny}]$  and  $k_x \in [-k_{xNy}, k_{xNy}]$ . This is a rectangular period and the integer periodicity matrix in Fourier and spatial domain is

$$\mathbf{N} = \mathbf{N}^T = \begin{pmatrix} N_x & 0 \\ 0 & N_t \end{pmatrix}, \quad (4.8)$$

which has a total of  $\det(\mathbf{N}) = N_x N_t$  sampling points.

A wavefield propagating in coordinates  $x$  and  $z$ , has vertical wavenumber  $k_z$ ,

$$k_z = \pm \sqrt{\left(\frac{\omega}{c}\right)^2 - k_x^2}. \quad (4.9)$$

For the waves to propagate downwards, the wavenumber in  $z$  direction,  $k_z$ , should be real and positive. This gives

$$|\omega| \geq c|k_x|, \quad (4.10)$$

which shows that the wavefield is limited in Fourier domain. This is illustrated in Figure 4.1, where seismogram of a point source at depth  $z = 4$  km in a homogeneous medium with velocity  $c = 2.5$  km/s is approximated by a hyperbola. Figure 4.1(b) shows that the Fourier spectrum is limited by the lines given by equation (4.10).

For a given medium with minimum velocity  $c_{\min}$  and Nyquist frequency  $\omega_{Ny}$ , the Nyquist wavenumber should be chosen  $k_{xNy} = \omega_{Ny}/c_{\min}$  to minimize the data when sampling on a rectangular grid. Using the relations between the Nyquist frequency and sampling interval gives that the sampling in  $x$  should be given  $\Delta x = c_{\min}\Delta t$ .

A periodic expansion of the wavefield in Figure 4.1 is given in Figure 4.2. The black lines illustrate the Nyquist frequency and wavenumber for rectangular sampling, the blue lines the

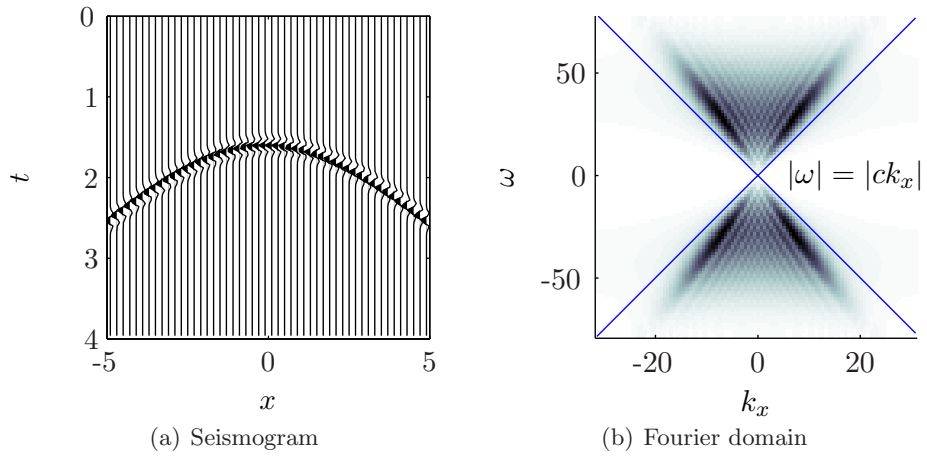


Figure 4.1: (a) A seismogram from an exploding source with depth  $z_0 = 4$  km with velocity  $c = 2.5$  km/s, and (b) its Fourier spectrum which is limited by the blue lines

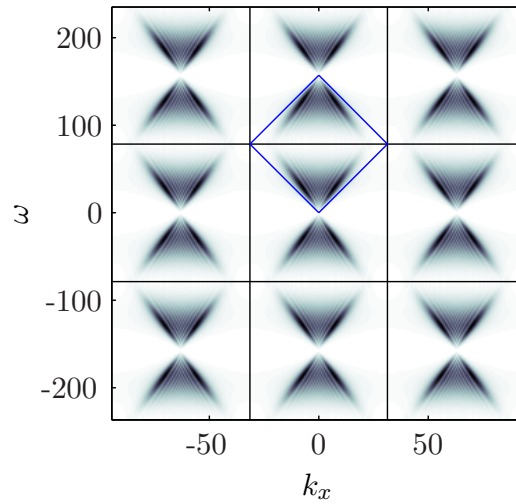


Figure 4.2: Periodic expansion of Fourier domain, black lines are the Nyquist frequencies  $k_{xNy}, \omega_{Ny}$  and the blue indicate the optimal sampling area

optimal periodicity. This Figure illustrate that a wavefield in Fourier domain will be contained in the range of a matrix given by

$$\mathbf{R}^T = \begin{pmatrix} k_{xNy} & -k_{xNy} \\ \omega_{Ny} & \omega_{Ny} \end{pmatrix}, \quad (4.11)$$

which can be written

$$\mathbf{R}^T = \begin{pmatrix} k_{xNy} & -k_{xNy} \\ ck_{xNy} & ck_{xNy} \end{pmatrix} = k_{xNy} \begin{pmatrix} 1 & -1 \\ c & c \end{pmatrix}. \quad (4.12)$$

Limiting the number of samples to even integers  $N_t$  and  $N_x$ , the Nyquist frequency and wavenumber in units of  $\Delta\omega$  and  $\Delta k_x$  are  $\frac{N_t}{2}$  and  $\frac{N_x}{2}$ . The optimal sampling area is then given by the periodicity matrix  $\mathbf{A}^T$  in Fourier domain.

$$\mathbf{A}^T = \begin{pmatrix} \frac{N_x}{2} & -\frac{N_x}{2} \\ \frac{N_t}{2} & \frac{N_t}{2} \end{pmatrix}. \quad (4.13)$$

In dual domain, time - space, this matrix is

$$\mathbf{A} = \begin{pmatrix} \frac{N_x}{2} & \frac{N_t}{2} \\ -\frac{N_x}{2} & \frac{N_t}{2} \end{pmatrix} \quad (4.14)$$

and  $\det(\mathbf{A}) = \frac{N_x N_t}{4} + \frac{N_x N_t}{4} = \frac{N_x N_t}{2}$ . Comparing with the conventional sampling, this sampling geometry preserves the wavefield with only half the samples. This is the same as the diamond sampling geometry from Section 3.3.2, where the sampling points in time offset domain is integer.

For odd number of samples the Nyquist frequency and wavenumber in units of the sampling interval can be defined  $(N_x - 1)/2$  and  $(N_t - 1)/2$ . This does not result in such a simple number of sampling points as for even sampling, but is also  $\approx 50\%$  more efficient.

Similar arguments can be made for 3D waves. The Fourier spectrum is bounded by

$$|\omega| \geq \pm c \sqrt{k_x^2 + k_y^2}, \quad (4.15)$$

which is a cone, Figure 4.3(a). The optimal sampling would then be to sample within a area bounded by two hexagonal pyramids. It is not possible to express such an volume with this definition of the periodicity matrices. The periodicity matrix for sampling in 3D with coordinates in Fourier domain,  $(k_x, k_y, \omega)^T$ , can be expressed

$$\mathbf{A}^T = \begin{pmatrix} N_x/2 & -N_x/2 & 0 \\ 0 & 0 & N_y \\ N_t/2 & N_t/2 & 0 \end{pmatrix}. \quad (4.16)$$

The range of this matrix is a volume in  $(k_x, k_y, \omega)$  space, and by shifting half of the  $k_y$  wavenumbers to negative this is plotted over the bandwidth of acoustic waves in Figure 4.3(b). This has  $\det(\mathbf{A}) = N_x N_y N_t / 2$  sampling points which is 50% less than the conventional sampling with  $N_x N_y N_t$  points.



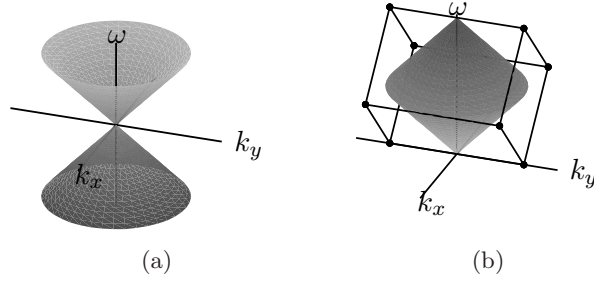


Figure 4.3: (a) The 3D bandwidth of acoustic waves and (b) the periodicity with half the sampling points.

#### 4.2.1 Example of 2D Sampling

The seismogram in Figure 4.4(a) is the same as in Figure 4.1(a) and is sampled on a lattice given by the intervals  $\Delta t = 0.03$  s and  $\Delta x = c\Delta t = 0.1$  km. The optimal sampling is given by the periodicity matrix in equation (4.12), with  $k_{x_{Ny}} \approx 31.4$  rad/km and  $\omega_{Ny} \approx 78.5$  rad/s. Figure 4.4(b) shows the absolute value of Fourier domain shifted from  $[-\omega_{Ny}, \omega_{Ny}]$  to  $[0, 2\omega_{Ny}]$ . The blue lines illustrate the optimal sampling periodicity. The conventional rectangular sampling have  $N_t = N_x = 100$  sampling points, therefore the periodicity matrix in units of  $\Delta x$  and  $\Delta t$  becomes

$$\mathbf{A}^T = \begin{pmatrix} 50 & -50 \\ 50 & 50 \end{pmatrix}. \quad (4.17)$$

This matrix is equal to the Quincunx periodicity matrix  $\mathbf{A}_{Q_{50}}$  from Section 3.3.1 and the Smith normal form is given

$$\mathbf{A}_{Q_{50}} = \mathbf{PDQ} = \begin{pmatrix} -1 & -1 \\ 1 & 0 \end{pmatrix} \begin{pmatrix} 50 & 0 \\ 0 & 100 \end{pmatrix} \begin{pmatrix} 1 & 1 \\ -1 & 0 \end{pmatrix}. \quad (4.18)$$

Now sampling inside the  $\mathcal{R}(\mathbf{A}^T)$  in Fourier domain and calculating the coordinate transformation

$$\Gamma_k : \tilde{\mathbf{k}} = \mathbf{Q}^{-1}\mathbf{k}, \quad (4.19)$$

results in the function  $f(\tilde{\mathbf{k}})$ , Figure 4.4(c). The function is on a rectangular grid and IFFT results in Figure 4.4(d).

The next step to get the image in time-space, is to map the function to  $\mathcal{R}(\mathbf{A})$ , this by

$$\Gamma_n^{-1} : \mathbf{n} = \mathbf{P}\tilde{\mathbf{n}}, \quad (4.20)$$

see Figure 4.4(e).

The coordinate transform

$$\boldsymbol{\eta} = \mathbf{TA}^{-1}\mathbf{n} \quad (4.21)$$

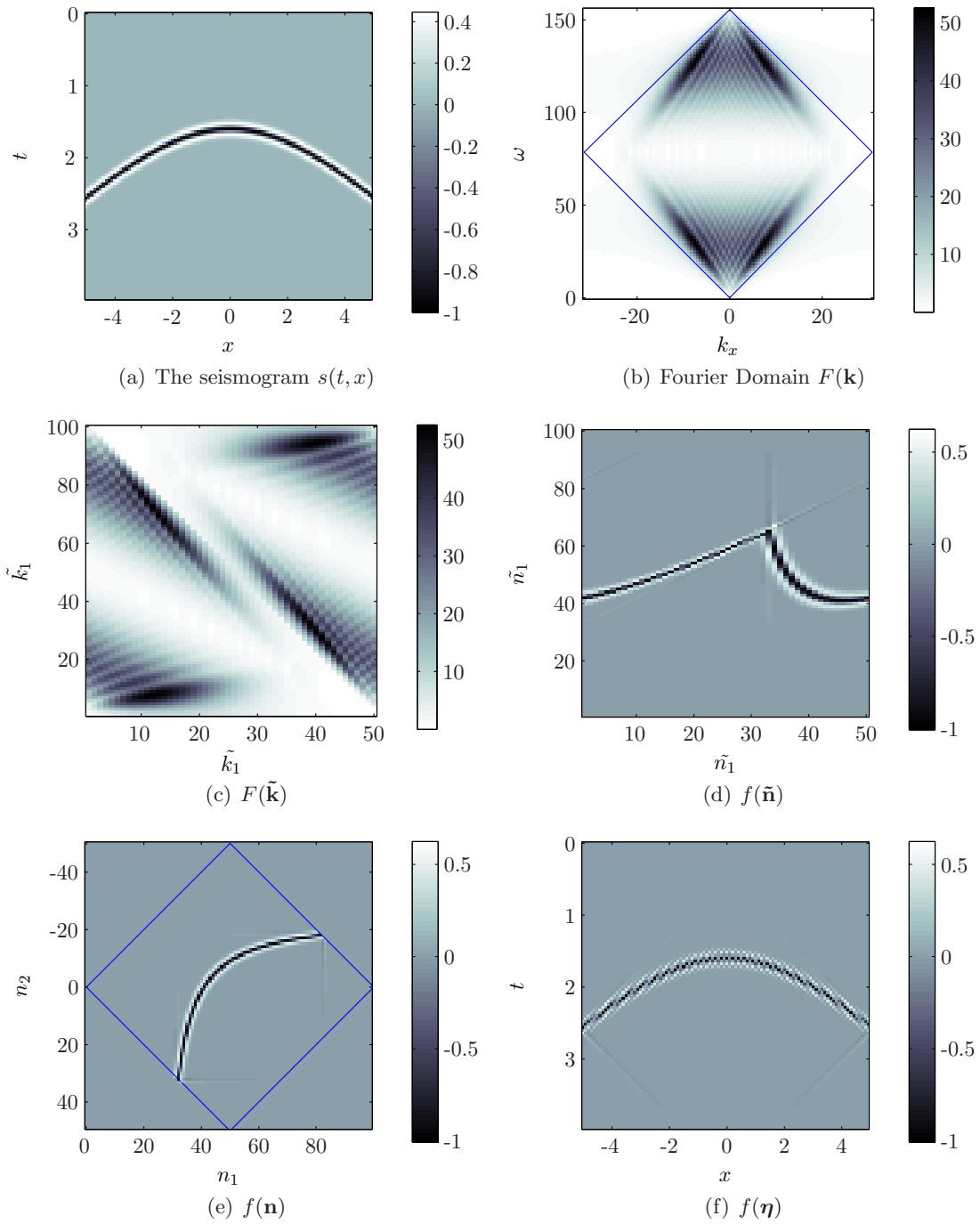


Figure 4.4: Example, optimal sampling of a wavefield

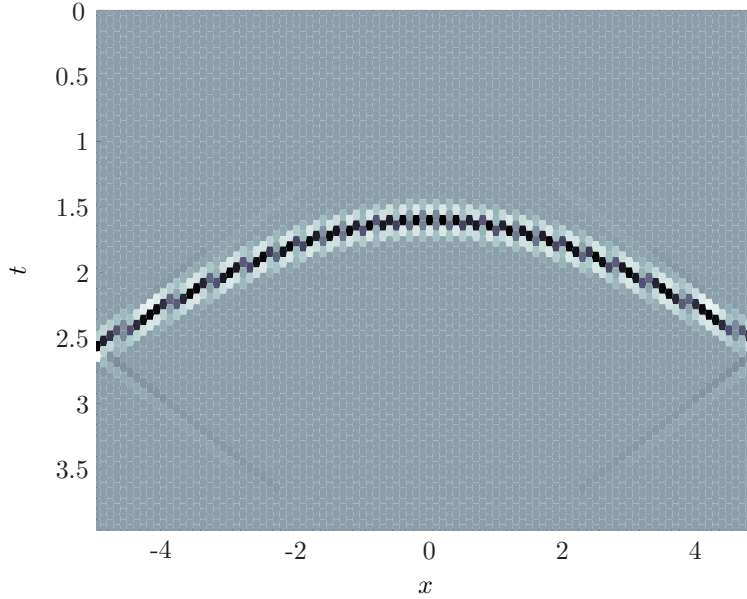


Figure 4.5:  $f(\boldsymbol{\eta})$  in hexagonal Voronoi cells

where  $\mathbf{T} = \text{diag}(N_x \Delta x, N_t \Delta t)$ , maps the sampling points to a rectangular period on the same interval as the seismogram in Figure 4.4(a). The downsampled seismogram is plotted on this lattice, Figure 4.4(f). The sampling points become integers as in Section 3.3.2, and the points without value are plotted as zeros.

Another method for displaying images on a diamond or hexagonal lattice is to fill the Voronoi cells which the lattice generates, with colors representing the functions value. Figure 4.5 shows such a plot of the seismogram, it can be observed that the cells are hexagonal. This is a good approach for displaying images on hexagonal lattices since it does not involve interpolation, see Appendix B for details.

The result of the downsampling clearly shows that some artifacts are present. Because sampling within an area given by  $\mathcal{R}(\mathbf{A}^T)$ , is a low-pass filtering. It is preferable to downsample in time-offset domain, because these artifacts will be avoided. The low-pass filtering when downsampling in Fourier domain, will be investigated in the next section.

### 4.3 Bow-Tie Filter and Sampling

The sampling scheme defined in Section 4.2 is a low pass filter which resembles a velocity filter, often referred to as a bow-tie filter. This filter is generally constructed in 2D to remove alias and noise which is outside the region defined by the  $\mathcal{R}(\mathbf{A})$  from Section 4.2.

The impulse response of such a filter is

$$g(x, t) = \frac{1}{4\pi^2} \int_{-\Omega}^{\Omega} \text{sign}(\omega) e^{i\omega t} d\omega \int_{-\kappa}^{\kappa} e^{-ixk_x} dk_x \quad (4.22)$$

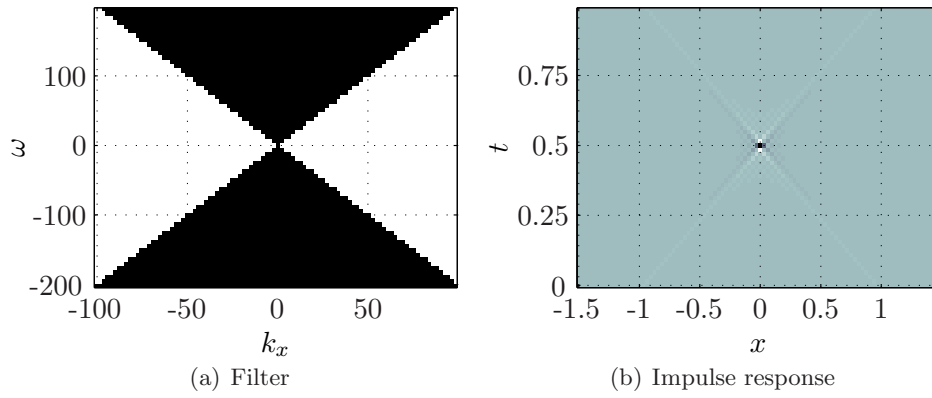


Figure 4.6: (a) The bow tie filter with velocity  $c = 2$  km/s, (b) the impulse response

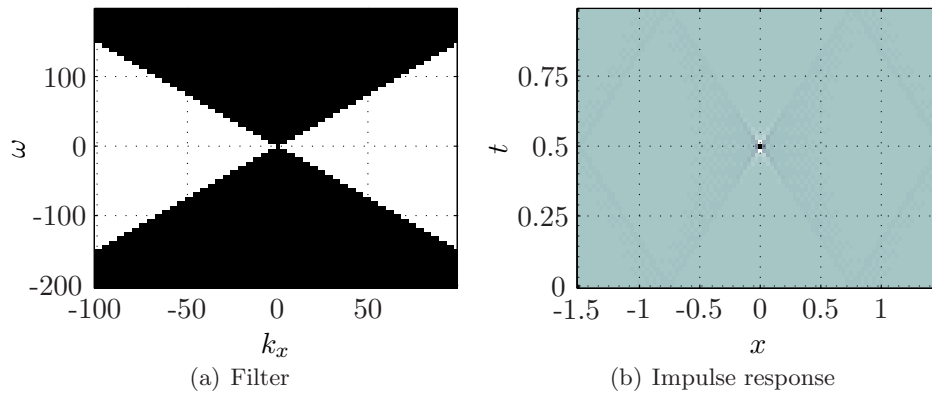


Figure 4.7: (a) The bow tie filter with velocity  $c = 1.5$  km/s resembles a hexagonal filter and (b) the impulse response

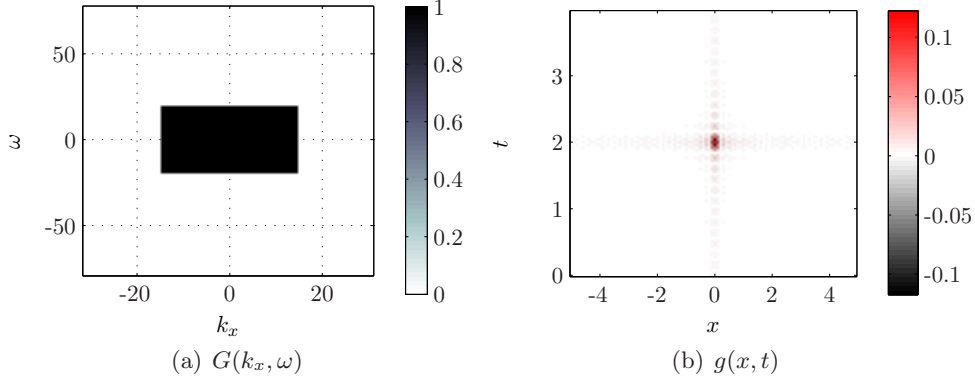


Figure 4.8: (a) A low-pass filter in Fourier domain, (b) the impulse response of the filter

where  $\kappa = \omega/V$ ,  $V$  the cutoff velocity and  $\Omega$  the frequency band. These integrals can be solved by use of the shift theorem, and more explicit the impulse response is

$$g(x, t) = -\frac{1}{2}\tilde{h}(t) * [\tilde{\delta}(t - x/V) - \tilde{\delta}(t + x/V)], \quad (4.23)$$

where  $\tilde{\delta}(t)$  is a  $\Omega$  band limited  $\delta$ -function and  $\tilde{h}(t) = \mathcal{H}[\tilde{\delta}(t)]$  is the Hilbert transformation. An example of a bow tie filter with  $V = 2$  km/s is given in Figure 4.6(a), and its impulse response in 4.6(b). If  $V = c_{\min}$ , the impulse response is somewhat equivalent to sampling a seismic wave on the lattice given by the optimal sampling matrix from Section 4.2.

When implementing this filter there is the general problem of oscillations of the impulse response. To reduce this, smoothing of the edges would be preferable. Before downsampling to a lattice with less sampling points such a filtering should be done.

An interesting result from this is if  $V$  is chosen smaller than  $c_{\min}$ , the filter can be interpreted as a period of the hexagonal filter from Section 3.2.3. A filter with  $V = 1.5$  km/s  $< c_{\min}$  is plotted in Figure 4.7(a), which by changing period is a hexagon. The impulse response, Figure 4.7(b), shows that the oscillations actually have a hexagonal shape. This is a result of alias, the lines of the impulse response map back around the period.

#### 4.4 Filtering in $(k_x, \omega)$ -domain

The seismic section in Figure 4.1(a) is given,  $s(x, t)$ , with maximum angular frequency and wavenumber  $\omega_{Ny}$  and  $k_{xNy}$ . A low pass filter which passes angular frequencies in a band  $\Omega$  and wavenumbers in a band  $\Lambda$  can be defined as

$$F(k_x, \omega) = \begin{cases} 1 & \text{if } \omega \in \Omega \text{ and } k_x \in \Lambda \\ 0 & \text{otherwise} \end{cases}. \quad (4.24)$$

The impulse response is a 2D sinc function, which oscillates from the center of the domain. An example of the filter and its impulse response is given in Figure 4.8(a,b), here  $\Omega = \{\omega \mid |\omega| <$

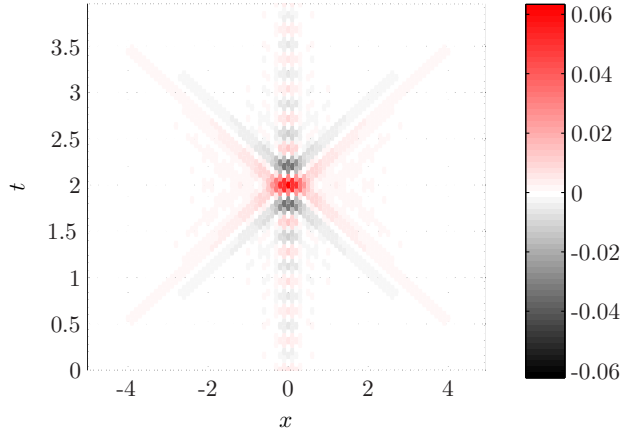


Figure 4.9: The impulse response of  $F(k_x, \omega)$  sampled with  $\mathbf{A}$

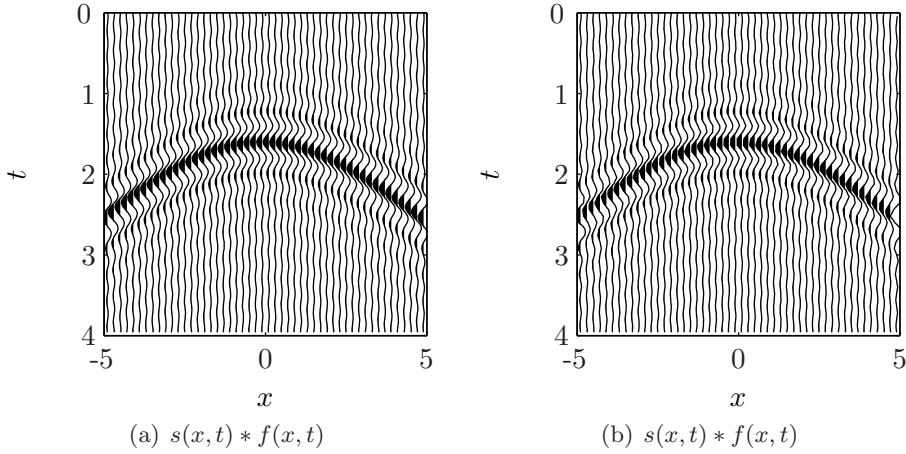


Figure 4.10: (a) Low-pass filtering of  $s(x, t)$  and (b) the same filtering with optimal sampling.

30 rad/s} and  $\Lambda = \{k_x | |k_x| < 15 \text{ rad/km}\}$ . The sampling scheme is given  $\Delta t = 0.04 \text{ s}$ ,  $\Delta x = c\Delta t$ ,  $c = 2.5 \text{ km}$  which is the velocity of the wavefield  $s(x, t)$ . This gives  $N_t = N_x = 100$ , when the period is  $T = 4 \text{ s}$  and  $x$  is sampled from  $-5 \text{ km}$  to  $5 \text{ km}$ .

By using the periodicity matrix  $\mathbf{A}$  from equation (4.14), the impulse response changes because of the different periodicity in time space domain, Figure 4.9. The oscillating lines are rotated compared to the rectangular sampled impulse response. This illustrates that the change of sampling grid, changes the periodicity in both domains and different alias effects is present.

The image is generated by filling the hexagonal cells enclosing the sampling points, Voronoi cells, see Appendix B. The rectangular sampling had a total of  $N_t N_x = 10,000$  sampling points while using the periodicity matrix  $\mathbf{A}$ , results in half the points,  $\det(\mathbf{A}) = 5,000$ .

This filter is applied to  $s(x, t)$  in Fourier domain and the result is plotted in 4.10(a). Comparing to 4.1(a) the main observation is that the wavelet contains lower frequencies. The same filtering is applied by sampling the wavefield and filter with the matrix  $\mathbf{A}$ . The result

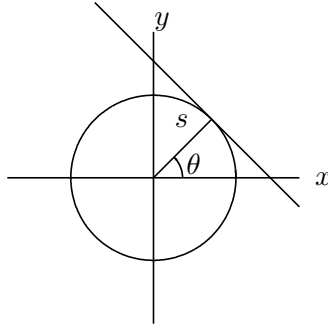


Figure 4.11: The Radon transform

is upsampled to the initial grid after the filtering. This is plotted in Figure 4.10(b). The upsampling is done by using MATLAB's implemented cubic spline interpolation. The results of the filtering are basically the same, of course by careful inspection some differences will exist.

This example shows that non-rectangular sampling theory can be used in seismic processing, resulting in only half the data points.

## 4.5 The Radon Transform and Slant Stacks

The Radon Transform in its original form was introduced by Johan Radon in 1917. The transform has a wide range of applications for example in medicine (X-ray and CT), in astronomy and in optics. Figure 4.11 shows that a ray can be defined

$$s = x \cos \theta + y \sin \theta, \quad (4.25)$$

and the Radon Transform is defined as the integral along these rays,

$$g(s, \theta) = \mathcal{R}[f] = \int_{-\infty}^{\infty} \int_{-\infty}^{\infty} f(x, y) \delta(s - x \cos \theta - y \sin \theta) dx dy. \quad (4.26)$$

The inversion of this transform is essential in almost all its applications and general references on this subject is Deans (1983) and Jain (1989).

Only a finite number of projections can be calculated, and to analyze how many is necessary to get the complete image, Rattey and Lindgren (1981) finds the Fourier spectrum of the Radon transforms impulse response. An impulse at the point  $(a, b)$  can be given by the Dirac delta function

$$f(x, y) = \delta(x - a, y - b), \quad (4.27)$$

for  $a, b \neq 0$ . The Radon transform is given

$$g(s, \theta) = \delta(s - a \cos \theta - b \sin \theta), \quad (4.28)$$

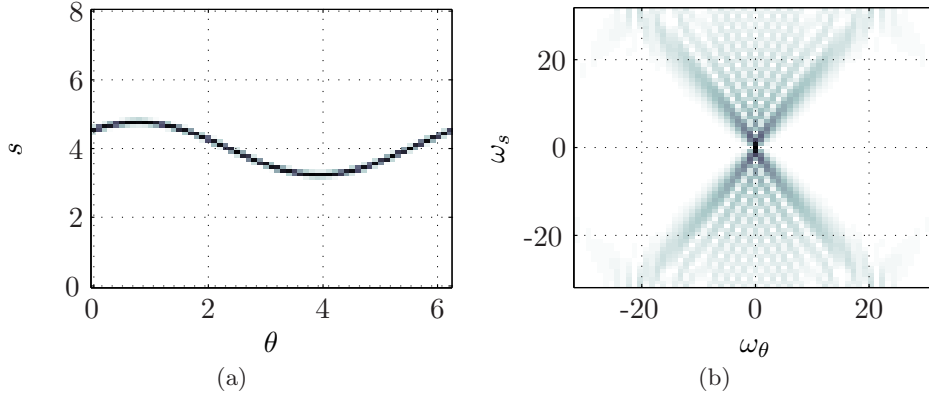


Figure 4.12: (a) The Radon transform of a point impulse in  $(a, b) = (2, 3)$  and (b) the Fourier transform of Radon domain

which is unequal to zero when

$$s = a \cos \theta + b \sin \theta = r \cos(\theta - \theta_0), \quad r = \sqrt{a^2 + b^2}, \quad \theta_0 = \arctan(b/a). \quad (4.29)$$

Transforming the  $\delta$ -function gives insight into the Radon Transform since any function  $f$  can be expressed as a continuous sum of impulses

$$f(x, y) = \int \int_{-\infty}^{\infty} f(a, b) \delta(x - a, y - b) da db. \quad (4.30)$$

This shows that the Fourier transform of equation (4.28) gives a band region not only for the impulse response but also for a general function. From equation (4.26), the Radon transform is  $2\pi$  periodic,  $g(s, \theta) = g(s, \theta + 2n\pi)$  for  $n \in \mathbb{Z}$ . Defining  $(s, \theta) \rightarrow (\omega_s, \omega_\theta)$  as Fourier pairs gives

$$\begin{aligned} G(\omega_s, \omega_\theta) &= \int_0^{2\pi} \int_{-\infty}^{\infty} \delta(s - r \cos(\theta - \theta_0)) e^{-i(\omega_s s + \omega_\theta \theta)} d\theta ds \\ &= \int_0^{2\pi} e^{-i\omega_s r \cos(\theta - \theta_0)} e^{-i\omega_\theta \theta} d\theta. \end{aligned} \quad (4.31)$$

This integral can be written as the Fourier series

$$G(\omega_s, \omega_\theta) = 2\pi \sum_{m=-\infty}^{\infty} e^{-im(\pi/2 + \phi_0)} J_m(r\omega_s) \delta(\omega_\theta - m), \quad (4.32)$$

where  $J_m(r\omega_s)$  is the  $m$ 'th order Bessel function of the first kind. Rattey and Lindgren (1981) further show that the Fourier spectrum is approximately zero for  $|\omega| < \lfloor |r\omega_s| \rfloor + 1$ , since the Bessel functions have bandwidth  $2(|r\omega_s| + 1) + 1$ . This is an efficient bandwidth for the Radon domain, which yields the number of projections necessary to get the image.



The Radon Transform of an impulse in  $(a, b) = (2, 3)$  is plotted in Figure 4.12(a), and the Fourier Transform of that in Figure 4.12(b). This shows that Radon domain would be most efficiently sampled with a hexagonal geometry.

By making two assumptions on the initial function  $f$ ,

- $f(x, y) \approx 0$  for  $x^2 + y^2 > R_M^2$
- $F(\omega_x, \omega_y) \approx 0$  for  $\omega_x^2 + \omega_y^2 > W_M^2$ ,

where  $R_M$  is the radius of a circular element in space and  $W_M$  is the bandwidth, Rattey and Lindgren (1981) shows that the hexagonal sampling scheme requires

$$N_h \approx \frac{1}{\pi}(R_M W_M)^2 \quad (4.33)$$

sampling points for large space-bandwidth products. The rectangular sampling theorems, using Nyquist in both variables, result in

$$N_r \approx \frac{2}{\pi}(R_M W_M)^2 \quad (4.34)$$

and the hexagonal sampling requirement results in only half the samples.

#### 4.5.1 The Linear Radon Transform

In geophysics the transform is called slant stacks,  $\tau - p$  transform, or the linear Radon transform (Schultz and Claerbout, 1978), and is defined as

$$\begin{aligned} \mathcal{R}[s(x, t)] &= \int \int_{-\infty}^{\infty} s(x, t) \delta(t - \tau - px) dx dt \\ &= \int_{-\infty}^{\infty} s(x, \tau + px) dx, \end{aligned} \quad (4.35)$$

which is the sum over all straight lines  $t = \tau + px$  where  $\tau$  is intercept time and  $p$  the ray-parameter or slowness,  $p = 1/c$ . This transform is often used for multiple elimination and there are examples of migrating data in this domain. The transformation maps linear events to points and point impulses to lines, Figure 4.13(a) and 4.13(b) illustrates this. An impulse in  $(x_0, t_0)$  is given by

$$s(x, t) = \delta(x - x_0) \delta(t - t_0)$$

and the Radon transform is

$$\mathcal{R}[s(x, t)] = \delta(\tau - t_0 + px_0), \quad (4.36)$$

which is a straight line,  $t_0 = \tau + px_0$ . For any given time curve  $t_0 = t_0(x)$  the Radon transform is the envelope of such lines. By defining  $\mathcal{F}(p, \tau; x_0) = 0$  the envelope is given as  $\mathcal{F} = \partial\mathcal{F}/\partial x_0 = 0$  and the ray-parameter is given  $p = \partial t_0 / \partial x_0$ .

Acoustic waves from a point source at depth  $z_0$  are generally modeled by a hyperbola given as

$$(ct_0)^2 = x_0^2 + z_0^2 \quad (4.37)$$

where  $(x_0, t_0)$  is a point on the hyperbola. This gives

$$\begin{aligned} p &= \frac{\partial t_0}{\partial x_0} = \frac{x_0}{c^2 t_0}, \\ \tau &= t_0 - px_0 = \frac{z_0^2}{c^2 t_0}, \end{aligned} \quad (4.38)$$

and elimination of  $x_0$  yields an ellipse in  $\tau - p$  domain,

$$(cp)^2 + \left(\frac{c\tau}{z_0}\right)^2 = 1. \quad (4.39)$$

The Fourier transformation of a Dirac  $\delta$ -ellipse could then be an indication of optimal sampling if the transform of hyperbolas is band limited. An analytic formula is derived by Guizar-Sicairos and Gutierrez-Vega (2004), but this does not imply any band limitations on the transform.

Another approach is to Fourier transform the  $\tau - p$  transforms impulse response, equation (4.36). This is given

$$\begin{aligned} R(\omega_p, \omega_\tau) &= \mathcal{F}[\mathcal{R}[s(x, t)]] = \int \int_{-\infty}^{\infty} \delta(\tau - t_0 + px_0) e^{-i(p\omega_p + \tau\omega_\tau)} dp d\tau \\ &= e^{-i\omega_\tau t_0} \int_{-\infty}^{\infty} e^{-ip(\omega_p - \omega_\tau x_0)} dp, \end{aligned} \quad (4.40)$$

which is the Dirac  $\delta$ -function

$$R(\omega_p, \omega_\tau) = 2\pi e^{-i\omega_\tau t_0} \delta(\omega_p - \omega_\tau x_0), \quad (4.41)$$

(Folland, 2009). This shows that the Fourier transform of the  $\tau - p$  transform of an impulse in  $(x_0, t_0)$ , is a straight line given by  $\omega_\tau = \omega_p/x_0$ .

The  $\tau - p$  transform is generally evaluated on discrete lattices, of finite length, say,  $x_{\min} \leq x \leq x_{\max}$  and  $t_{\min} \leq t \leq t_{\max}$ . Since any function can be represented by a sum of impulses this introduce a bandwidth for the discrete slant stack given by the lines

$$\mathcal{L}_1 : \omega_p = \omega_\tau x_{\max} \quad \text{and} \quad \mathcal{L}_2 : \omega_p = \omega_\tau x_{\min}. \quad (4.42)$$

With this bandwidth and a symmetric sampling in  $x$ , so that  $x_{\max} = -x_{\min}$ , the optimal sampling is a diamond scheme, see Section 3.3.2. The periodicity matrix is given by

$$\mathbf{R}^T = \begin{pmatrix} \omega_{pNy} & -\omega_{pNy} \\ \omega_{\tau Ny} & \omega_{\tau Ny} \end{pmatrix} = \omega_{\tau Ny} \begin{pmatrix} x_{\max} & -x_{\max} \\ 1 & 1 \end{pmatrix}. \quad (4.43)$$

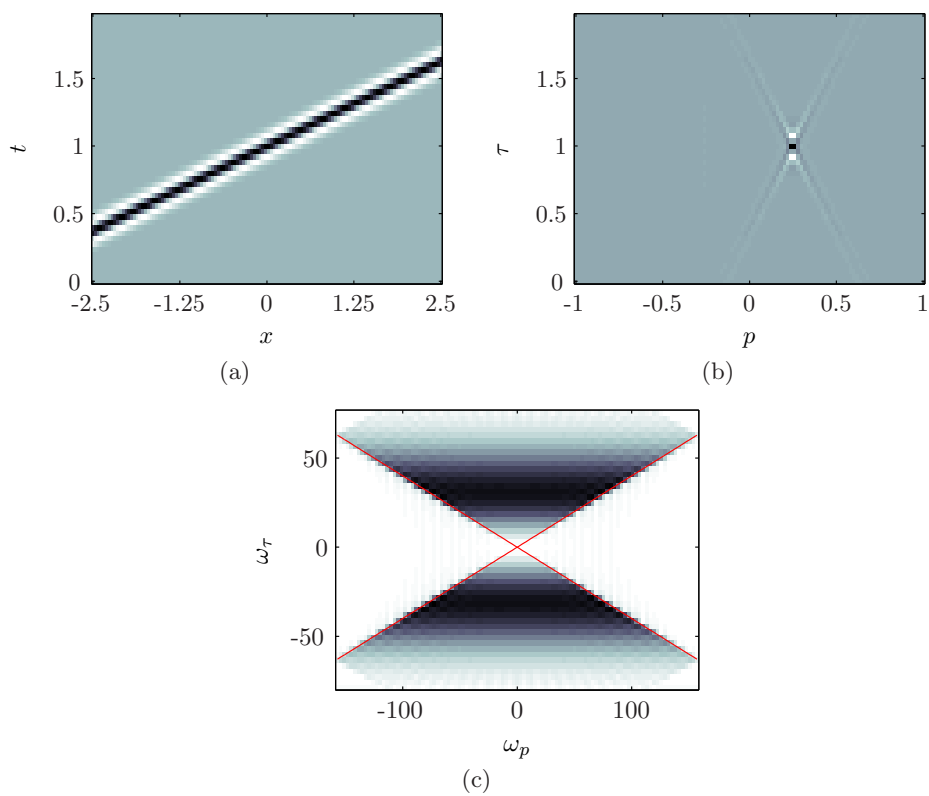


Figure 4.13: (a) A seismogram of a plane wave, (b) the Radon domain and (c) the Fourier transform of Radon domain, the red lines indicate the bandwidth

where  $\omega_{\tau N_y} = \omega_{N_y}$ , since  $\tau = t$ . The sampling area is then given  $\det(\mathbf{R}) = 2\omega_{p N_y} \omega_{\tau N_y}$  which is one half the area of conventional sampling,  $4\omega_{p N_y} \omega_{\tau N_y}$ . This is illustrated in Figure 4.13(c), where the  $\tau - p$  domain from Figure 4.13(b) is Fourier transformed. These band limits are also shown by Bardan (1989) but with a different approach.

### 4.5.2 The Parabolic Radon Transform

The Radon transform can be generalized to curves other than straight lines. The most common in seismic processing is the Parabolic Radon Transform defined by

$$\mathcal{R}[f(x, t)] = \int_{-\infty}^{\infty} f(x, \tau + qx^2) dx, \quad (4.44)$$

(Yilmaz and Doherty, 2001). The impulse response is

$$\mathcal{R}[s(x, t)] = \delta(\tau - t_0 + qx_0^2), \quad (4.45)$$

and similar arguments as with the linear gives that the Fourier spectrum is limited by the lines

$$\mathcal{L}_1 : \omega_q = \omega_{\tau} x_{\max}^2 \quad \text{and} \quad \mathcal{L}_2 : \omega_q = \omega_{\tau} x_{\min}^2. \quad (4.46)$$

Two seismic events at depths  $z = 1$  km and  $z = 2$  km in a medium of constant velocity  $c = 1$  km/s are modelled by hyperbolas, Figure 4.14(a). The sampling grid are defined by  $0 \leq t \leq 4$  s with  $\Delta t = 0.02$  s and  $0 \leq x \leq 2.5$  km with  $\Delta x = c\Delta t = 0.04$  km. The Parabolic Radon transform is given in Figure 4.14(b), the aperture is limited by the sampling in offset, and the bandwidth is given by the lines

$$\mathcal{L}_1 : \omega_q = 6.25\omega_{\tau} \quad \text{and} \quad \mathcal{L}_2 : \omega_q = 0.$$

The Fourier spectrum of the Radon transform is shown in Figure 4.15, the lines  $\mathcal{L}_1$  and  $\mathcal{L}_2$  are plotted in red. This shows that a different choice of periodicity would sample the parabolic Radon domain more efficiently.

### 4.5.3 Comments

To summarize, the Radon transform used in CT scans, have finite bandwidth. This is also the case for the (geophysical) discrete linear and parabolic Radon transform. Therefore, a multirate sampling scheme would be preferable and possibly make the transformation more efficient.

In these examples the least squares solution of both the linear and parabolic radon transform is used, (Beylkin, 1987; Yilmaz and Doherty, 2001). However, when using a diamond sampling scheme as in Section 3.3.2, the Fourier transformation is no longer separable in space and the transform in one direction is aliased. This imposes a problem when calculating the transform,

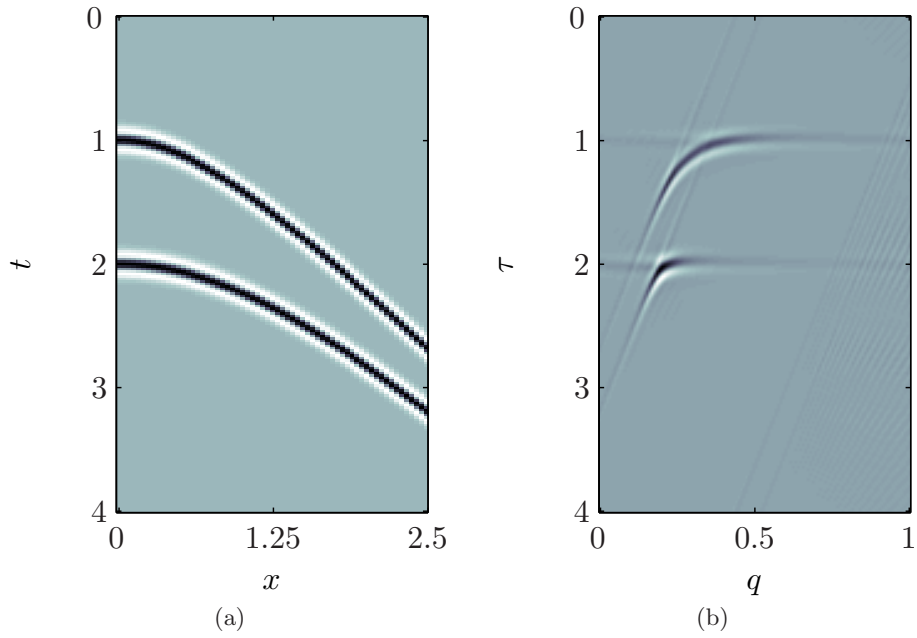


Figure 4.14: (a) Two hyperbolic events at depths  $z = 1$  km and  $z = 2$  km with velocity  $c = 1$  km/s and (b) the Parabolic Radon transform.

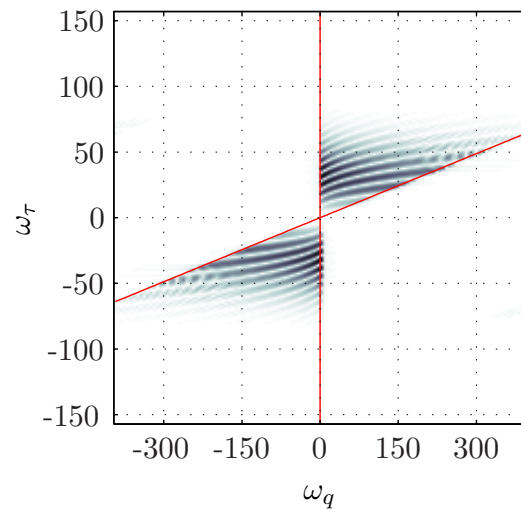


Figure 4.15: The Fourier transform of Figure 4.14(b).

since the majority of transform algorithms are evaluated in frequency-offset. The hexagonal Fourier transform with rectangular output could be a candidate for this. This transform does give a frequency-offset domain. There have been developed fast methods for calculating the transform in time-offset domain, (Yilmaz and Taner, 1994), which also could make it possible to calculate on other lattices than the rectangular.

## Chapter 5

# Seismic Migration

Seismic migration is the process of finding the wavefield  $p = p(x, y, z, t = 0)$  where  $z$  is the depth from a wavefield recorded in time  $p = p(x, y, z = 0, t)$ . It is often assumed that instead of the waves traveling down to the reflectors and back, the reflectors is a collection of seismic sources which explode at time zero. This is called an exploding reflector model and makes the migration algorithms simpler to deduce and implement.

Seismic recordings can be expressed as

$$p(x, y, z = 0, t) = \mathcal{L}[p(x, y, z, t = 0)] \quad (5.1)$$

where  $\mathcal{L}$  is the earths response to seismic waves. Seismic migration is the inverse of this

$$p(x, y, z, t = 0) = \mathcal{L}^{-1}[p(x, y, z = 0, t)], \quad (5.2)$$

where the operator  $\mathcal{L}$  is generally governed by the wave equation. All migration algorithms are approximate solutions to this inversion.

The first section in this chapter is a study of Gazdag phase-shift algorithm implemented with multirate sampling, and then a study of Reverse Time Migration (RTM).

General references on the subject of seismic migration is Stolt and Benson (1986) and Yilmaz and Doherty (2001)

### 5.1 Seismic Migration by Extrapolation

The 2D acoustic wave equation is given as

$$\frac{\partial^2 p}{\partial t^2} = c^2 \left( \frac{\partial^2 p}{\partial x^2} + \frac{\partial^2 p}{\partial z^2} \right) \quad (5.3)$$

where  $p = p(x, z, t)$ . If the velocity is only dependent on depth,  $c = c(z)$ , it is possible to Fourier transform the equation in  $t$  and  $x$ . By defining  $Q = Q(k_x, z, \omega)$ , the equation becomes

$$\frac{\partial^2 Q}{\partial z^2} + \left[ \left( \frac{\omega}{c} \right)^2 - k_x^2 \right] Q = 0, \quad (5.4)$$

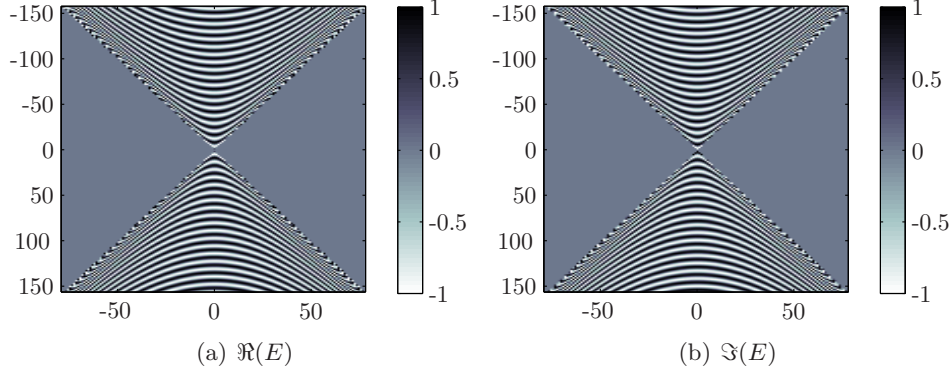


Figure 5.1: The real and complex part of the extrapolation filter  $E$

which has the solution

$$Q = Ue^{izk_z} + De^{-izk_z}, \quad (5.5)$$

when  $k_z = \sqrt{(\frac{\omega}{c})^2 - k_x^2}$ . Here  $U(k_x, z, \omega)$  and  $D(k_x, z, \omega)$  is the upwards and downwards propagating wavefield. If the wavefield is known in a position  $z_0$ , the upward propagating wavefield in a position  $z \leq z_0$  is given by

$$U(k_x, z, \omega) = U(k_x, z_0, \omega)e^{i(z-z_0)k_z} \quad (5.6)$$

and the downward propagating waves in position  $z \geq z_0$

$$D(k_x, z, \omega) = D(k_x, z_0, \omega)e^{-i(z-z_0)k_z}. \quad (5.7)$$

This shows that if  $\Delta z = |z - z_0|$ , the wavefield in a position  $z_0 \pm \Delta z$  can be expressed

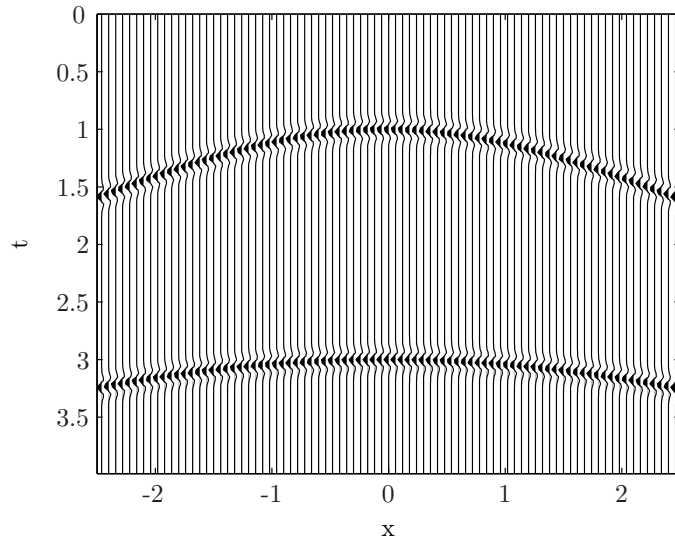
$$Q(k_x, z \pm \Delta z, \omega) = Q(k_x, z_0, \omega)e^{-i\Delta z k_z}. \quad (5.8)$$

The operator  $E = e^{-i\Delta z k_z}$  is called the extrapolation operator. Considering only propagating waves,  $|\omega/c| \geq |k_x|$ , this is an all-pass filter with phase shift (Gazdag, 1978). The filters real and imaginary part is shown in Figure 5.1.

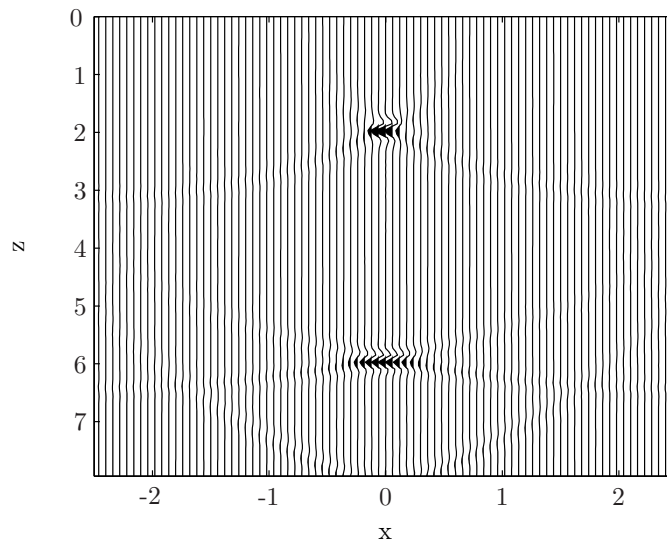
Seismic migration is generally a combination of extrapolation and imaging. The approach is first to Fourier transform the data from  $(x, t)$  to  $(k_x, \omega)$ , multiply with the extrapolation operator  $E$ , and an inverse Fourier transform. This is done for each extrapolation step,  $n$ , and the data at zero time corresponds to the wavefield at depth  $n\Delta z$ . Extracting at  $t = 0$  for each extrapolation step until the desired depth is reached, results in the migrated image. This algorithm is often called Gazdag phase-shift migration, and only allows for velocity as a function of depth,  $c = c(z)$ . This because the Fourier transform from  $(x, t)$  to  $(k_x, \omega)$  require constant velocity.

An example of a migration of two events at depths  $z = 2$  km and  $z = 6$  km in a medium with constant velocity  $c = 2$  km/s, approximated by hyperbolas is shown in Figure 5.2. The





(a) Model



(b) Migrated image

Figure 5.2: (a) Model with two exploding sources at depths  $z = 2$  km and  $z = 6$  km , (b) the migrated image.

sampling grid is given by  $\Delta t = 0.03$  s,  $\Delta x = c\Delta t$ , the period  $T = 4$  s and the offset is sampled from  $-2.5$  km to  $2.5$  km. This grid has  $N_t \times N_x = 134 \times 84 = 11,256$  sampling points.

The extrapolation operator has bandwidth with the same geometry as the optimal sampling from Section 4.2, when only considering propagating waves, not the evanescent field, Figure 5.1. Therefore choosing a diamond periodicity will be most efficient. The periodicity matrix in Fourier domain is given

$$\mathbf{A}^T = \frac{1}{2} \begin{pmatrix} N_x & -N_x \\ N_t & N_t \end{pmatrix} = \begin{pmatrix} 42 & -42 \\ 67 & 67 \end{pmatrix}, \quad (5.9)$$

and the number of sampling points  $\det(\mathbf{A}) = 5,628$ , which is exactly half the number of sampling points compared to conventional sampling. Defining the imaging lattice,  $(x, z)$ , with the same matrix will make it possible to extrapolate downwards in depth and image at time  $t = 0$  for each  $\Delta z$ . The sampling points on the lattice for imaging is integer with diamond sampling, as shown in Section 3.3.2.

In this example the Smith Normal Form is

$$\mathbf{D} = \begin{pmatrix} 1 & 0 \\ 0 & 5628 \end{pmatrix} \quad (5.10)$$

which shows that it is sufficient with 1D FFTs for each extrapolation step. The first step is to resample the model from Figure 5.2(a) to the new lattice, this is plotted in Figure 5.3(a). The result of migration on this lattice is shown in Figure 5.3(b). The migration is done by mapping the extrapolation filter and the seismic section to the diagonal space and extrapolating there. In this figure the traces are plotted over the multirate sampling points, which can be seen at the top and bottom of the figures where every second trace start at later or earlier sample.

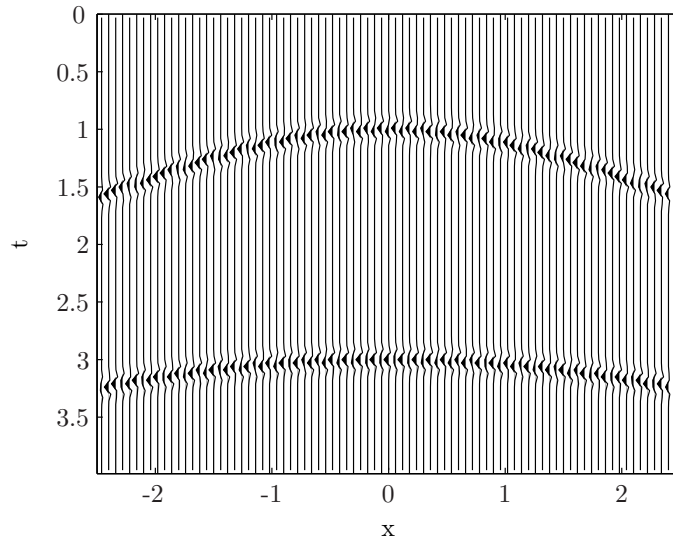
The diamond sampling scheme introduce a different periodicity in Fourier domain than rectangular sampling. Fourier domain of the conventional sampled migration is plotted in Figure 5.4(a). A periodic expansion of Fourier domain of the multirate sampled migration is shown in Figure 5.4(b). The plot shows four periods, as indicated by the red parallelograms. The blue lines show the conventional sampling period, and the multirate sampling scheme contains only half the data. The periodic expansion shows that the Fourier spectrum of the multirate sampled migration is almost the same as with rectangular periodicity, except for some small differences due to migration artifacts and alias.

The wavelets in Figure 5.3(b) look different compared to Figure 5.2 this is because there are much less sampling points. This can be corrected for with interpolation back to the original grid after the migration.

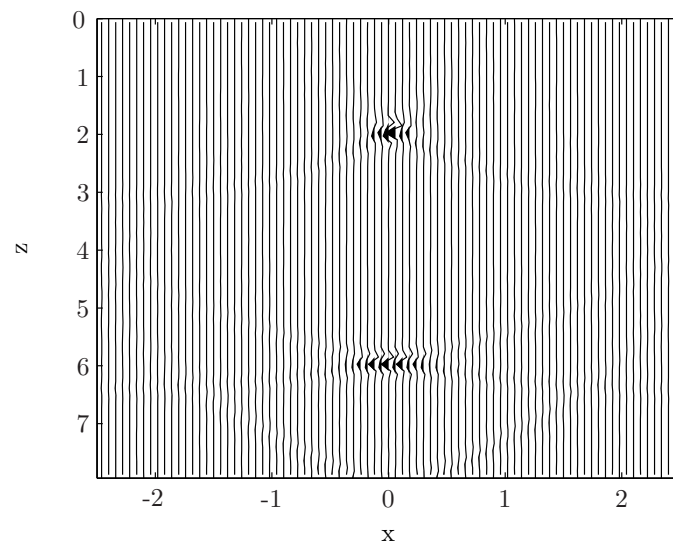
### 5.1.1 3D Seismic Migration

The extrapolation operator  $E = e^{-i\Delta z k_z}$  can be used for seismic migration of 3D data. In 3D the dispersion relation gives that

$$k_z = \sqrt{\left(\frac{\omega}{c}\right)^2 - k_x^2 - k_y^2}, \quad (5.11)$$

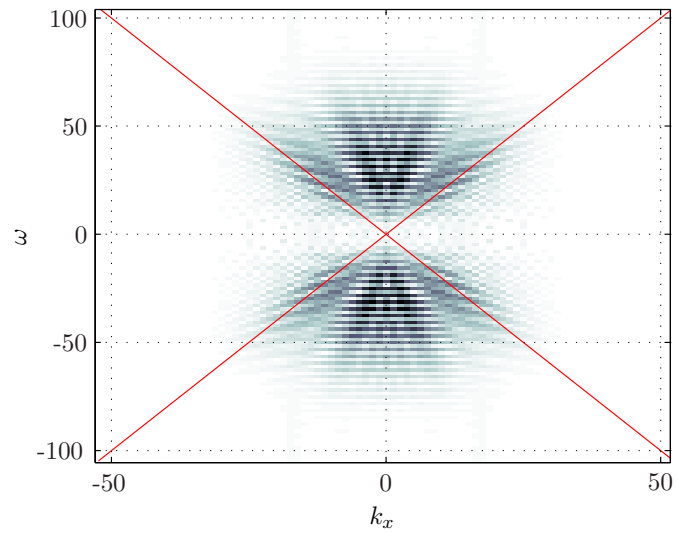


(a) Model

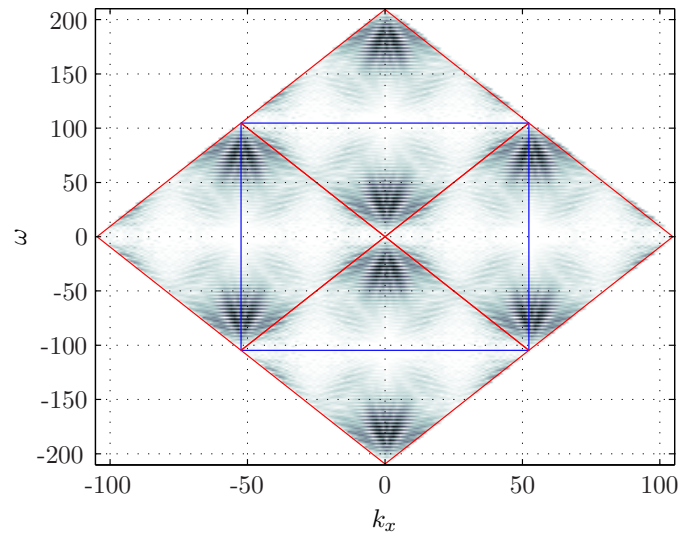


(b) Migrated image

Figure 5.3: (a) Multirate sampling and migration of a model with two exploding sources at depths  $z = 2$  and  $z = 6$ , (b) the migrated image



(a) Rectangular grid



(b) Multirate grid

Figure 5.4: (a) The Fourier transformation of a migrated image on a conventional grid, (b) Fourier transformation and periodic extension of a diamond sampled migration, red lines are the sampling period and blue indicate the conventional sampling period.

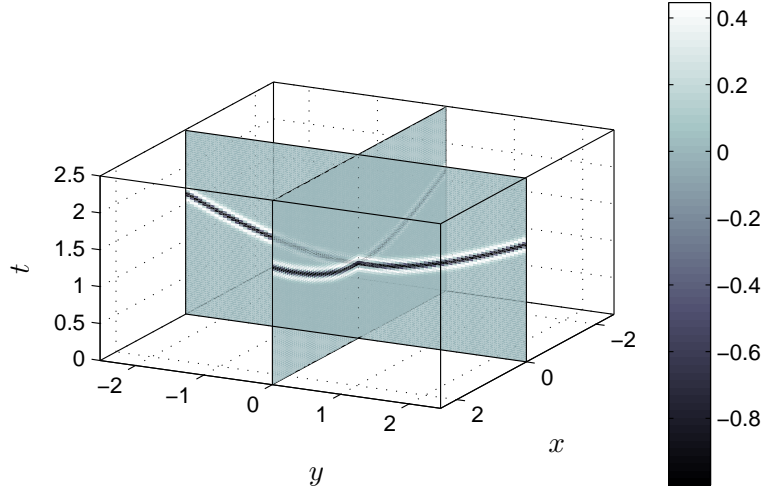


Figure 5.5: A seismic recording of a single source at depth  $z = 2$  km in a medium with constant velocity  $c = 2$  km/s

generates the filter  $E$ . A seismic source at depth  $z = 2$  km in a medium with velocity  $c = 2$  km/s is modeled with a hyperboloid, Figure 5.5. The model is sampled with  $\Delta t = 0.03$  s,  $\Delta x = \Delta z = c\Delta t$  which is optimal for rectangular sampling, the number of sampling points is  $N_t N_x N_y$ . Choosing a periodicity matrix as in Section 4.2,

$$\mathbf{A}^T = \begin{pmatrix} N_x/2 & -N_x/2 & 0 \\ 0 & 0 & N_y \\ N_t/2 & N_t/2 & 0 \end{pmatrix}, \quad (5.12)$$

results in half the sampling points.

The 3D Fourier spectrum of the seismic section sampled with this geometry is plotted in Figure 5.6, the spectrum is overlaid a double cone with velocity  $c = 3$  km/s. On the line through  $k_y = 0$  the periodicity given by  $\mathcal{R}(\mathbf{A})$  is observed by the dotted lines.

A 3D Gazdag phase-shift migration is then calculated on this lattice, the filter have the same bandwidth as the data, and the result is shown in Figure 5.7. The algorithm is a straight forward expansion of the one for 2D.

## Comments

The Gazdag phase-shift migration can be calculated for both 2D and 3D data sets on non-rectangular sampling grids. The results are the same as with the conventional sampling except for some differences in migration artifacts. The aliasing pattern of migration with a smaller periodicity becomes different, therefore it could become more difficult to interpret these problems. Both 2D and 3D migrations are performed on sampling grids with only half the sampling points compared to conventional rectangular sampling.

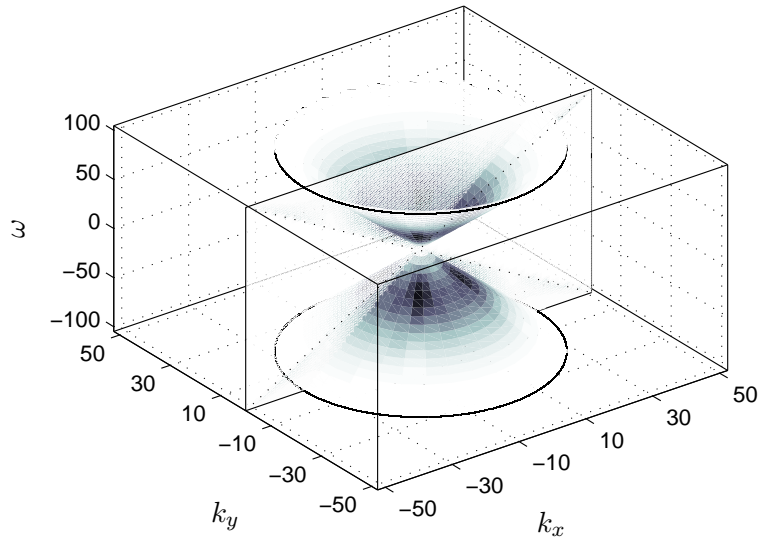


Figure 5.6: Fourier transform of the seismic recording in Figure 5.5 after downsampling to the multirate grid

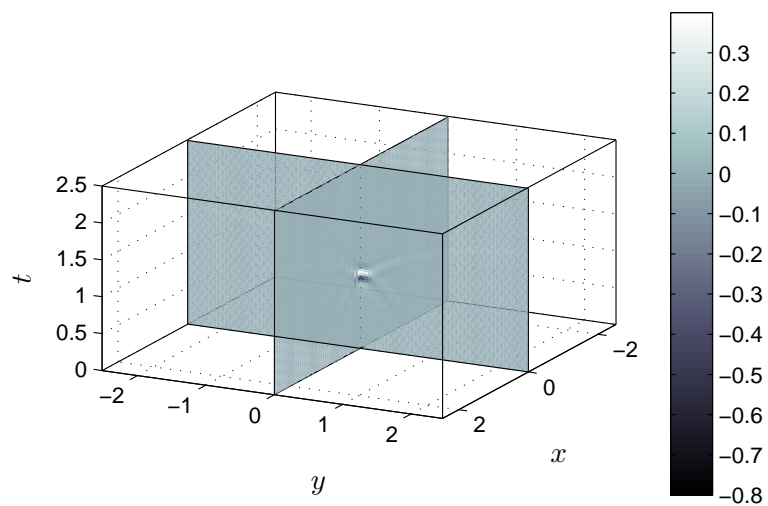


Figure 5.7: Gazdag phase-shift migration of the model in Figure 5.5

## 5.2 Reverse Time Migration

Reverse Time Migration (RTM) is based on solving the wave equation as a boundary value problem. It was introduced in the 1980s by McMechan (1982, 1983); Loewenthal and Mufti (1983); Baysal et al. (1983). This algorithm allows for a rapidly varying velocity field in all space coordinates. It is constructed for 2D post-stack data with the exploding reflector assumption, but there has also been developed methods for 3D pre-stack data (Chang and McMechan, 1990).

Let  $p(x, z = 0, t)$  be the recorded wavefield at the surface, where  $x$  is the horizontal offset and  $z$  is depth increasing downwards. As before the migrated section should then be  $p(x, z, t = 0)$ . Assuming that all energy has propagated away from the subsurface after the last time sample  $T_N$ ,  $p(x, z, t) = 0 \forall t > T_N$ . Migration is performed by extrapolating the section backwards in time until time  $t = 0$ , which is the imaging condition. The problem is then formulated as a boundary value problem with  $p(x, z = 0, t)$  as boundary condition. McMechan (1983) called this *boundary value migration* (BVM), but the most common term is that of Baysal et al. (1983) namely *reverse time migration* (RTM).

McMechan (1983) constructs the algorithm by using a finite difference scheme for the derivatives. The algorithm presented here is based on Fourier derivatives, (Gazdag, 1980), for the spatial coordinates, (Baysal et al., 1983). The advantage of using Fourier derivatives is that it does not introduce numerical dispersion as any finite difference scheme.

The dispersion relation for downwards traveling waves is

$$\omega = c(k_z^2 + k_x^2)^{1/2}, \quad (5.13)$$

where  $(k_x, k_z)$  are horizontal and vertical wavenumbers, and  $\omega$  the angular frequency. If the velocity  $c$  is constant, the wave equation can be written

$$\frac{\partial P}{\partial t} = ick_z \left(1 + \frac{k_x^2}{k_z^2}\right)^{1/2} P, \quad (5.14)$$

(Gazdag, 1981). Here  $P = P(k_x, k_z, t)$  is the two dimensional Fourier transform of  $p = p(x, z, t)$ . To allow for velocity variations, this equation can be written

$$\frac{\partial p}{\partial t} = c \mathcal{F}^{-1} \left[ ik_z \left(1 + \frac{k_x^2}{k_z^2}\right)^{1/2} \mathcal{F}[p] \right], \quad (5.15)$$

where  $\mathcal{F}$  is the Fourier transform over the space coordinates  $(x, z)$ . Gazdag (1981) shows that the step from equation (5.14) to (5.15) allows the velocity to become a function of the space coordinates,  $c = c(x, z)$ . The equation can also be written

$$\frac{\partial p}{\partial t} = c \mathcal{F}^{-1} \left[ \text{sign}(k_z) i (k_z^2 + k_x^2)^{1/2} \mathcal{F}[p] \right] \quad (5.16)$$

which does not have a singularity at  $k_z = 0$ . This equation gives a numerical estimate of the time derivative of the wavefield at time  $t = T_{N-n}$  for  $n \in \mathbb{Z}_N$ . The approach is first to

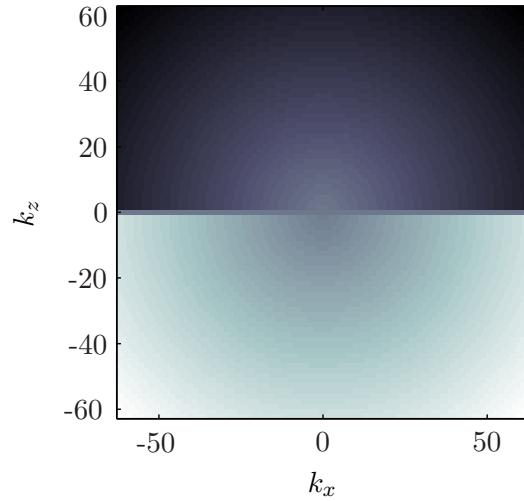


Figure 5.8: The differentiation filter  $\mathcal{D}(k_x, k_z)$

Fourier transform over  $(x, z)$ , multiply with the filter  $\mathcal{D} = \text{sign}(k_z)i(k_z^2 + k_x^2)^{1/2}$ , an inverse Fourier transform, followed by multiplication by the velocity field. The differentiation filter  $\mathcal{D}$  is plotted in Figure 5.8.

The time derivative can be approximated by a centered finite difference around time  $T_{N-n}$ . Defining  $p(x, z, T_{N-n}) = p_{N-n}$  yields,

$$\frac{\partial p_{N-n}}{\partial t} = \frac{p_{N-n+1} - p_{N-n-1}}{2\Delta t} \quad (5.17)$$

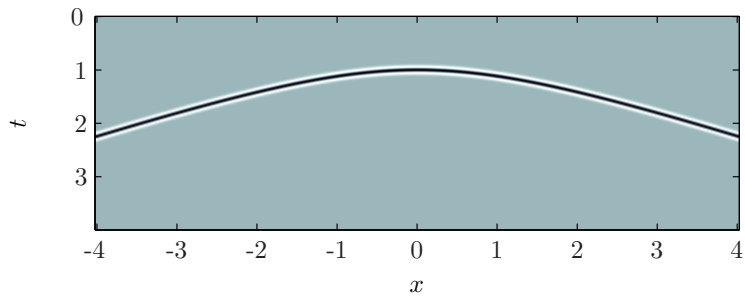
where  $\Delta t$  is the sampling interval in time, and  $T_{N-n} = T_N - n\Delta t$ . The RTM is based on extrapolating the wavefield backwards in time, combining equations (5.16) and (5.17) gives

$$p_{N-n-1} = p_{N-n+1} - 2c\Delta t \mathcal{F}^{-1}[\text{sign}(k_z)i(k_z^2 + k_x^2)^{1/2} \mathcal{F}[p_{N-n}]]. \quad (5.18)$$

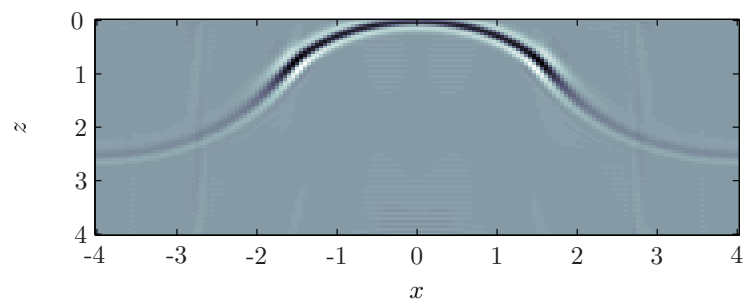
The values of  $p(x, z = 0, T_{N-n})$  are provided from the recorded data at each time step. Starting at  $n = 0$  and calculating until  $n = N - 1$ , results in the final migrated image,  $p(x, z, t = 0)$ . There are many improvements of this algorithm, for example it can be expanded to TTI anisotropic waves, (Du et al., 2007).

Figure 5.9(a) shows a seismic recording of a single source at depth  $z = 2$  km in a homogeneous medium with velocity  $c = 2$  km/s. The sampling parameters is  $\Delta t = 0.005$  s,  $\Delta x = \Delta z = 0.05$  km, the sampling period is  $T = 4$  s, total offset  $L_x = 8$  km and maximum depth  $L_z = 4$  km. This sampling scheme results in  $N = T/\Delta t = 800$  extrapolation steps. Figure 5.9(b) and 5.9(c) shows the wavefield at time  $t = 1$  and  $t = 0.5$  s. This shows that the algorithm focuses the wave front at the source, which is in the final migrated image at time  $t = 0$  s, Figure 5.9(d).

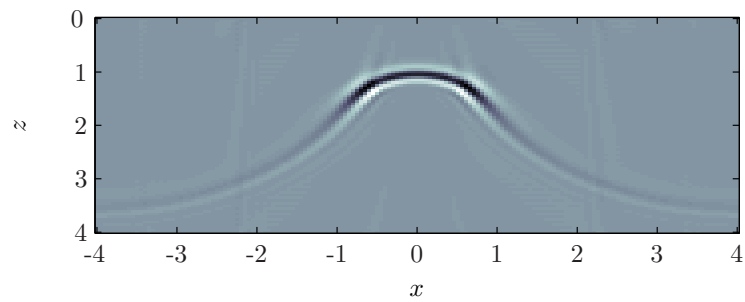




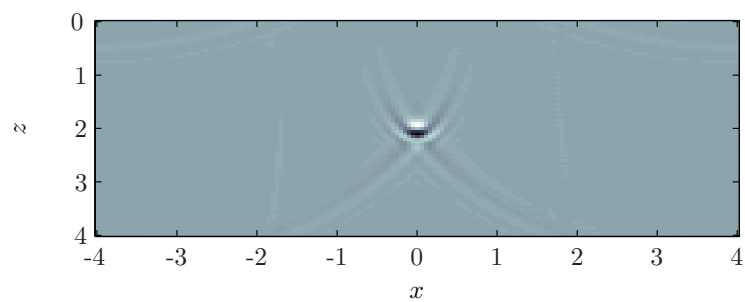
(a) A seismic section from a source at depth  $z = 2\text{km}$



(b) The wavefield at time  $t = 1$  sec



(c) The wavefield at time  $t = 0.5$  sec



(d) The wavefield at time  $t = 0$  sec

Figure 5.9: Time steps in Reverse Time Migration

### 5.2.1 Stability of the RTM

When approximating derivatives with finite difference it is important to study the stability of the operator.

Assuming constant velocity  $c$ , and the wavefield in Fourier domain  $P = P(k_x, k_z, t)$ , equation (5.16) can be written

$$\frac{\partial P}{\partial t} = ic|\mathbf{k}|P \quad (5.19)$$

where  $|\mathbf{k}| = \sqrt{k_x^2 + k_z^2}$ . For a medium with a variable velocity,  $c$  should be chosen  $c = c_{\max}$ . Equation (5.17) results in

$$P_{N-(n+1)} - P_{N-(n-1)} = 2ic\Delta t|\mathbf{k}|P_{N-n}, \quad (5.20)$$

letting  $a = c\Delta t|\mathbf{k}|$  gives the second-order difference equation

$$P_{N-n+1} - 2iaP_{N-n} - P_{N-n-1} = 0. \quad (5.21)$$

This type of difference equations has general solution

$$P_n = A\lambda_1^n + B\lambda_2^n, \quad \lambda \in \mathbb{C}, \quad (5.22)$$

where  $A$  and  $B$  are constants. The system is stable only when  $|\lambda_{1,2}| \leq 1$ . The characteristic polynomial is given

$$\lambda^2 - 2ia\lambda - 1 = 0, \quad (5.23)$$

hence two solutions

$$\lambda_{1,2} = ia \pm \sqrt{1 - a^2} = i[a \pm \sqrt{a^2 - 1}]. \quad (5.24)$$

There are two possibilities for  $a$ , either  $|a| \leq 1$  or  $|a| > 1$ . The first case can be investigated by letting  $a = \cos \phi$ , which is always smaller than, or equal to 1. Then the solution to the characteristic polynomial becomes

$$\lambda_{1,2} = i[\cos \phi \pm i \sin \phi] = ie^{\pm i\phi}, \quad (5.25)$$

hence

$$|\lambda_{1,2}|^2 = 1, \quad (5.26)$$

and both solutions are on the unit circle in the complex plane. The solution to the difference equation when  $|a| \leq 1$  is

$$P_n = iAe^{\pm i\phi n}, \quad (5.27)$$

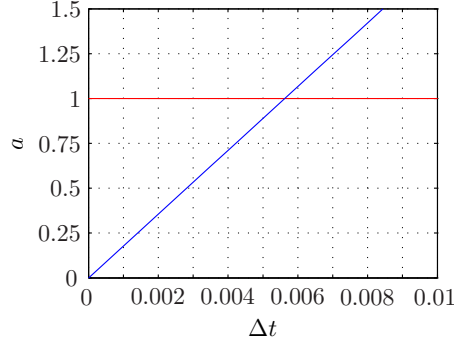


Figure 5.10: Time step against stability factor for fixed sampling in space, red line indicate  $a = 1$

which is stable when  $n \rightarrow \infty$ .

The other possibility is that  $a > 1$ , the solution

$$\lambda_{1,2} = i[a \pm \sqrt{a^2 - 1}], \quad (5.28)$$

gives that one  $\lambda$  is outside and one inside the unit circle in the complex plane, the algorithm is unstable.

If the velocity is a function of space, the maximum is chosen  $c = c_{\max}$ , and the stability condition for RTM is

$$a = c_{\max} \Delta t |\mathbf{k}| \leq 1. \quad (5.29)$$

On a finite rectangular sampling grid the maximum of  $k_x$  and  $k_z$  are the Nyquist wavenumbers  $k_{xNy} = \frac{\pi}{\Delta x}$  and  $k_{zNy} = \frac{\pi}{\Delta z}$ , therefore

$$a = c_{\max} \Delta t \sqrt{k_{xNy}^2 + k_{zNy}^2} = c_{\max} \Delta t \sqrt{\left(\frac{\pi}{\Delta x}\right)^2 + \left(\frac{\pi}{\Delta z}\right)^2} \leq 1. \quad (5.30)$$

This equation shows that the  $(x, z)$  grid should be chosen as coarse as possible without introducing alias because it lets the time step  $\Delta t$  be larger. The time step generally becomes quite small, the example in Figure 5.9(a) have  $\Delta x = \Delta z = 0.05$  km, which gives

$$a = \sqrt{2} c_{\max} \Delta t \frac{\pi}{\Delta x} \quad (5.31)$$

and with  $c_{\max} = 2$  km/s and  $\Delta t = 0.005$  s the stability factor is

$$a \approx 0.8886 \leq 1, \quad (5.32)$$

and the algorithm is stable. By fixing the sampling interval in  $(x, z)$  and using the maximum velocity, the factor  $a$  can be plotted against the time step. Figure 5.10 shows that the time

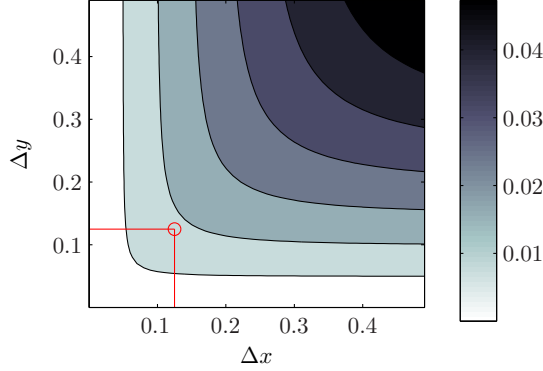


Figure 5.11: The time sampling interval  $\Delta t$  when  $a = 1$  and  $c = 2$

step could be chosen larger,  $\Delta t = 0.0056$  s, this would decrease the number of steps until time  $t = 0$  and therefore make the algorithm finish faster.

The optimal sampling discussed in Section 4.2 will not work in this case. If the sampling grid is chosen such that  $\Delta x = \Delta z = c_{\min}\Delta t$ , the stability condition will not be fulfilled because

$$a = c_{\max}\sqrt{2}\frac{\Delta t\pi}{c_{\min}\Delta t} = \sqrt{2}\pi\frac{c_{\max}}{c_{\min}} \geq 1, \quad (5.33)$$

since  $\frac{c_{\max}}{c_{\min}} \geq 1$ . The extreme limit for a stable migration is when  $a = 1$ , by fixing the migration grid  $\Delta x, \Delta z$ , the maximum  $\Delta t$  can be expressed by

$$\Delta t = \frac{1}{c_{\max}\sqrt{k_{xNy}^2 + k_{zNy}^2}}. \quad (5.34)$$

For a maximum velocity  $c_{\max} = 2$  km/s and  $\Delta x, \Delta z$  both ranging from 0 to 0.5 km/s,  $\Delta t$  is shown in Figure 5.11. Choosing a grid for the migration defined by  $\Delta x = \Delta z = 0.1250$  km, the necessary time step is plotted by the red lines and circle. The maximum time step for these parameters are given by equation (5.34),  $\Delta t = 0.014$  s.

A seismic recording of a single source at depth  $z = 2$  km, sampled with this configuration modeled by a hyperbola is shown in Figure 5.12(a). This is low pass filtered with a Blackman window with a cutoff  $\omega = c_{\min}k_{xNy}$  to avoid alias. Figure 5.12(b) shows the absolute value of Fourier domain of this seismic section. It is oversampled due to the stability criteria. In Figure 5.12(c) the result of the migration is plotted. The absolute value of the Fourier transform of the migrated image is shown in Figure 5.12(d), as expected it has circular bandwidth.

In Figure 5.12(c) the wavelets phase has changed compared to the recording where it is zero phase. This is because the modeling with hyperbola is most suitable for 3D seismic, the wavelet gets a phase change of  $\pi/4$ . This can be corrected by filtering the migrated image with the all pass filter  $e^{i\pi/4}$ .

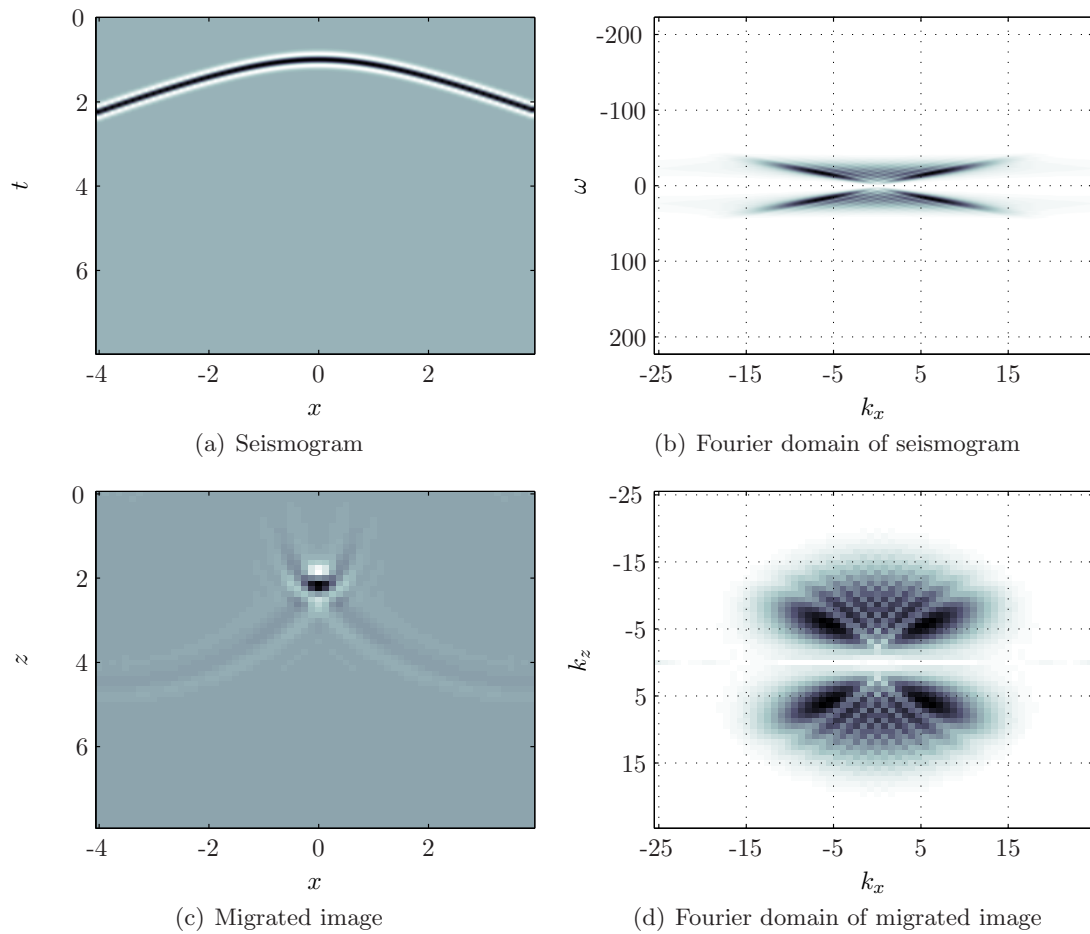


Figure 5.12: (a) A seismic section modeled by a hyperbola from a single exploding source at depth  $z = 2$  km in a medium with constant velocity  $c = 2$  km/s. (b) the Fourier transform of (a), (c) migrated image and (d) the Fourier transform of the migrated image

## 5.2.2 Hexagonal Sampling

The band region of migrated images are circular, see Figure 5.12(d), therefore assuming hexagonal periodicity is preferable for RTM. Assuming that the seismic is sampled with equal number of samples for both  $x$  and  $z$ , the matrix from Section 3.2.2 can be used,

$$\mathbf{H}^T = \begin{pmatrix} N & 0 \\ 3M & 2(N+M) \end{pmatrix} = \begin{pmatrix} N & 0 \\ 3N/2 & 3N \end{pmatrix}, \quad (5.35)$$

where  $N = N_x/2 = N_z/2$ ,  $M = N_x/4$ , for a even number of samples.

The lattice for imaging is then given by

$$\mathbf{x} = \mathbf{T}\mathbf{H}^{-1}\mathbf{n}, \quad (5.36)$$

where  $\mathbf{n} \in \mathcal{R}(\mathbf{H})$ ,  $\mathbf{x} = (x, z)^T$  and  $\mathbf{T}$  is the rectangular period,

$$\mathbf{T} = \begin{pmatrix} X & 0 \\ 0 & Z \end{pmatrix}, \quad (5.37)$$

when  $X$  is maximum offset and  $Z$  maximum depth. The lattice could also be given on the integer interval from zero to the number of samples in both directions by choosing

$$\mathbf{T}_N = \begin{pmatrix} N_x & 0 \\ 0 & N_z \end{pmatrix}, \quad (5.38)$$

which makes the computer calculations simpler. These points is denoted by  $\boldsymbol{\eta} \in \mathcal{R}(\mathbf{T}_N)$ . The lattice is generated by the sampling matrix

$$\mathbf{V} = \mathbf{T}_N\mathbf{H}^{-1} = \begin{pmatrix} 2 & -3/4 \\ 0 & 1 \end{pmatrix}, \quad (5.39)$$

and from Section 2.5 the sampling points is given,

$$\boldsymbol{\eta} = \mathbf{V}\mathbf{n}, \quad (5.40)$$

where  $\mathbf{n} \in \mathcal{R}(\mathbf{H})$ .

The RTM gets input for each time step at  $z = 0$ , and generally when imaging on a lattice other than the input lattice, interpolation would be necessary. But for the case outlined, the sampling matrix  $\mathbf{V}$  shows that  $\eta_1 = 2n_1$  at  $z = 0$ , which is integer and no interpolation is needed.

If the velocity function is sampled on a rectangular lattice it has to be downsampled. The RTM finite difference scheme, equation (5.18), is only time dependent, and by using Smith normal form, it can be calculated on the grid given by  $\mathcal{R}(\mathbf{D})$ , where

$$\mathbf{D} = \mathbf{P}\mathbf{A}\mathbf{Q}. \quad (5.41)$$

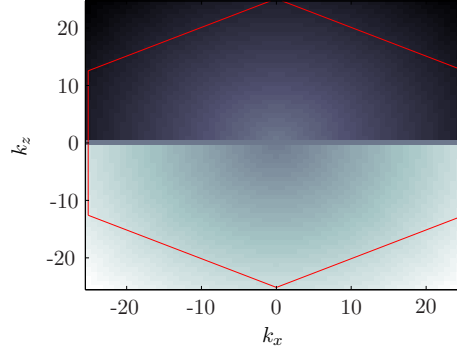
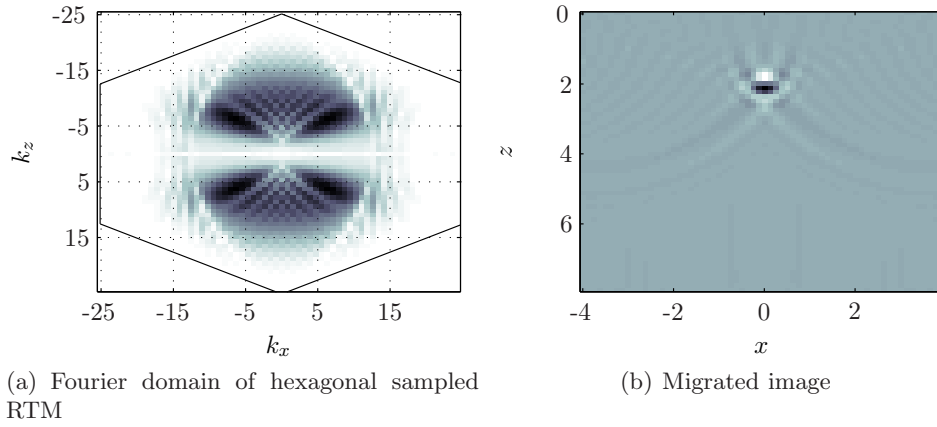


Figure 5.13: Hexagonal sampling of the differentiation filter  $\mathcal{D}$



(a) Fourier domain of hexagonal sampled RTM

(b) Migrated image

Figure 5.14: Hexagonal sampled RTM results

The differentiation filter  $\mathcal{D}$  and the velocity function is mapped with the coordinate transformations  $\Gamma$  from Section 2.4 to the range of the normal form. For each time step, the wavefield at the given time is downsampled to the hexagonal lattice at  $z = 0$ , and mapped to  $\mathcal{R}(\mathbf{D})$ .

The result of the migration is on a hexagonal lattice, for comparison with rectangular migrations it is upsampled with Fourier interpolation. Mapping the sampling points from diagonal space to the hexagonal period in rectangular Fourier domain, an inverse Fourier transform gives the migrated image on a rectangular period. Choosing the same model as Figure 5.12, where  $N_z = N_x = 64$ , the periodicity matrix is

$$\mathbf{H}^T = \begin{pmatrix} 32 & 48 \\ 0 & 96 \end{pmatrix} \quad (5.42)$$

This yields  $\det(\mathbf{H}) = 3N^2 = 3,072$  number of sampling points and compared to the conventional sampling,  $N_x \times N_z = 4,096$ , hexagonal sampling is 25% more efficient. The differentiation filter is sampled within this hexagon, see Figure 5.13, and afterwards mapped to  $\mathcal{R}(\mathbf{D})$ . The finite difference is fully calculated in the range of the diagonal matrix and the resulting Fourier domain is shown in Figure 5.14(a). The upsampled migrated image in Figure 5.14(b) is equal to the migration done on a rectangular period, except for some small oscillations in the upper corners which are due to fewer sampling points.

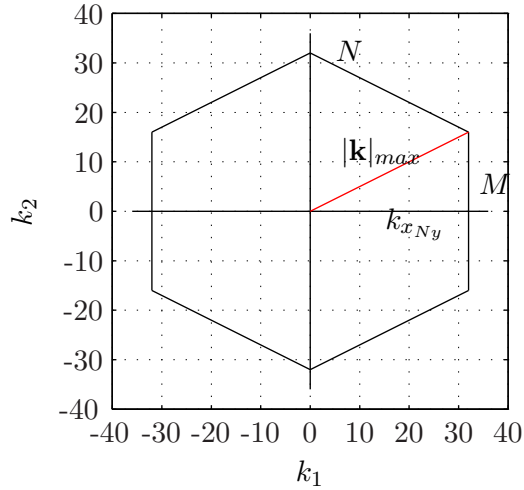


Figure 5.15: The maximum wavenumber (red line) in the hexagonal period

In this example the Smith normal form is

$$\mathbf{D} = \begin{pmatrix} 16 & 0 \\ 0 & 196 \end{pmatrix}, \quad (5.43)$$

which means that a 2D FFT has to be calculated on each step. But for a different choice of the hexagonal periodicity matrix, a diagonal which have first entry equal to 1 could be possible, and a 1D FFT would be sufficient.

Another advantage of calculating the RTM on a hexagonal lattice is that the time step can be increased. The stability condition from equation (5.29) is changed. The maximum wavenumber on a hexagonal period is no longer given by  $|\mathbf{k}| = \sqrt{k_{xNy}^2 + k_{zNy}^2}$ , which is in the upper right corner, since this is not covered by the hexagon. The maximum is dependent on how the period is chosen. In this example the maximum becomes

$$|\mathbf{k}|_{\max} = \sqrt{k_{xNy}^2 + (M\Delta k_z)^2}, \quad (5.44)$$

which can be deduced from Figure 5.15.

Then the maximum time step becomes

$$\Delta t = \frac{1}{c_{\max} \sqrt{k_{xNy}^2 + (M\Delta k_z)^2}} \quad (5.45)$$

and since  $M\Delta k_z \leq k_{zNy}$ , the time step will be larger with hexagonal, than with conventional sampling. Equation (5.45) is valid when  $k_{xNy} = k_{zNy}$ . If these are different, one should do the same analysis again. For the migration in Figure 5.14(b) the time step could be chosen  $\Delta t = 0.0178$  s, which is larger than the maximum time step with conventional sampling,  $\Delta t = 0.0141$  s. Hence with the hexagonal sampling there is need for only  $N_t = 449$  iterations, compared to 571 iteration for conventional sampling.



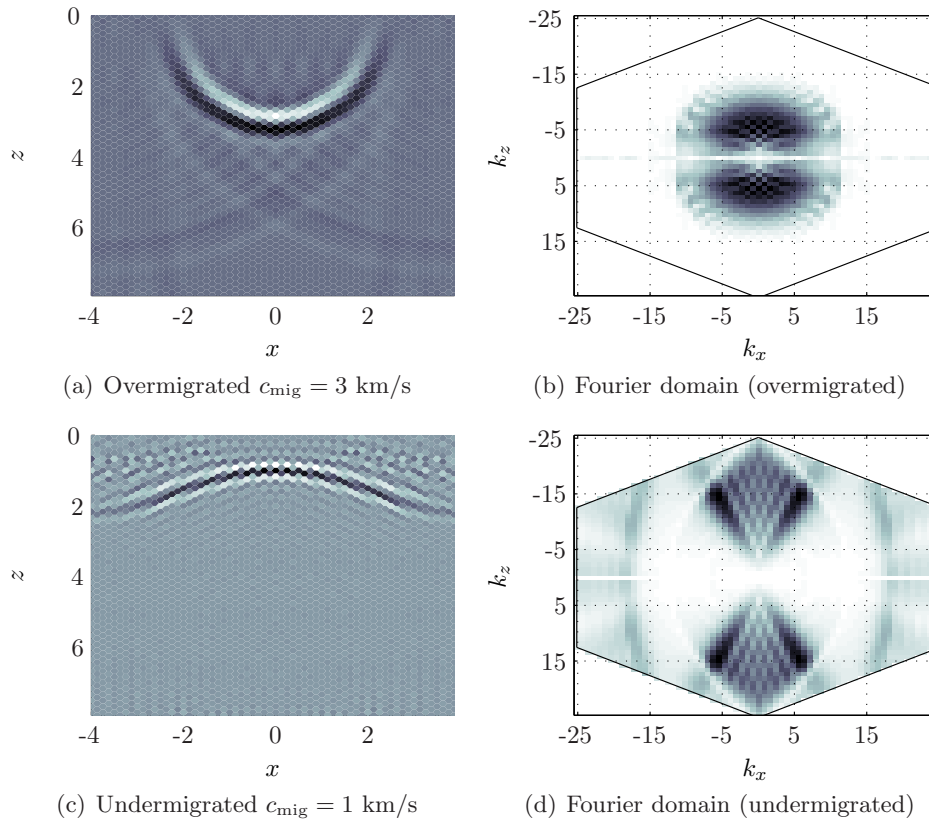


Figure 5.16: Over and under migration with the hexagonal sampled RTM, the seismic sections are plotted by filling the Voronoi diagram.

In Figure 5.16(a) and 5.16(c), there are examples of overmigration ( $c_{\text{mig}} > c$ ), and undermigration, ( $c_{\text{mig}} < c$ ) with this sampling geometry. Overmigration results in a “smile” and undermigration a “frown” in the seismic image. By inspection of Figure 5.16(d), the cone in Fourier domain is still a cone after migration, which shows that the image is not migrated with the correct velocity. In Figure 5.16(b) the overmigration maps the Fourier spectrum to the horizontal axis and may be even further. There is also a phase shift of the wavelet on the overmigrated image, the wavelet changes phase as it moves through the focus.

### 5.2.3 Synthetic Examples

In this section there will be presented a RTM of two synthetic examples, both on rectangular and hexagonal lattices. The first example is data with a varying velocity function. The second is a constant velocity model with many dips present, constructed to illustrate one of RTMs imaging strengths.

#### Kirchhoff Modeled Data

A more realistic example than the single exploding point source is the velocity model given in Figure 5.17(a). Zero offset data modeled with the Kirchhoff integral (Berryhill, 1979) is provided by E. Mæland (Mæland, 1994), Figure 5.17(b). The modeling grid has  $128 \times 128$  sampling points where  $\Delta x = 0.1250$  km and  $\Delta z = 0.0625$  km. The sampling interval in time is  $\Delta t = 0.0080$  s, and the number of samples  $N_t = 1000$ . These sampling parameters yields a stable RTM algorithm. The result of a migration on a rectangular grid is given in Figure 5.18(a). It can be observed that the RTM images steep dips in the data. There are some migration artifacts on the left and right side of the image, this is probably due alias in the operator.

A grid for the finite difference is defined with the matrix from equation (5.35), by  $N = N_x/2$  and  $M = N_x/4$ . This lattice has as previously shown 25% less sampling points. The extrapolation is calculated on a rectangular lattice given by the range of the Smith normal form,

$$\mathbf{D} = \begin{pmatrix} 32 & 0 \\ 0 & 384 \end{pmatrix}. \quad (5.46)$$

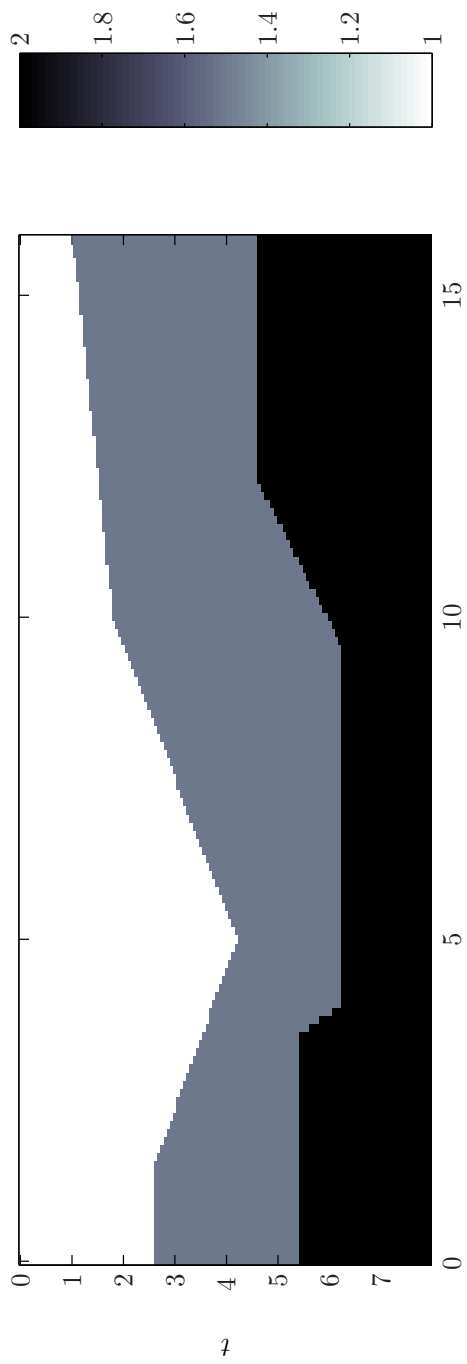
One problem is to downsample the velocity field to the hexagonal lattice given by  $\mathbf{x} = \mathbf{TH}^{-1}\mathbf{n}$  where  $\mathbf{n} \in \mathcal{R}(\mathbf{A})$ . The periodicity is given as  $\mathbf{T} = \text{diag}(X, Z)$ , when  $X$  is maximum offset and  $Z$  maximum imaging depth. The velocity function is downsampled by Fourier transforming and picking the points within the hexagonal period. The real part of the inverse Fourier transform calculated with Smith normal form is the interpolated velocity. The result of the migration on the hexagonal lattice is given in Figure 5.18(b). The result is equal to the one calculated on a rectangular lattice except for some small oscillations.

Both migration results are low-pass filtered with a cutoff frequency  $\omega_c = 40$  rad/s. This removes much of the oscillations and migration artifacts, but for the hexagonal example much of the remaining oscillations could be removed with a lower cutoff.

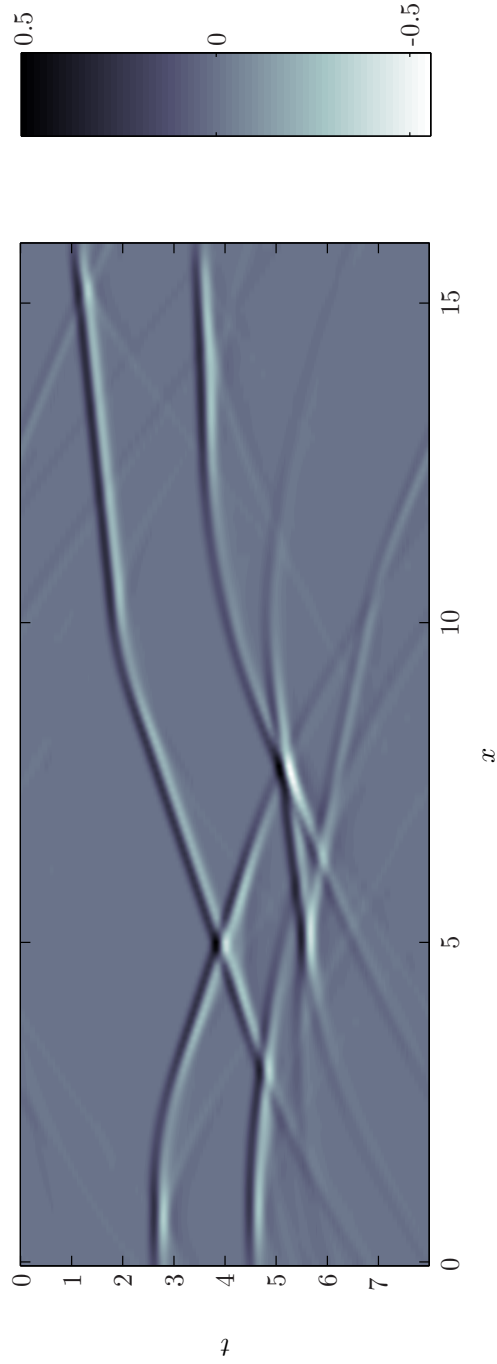
The migration on a rectangular grid runs for approximately 5.2 s, by MATLABs cpu time function, and the hexagonal 4.5 s. This shows that migration on a hexagonal lattice is more efficient with respect to computation time. Figure 5.19(a) and 5.19(b) shows the Fourier spectrum, respectively, of the rectangular sampled and hexagonal sampled migration. These images also resemble each other.

The sampling grid for  $(x, z)$  gives that  $k_{zN_y} > k_{xN_y}$  and the maximal time step for the extrapolation on the hexagonal grid is

$$\Delta t_{\max} = \frac{1}{c_{\max}|\mathbf{k}|_{\max}} = \frac{1}{c_{\max}(k_{zN_y} - \Delta k_z)} \approx 0.01\text{s}. \quad (5.47)$$

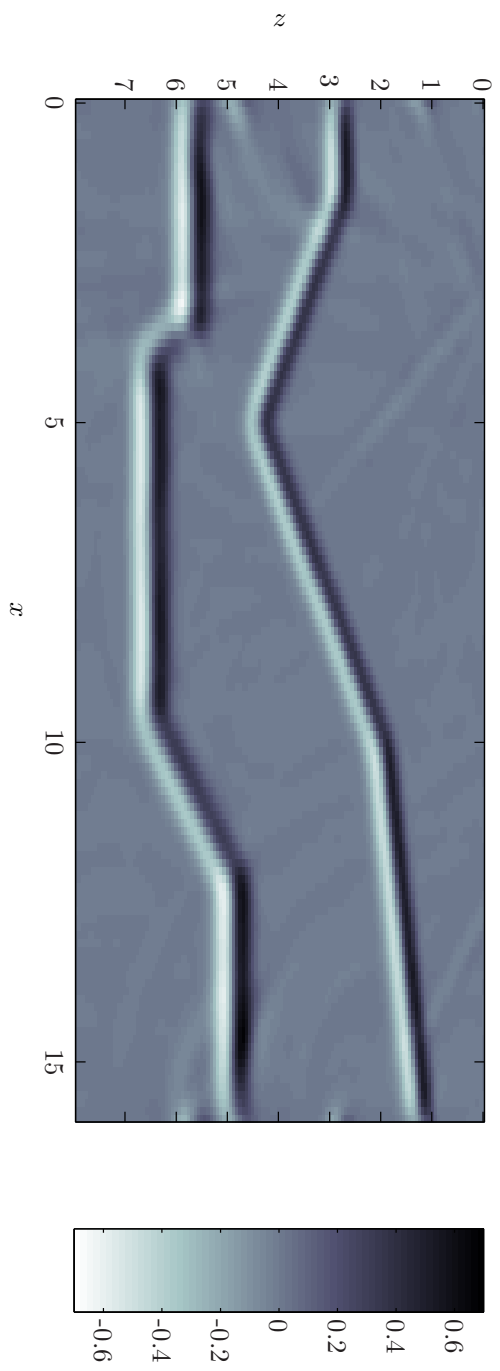


(a) Velocity model

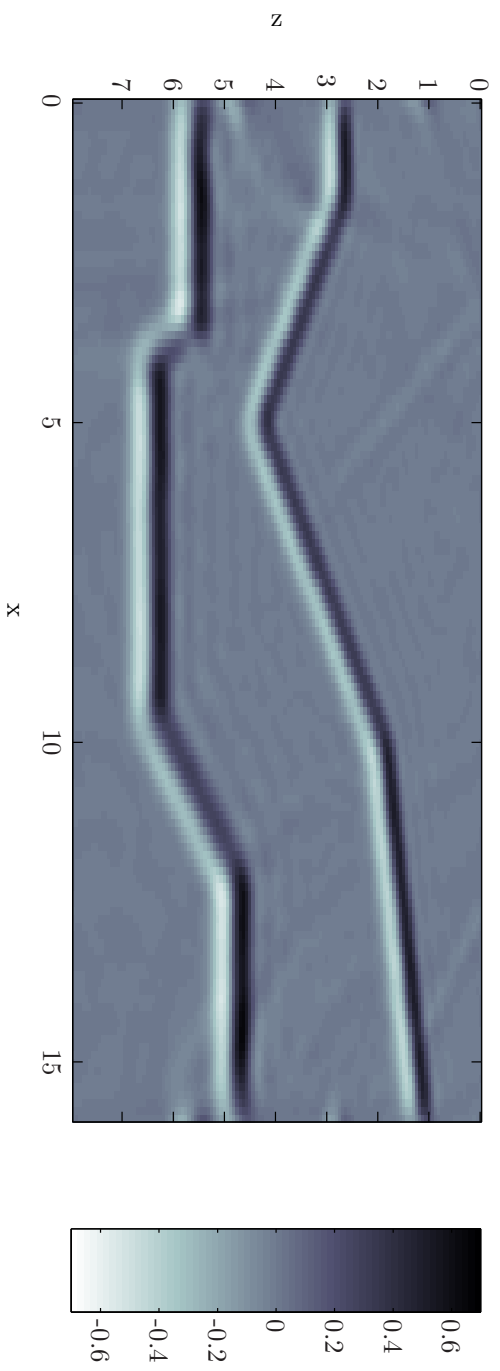


(b) Kirchhoff modeling of exploding reflectors, provided by E. Maeland

Figure 5.17: Model input to the RTM



(a) RTM on a rectangular lattice.



(b) RTM on a hexagonal lattice.

Figure 5.18: Reverse time migration of the model in Figure 5.17.

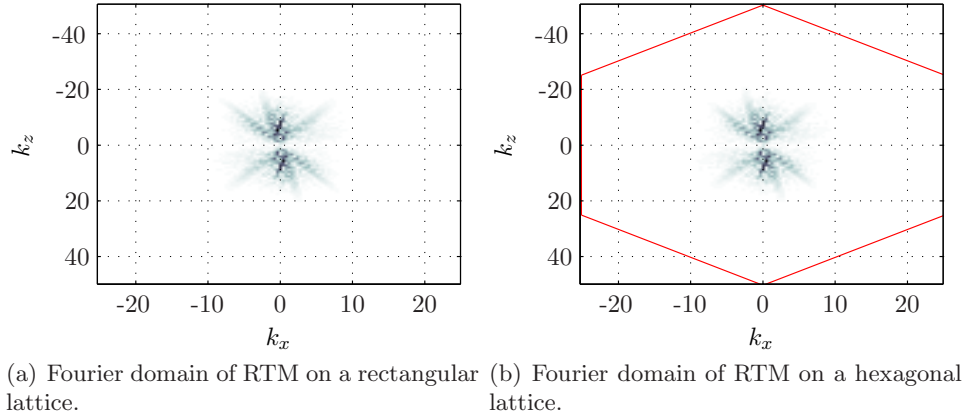


Figure 5.19: Fourier domain of the migrations of Figure 5.17.

This shows that it is only necessary with  $8s/0.01s = 800$  iterations on a hexagonal lattice. Downsampling by Dirichlet interpolation, Appendix C.2, and the migration result is given in Figure 5.20. This is calculated with 200 less iterations than the previous and the cpu time is reduced even further, now approximately 3.5 s.

For the migration to be exact on a hexagonal lattice the velocity function should be constructed here, and the modeling should be calculated on a hexagonal lattice. The modeling scheme from Gazdag (1981), which essentially is the inverse operation of RTM, could be calculated on such a lattice, but for testing a algorithm it is preferable to use another modeling.

### Constant Velocity Fourier Modeled Data

A synthetic model which contains a wide range of dips are shown in Figure 5.21(a). In this example the modeling is done in Fourier domain with a constant velocity  $c = 1.5$  km/s. Constant velocity imply that all the reflection coefficient are only a result of differences in density. The Fourier transform of the model  $f = f(x, z)$  is given

$$F(k_x, k_z) = \int \int_{-\infty}^{\infty} f(x, z) e^{-i(xk_x + zk_z)} dx dz. \quad (5.48)$$

The dispersion relation of the acoustic wave equation defines the map

$$k_x = \sqrt{\left(\frac{\omega}{c}\right)^2 + k_z^2}, \quad (5.49)$$

which gives

$$S(k_x, \omega) = F\left(k_x, \sqrt{\left(\frac{\omega}{c}\right)^2 + k_x^2}\right). \quad (5.50)$$

where  $S(k_x, \omega)$  is the Fourier spectrum of the seismic section. Inverse Fourier transform results in zero-offset seismic,

$$s(x, t) = \mathcal{F}^{-1}[S(k_x, \omega)]. \quad (5.51)$$

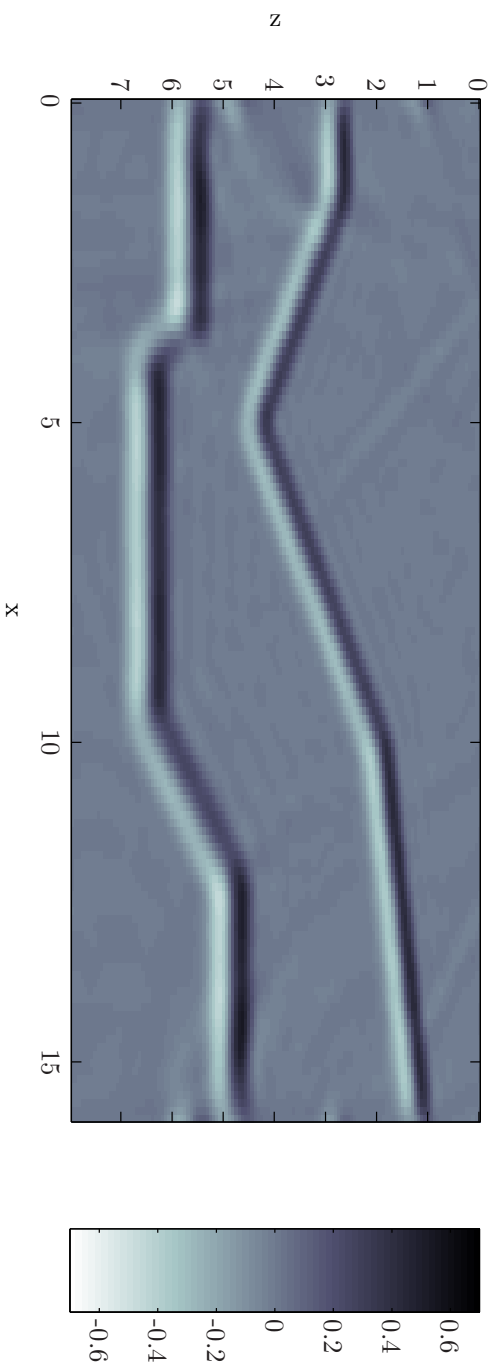
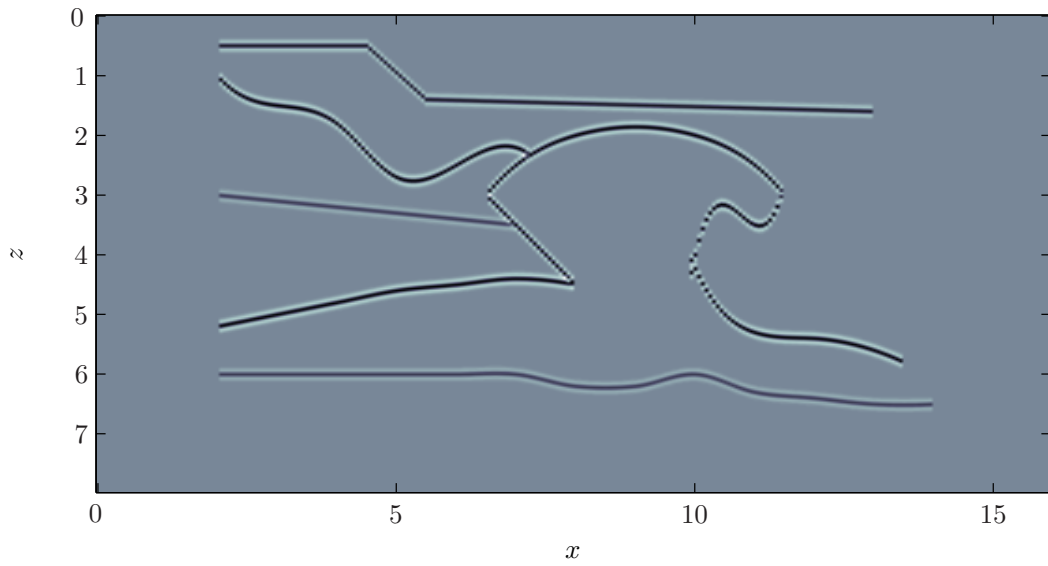
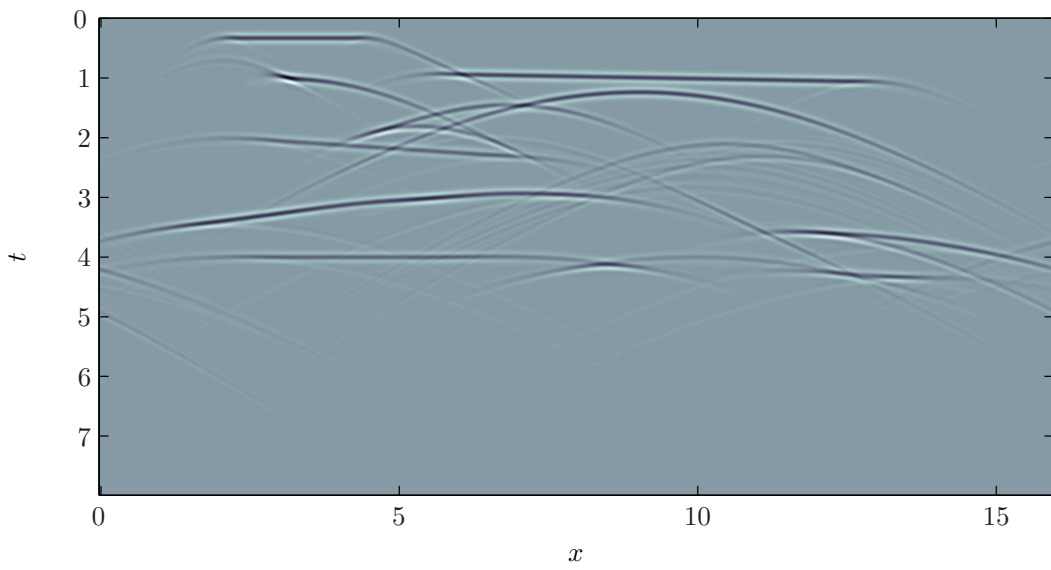


Figure 5.20: RTM result with 800 time steps opposed to 1000 for conventional migration



(a) Synthetic model with constant velocity  $c = 1.5$  km/s



(b) Synthetic data modeled with FK-modeling

Figure 5.21: Synthetic model and constant velocity modeled seismic

	Number of time steps	Calculation time
Rectangular, Kirchhoff data	1000	5.2 s
Hexagonal, Kirchhoff data	1000	4.5 s
Hexagonal, Kirchhoff data	800	3.5 s
Rectangular, FK modeled data	1348	32.8 s
Hexagonal, FK modeled data	1201	24.4 s

Table 5.1: Summary of different RTMs performed.

This is in principle the inverse operation of the FK or Stolt migration, (Stolt and Benson, 1986), except for the amplitude correction, it does not allow for varying velocities in any direction.

When calculating this discrete map there is need for interpolation, and the Dirichlet kernel described in Appendix C.2 is used. The zero-offset section modeled by this approach is given in Figure 5.21(b). The sampling grid is given by  $\Delta x = 0.0625$  km,  $\Delta z = 0.0312$  km, the number of sampling points is  $N_x = 256$  and  $N_z = 512$ . In Figure 5.21(a) only the first 256 samples are shown, the rest is added to avoid alias in the modeling.

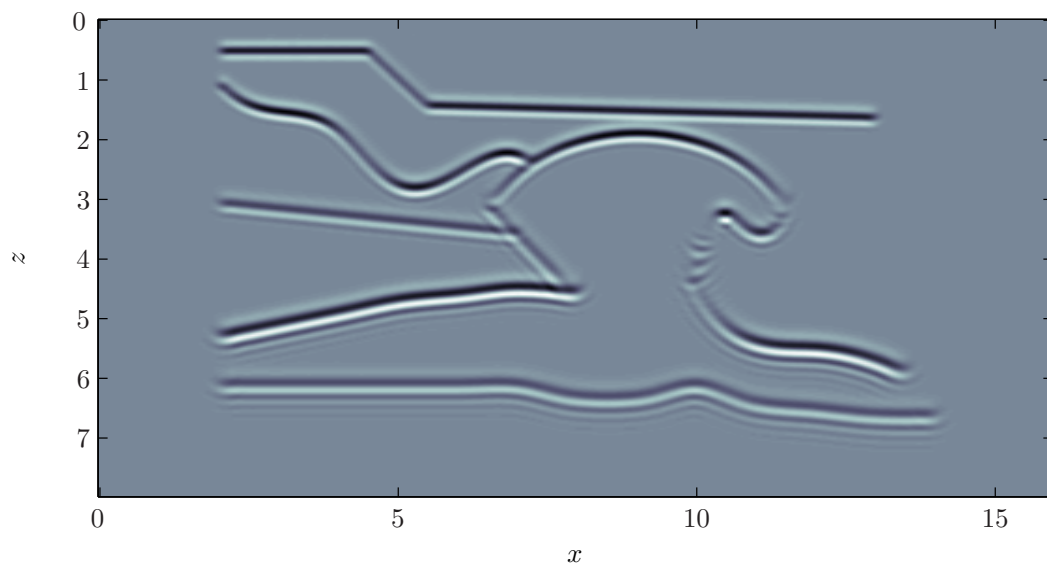
For the RTM on rectangular lattice the stability criteria yields  $\Delta t_{\max} = 0.0059$  s, and there is need for  $N_t = 1348$  time steps until  $t = 0$ . RTM on a rectangular lattice is given in Figure 5.22(a). For the imaging on the hexagonal lattice the time step can be chosen  $\Delta t = 0.006$  s, which yields  $N_t = 1201$ . The result of imaging on the hexagonal lattice is given in Figure 5.22(b). The migration grid is defined with the same sampling intervals as the model, and with  $N_x = N_z = 256$ , since the deepest reflector is shallower than  $N_z \Delta z = 256 \times 0.0312 \approx 8$  km. The hexagonal lattice is defined as in the previous example,  $N = N_x/2$  and  $M = N_x/4$ . After the migration there is applied a circular Blackman low-pass filter with cutoff  $k_z = 100$  rad/km and  $k_x \approx 49$  rad/km. The images are equal except for some oscillations on the hexagonal migration, which could be removed with a lower cutoff. It can be observed that almost all dips are imaged, only the vertical part of the dome are a bit weak, due to coarse sampling.

The rectangular grid have  $N_x \times N_z = 65,536$  sampling points and the hexagonal have  $\det(\mathbf{H}) = 49,152$ , which shows that the hexagonal lattice has 25% less sampling points. The RTM is faster on the hexagonal lattice, since it has fewer sampling points and fewer time steps are necessary, it finishes in 24.4 s compared to the rectangular case which finishes in 32.8 s.

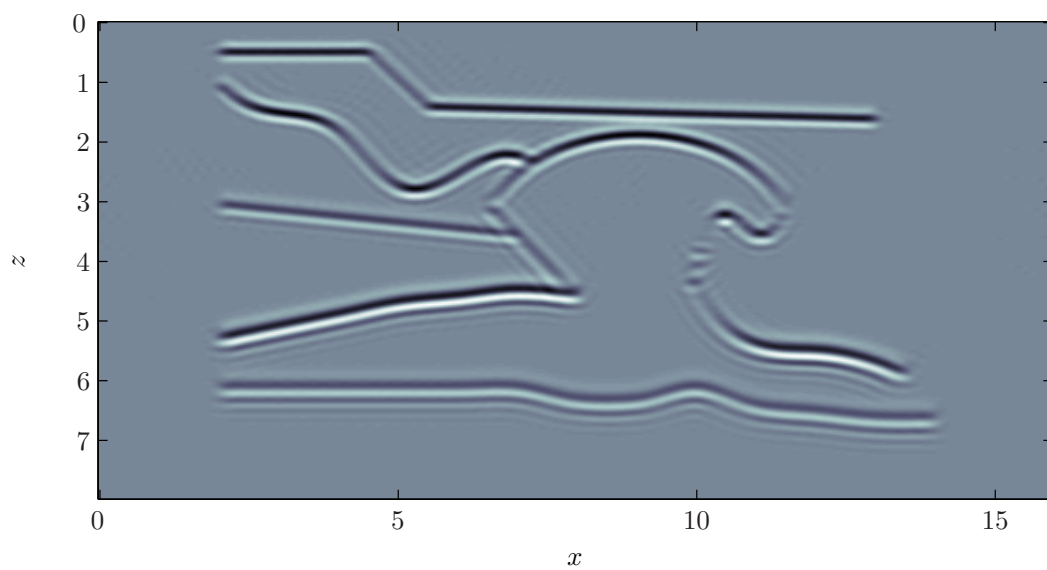
## Comments

The results of RTM on hexagonal lattices are good, the images are the same as the results on rectangular lattices except for some oscillations. Using a hexagonal lattice shows improvement in computation time, the RTM on a hexagonal lattice is faster in both examples. A summary of the computation times is given in Table 5.1. Calculating RTM on a hexagonal lattice also allows for a larger time step than for rectangular sampling, which further reduce the computation time.





(a) RTM on a rectangular lattice



(b) RTM on a hexagonal lattice

Figure 5.22: (a) Result of migration on a rectangular lattice and (b) on a hexagonal lattice.



## Chapter 6

# Summary and Conclusions

A method for calculating the multidimensional DFT with FFT for general periodic signals has been reviewed. The Smith normal form of the matrix defining the periodicity yields simple coordinate transformations to a rectangular grid where the FFT is calculated. Assuming non-rectangular periodicity results in a periodicity in Fourier domain given by the transpose of the periodicity matrix.

For a given set of sampling points there are different periodicities covering the same points which result in different sets of points in Fourier domain. This yields different sampling of the Fourier transform itself.

Hexagonal sampling is preferable for images with circular bandwidth in Fourier domain. It has been shown that the Fourier transform on such lattices can be calculated with different methods. The hexagonal periodicity can be represented with an integer matrix and calculated with FFT, using the Smith normal form theorem.

Seismic data recorded in time is oversampled, and boundaries for the Fourier spectrum are given by the wave equation. An optimal sampling scheme is defined by periodicity matrices, here referred to as Diamond sampling. This is a special case of hexagonal sampling, and the Fourier transform is calculated by the Smith normal form. Using these periodicity matrices on seismic data reduces the number of sampling points with a factor 2. This reduces the need for data storage and makes processing algorithms more efficient. Filtering a seismic section can be accomplished in the rectangular space given as the range of the normal form, which makes it more efficient.

It is well known that the tomographic Radon transform has a hexagonal bandwidth. It is shown that this is also the case for the (geophysical) linear and parabolic Radon transform. Therefore sampling of the transformation could be more efficient by using non-rectangular sampling. The hexagonal Fourier transform with rectangular output could be a candidate for transforming from time to frequency, and thereafter calculating least squares solution for each frequency.

Migrated images have circular bandwidth, therefore it is more efficient migrate on a hexagonal lattice. A 2D and 3D Gazdag phase-shift migration is calculated on non-rectangular sampling grid. The full operation is on the range of the Smith normal form. There is then need for smaller FFT for each extrapolation step, and the process becomes more efficient compared to

migrations on rectangular lattices.

Reverse time migration has been implemented for zero-offset seismic data and a stability condition for the finite difference was derived. The RTM is more efficiently sampled on a hexagonal lattice, in the examples shown there are 25% less sampling points. The algorithm is performed on a lattice generated by assuming hexagonal periodicity in Fourier domain. The results are similar to the rectangular migration. Assuming smaller periodicity gives another stability condition and the recursion can be calculated with fewer time steps, which shows a reduction in calculation time. RTM of two synthetic sections have been shown, and migration on hexagonal grids are more efficient with respect to calculation time. The hexagonal sampling does introduce some more oscillations than the rectangular sampled, as a result of the smaller period, but these could be removed with a low-pass filter.

## Appendix A

# Diagonalization of the Periodicity Matrix

The Smith normal form is used to calculate DFT with FFT on more general grids than the rectangular. This is shown in Chapter 2. In this appendix, a method for calculating the 2D normal form and the matrices  $\mathbf{P}$  and  $\mathbf{Q}$  is presented. These are used in the coordinate maps  $\Gamma$ , which maps a generally sampled function to a rectangular lattice given by  $\mathcal{R}(\mathbf{D})$ , where  $\mathbf{D}$  is the Smith normal form. Different aspects of the coordinate map matrices are covered and important results on normal forms in more than 2D are presented. In the last section an algorithm for finding the Smith normal form is implemented in MATLAB.

### A.1 Smith Normal Form

Let  $\mathbb{Z}$  be the set of integers, and  $\mathbf{P}$  and  $\mathbf{Q}$  be unimodular matrices with  $\det(\mathbf{P}) = \det(\mathbf{Q}) = \pm 1$ . Any matrix in  $M_n(\mathbb{Z})$ ,  $n \times n$  integer matrices, can be written on the Smith normal form  $\mathbf{D} = \mathbf{P}^{-1}\mathbf{A}\mathbf{Q}^{-1}$  where  $\mathbf{D}$  is diagonal and the diagonal elements  $d_i$  is divisors of  $d_{i+1}$ , which is written  $d_1|d_2|\dots|d_n$  (Morandi, 2005). The simplest solution of this is for  $2 \times 2$  integer matrices,  $M_2(\mathbb{Z})$ , which is the case that will be treated here. In A.7 an algorithm is given for  $n \times n$  matrices.

A general periodicity matrix in  $M_2(\mathbb{Z})$  is defined in Chapter 2 as

$$\mathbf{A} = \begin{pmatrix} a & b \\ c & d \end{pmatrix}.$$

Let  $g_1 = \gcd(a, c)$ , where  $\gcd$  is the greatest common divisor of the two elements,  $a$  and  $c$ , (Fraleigh, 2003). Using the equations

$$\begin{aligned} g_1 &= ax + cy \\ 1 &= \alpha x + \beta y \end{aligned} \tag{A.1}$$

for  $x, y \in \mathbb{Z}$ ,  $a = \alpha g_1$  and  $b = \beta g_1$ , gives the matrix

$$\mathbf{P}_1^{-1} = \begin{pmatrix} x & y \\ -\beta & \alpha \end{pmatrix}$$

which is invertible and unimodular because

$$\det(\mathbf{P}_1^{-1}) = \alpha x + \beta y = 1.$$

Then the product

$$\begin{aligned} \mathbf{P}_1^{-1} \mathbf{A} &= \begin{pmatrix} x & y \\ -\beta & \alpha \end{pmatrix} \begin{pmatrix} a & b \\ c & d \end{pmatrix} \\ &= \begin{pmatrix} ax + by & bx + dy \\ -a\beta + c\alpha & -b\beta + d\alpha \end{pmatrix} \end{aligned}$$

and  $-a\beta + c\alpha = -\alpha g_1 \beta + \beta g_1 \alpha = 0$ , gives

$$\mathbf{P}_1^{-1} \mathbf{A} = \begin{pmatrix} g_1 & \times \\ 0 & \times \end{pmatrix}.$$

The same operations for the first row, instead of the first column of the matrix  $\mathbf{A}$ , results in a zero in the upper right corner. Defining  $g_2 = \gcd(g_1, h_1)$  and then  $g_1 t + h_1 s = f \Rightarrow \lambda t + \mu s = 1$ , and the product

$$\mathbf{A} \mathbf{Q}_1^{-1} = \begin{pmatrix} g_1 & h_1 \\ 0 & h_2 \end{pmatrix} \begin{pmatrix} t & -\mu \\ s & \lambda \end{pmatrix}$$

results in a matrix

$$\mathbf{A} \mathbf{Q}_1^{-1} = \begin{pmatrix} g_2 & 0 \\ \times & \times \end{pmatrix}.$$

It is sometimes necessary to perform these operations several times, depending on the initial matrix. This will give a sequence of divisors  $g_1, g_2, \dots$  which eventually gives  $g_i = g_{i+1} = g_{i+2} \dots$ . The result will then be a matrix on the form

$$\begin{pmatrix} r & 0 \\ p & q \end{pmatrix} \quad \text{or} \quad \begin{pmatrix} r & p \\ 0 & q \end{pmatrix} \tag{A.2}$$

where  $p$  divides  $q$  and a single row operation ( $\mathbf{P}_n^{-1}$ ) will give a diagonal matrix and  $\mathbf{A}$  can be written as

$$\begin{aligned} \mathbf{A} &= \mathbf{P}_1 \dots \mathbf{P}_i \mathbf{D}' \mathbf{Q}_1 \dots \mathbf{Q}_j \\ &= \mathbf{P} \mathbf{A} \mathbf{Q}. \end{aligned} \tag{A.3}$$

This shows that matrices in  $M_2(\mathbb{Z})$  can be written as a product of three integer matrices, where one is diagonal. This diagonalization holds for the calculations in Section 2.4 but for the diagonal matrix  $\mathbf{D} = \text{diag}(a_1, a_2)$  to be of Smith normal form,  $a_1$  must be a divisor of  $a_2$ . When the matrix is reduced to the form  $\mathbf{D}' = \text{diag}(r, q)$ , elementary row and column operations will give the desired result (Morandi, 2005). If  $d = \text{gcd}(r, q) = rx + qy$  for  $x, y \in \mathbb{Z}$  and as before  $q$  and  $r$  can be written as a multiple of  $d$ ,  $r = \rho d, q = \sigma d$ , then adding  $x$  times row one results in the matrix multiplication

$$\begin{pmatrix} 1 & 0 \\ x & 1 \end{pmatrix} \begin{pmatrix} r & 0 \\ 0 & q \end{pmatrix} = \begin{pmatrix} r & 0 \\ rx & q \end{pmatrix}$$

and adding  $y$  times the second column to the first gives

$$\begin{pmatrix} r & 0 \\ rx & q \end{pmatrix} \begin{pmatrix} 1 & 0 \\ y & 1 \end{pmatrix} = \begin{pmatrix} r & 0 \\ rx + qy & q \end{pmatrix} = \begin{pmatrix} r & 0 \\ d & q \end{pmatrix}.$$

Then subtracting  $\rho$  times the second row from the first

$$\begin{pmatrix} 1 & -\rho \\ 0 & 1 \end{pmatrix} \begin{pmatrix} r & 0 \\ d & q \end{pmatrix} = \begin{pmatrix} 0 & -q\rho \\ d & q \end{pmatrix}$$

and column two minus  $\sigma$  times column one results in the anti-diagonal matrix

$$\begin{pmatrix} 0 & -q\rho \\ d & q \end{pmatrix} \begin{pmatrix} 1 & -\sigma \\ 0 & 1 \end{pmatrix} = \begin{pmatrix} 0 & -q\rho \\ d & 0 \end{pmatrix}.$$

Rotating this gives

$$\begin{pmatrix} 0 & 1 \\ -1 & 0 \end{pmatrix} \begin{pmatrix} 0 & -q\rho \\ d & 0 \end{pmatrix} = \begin{pmatrix} d & 0 \\ 0 & q\rho \end{pmatrix},$$

which is the Smith normal form since  $d$  divides  $q\rho$ . All of these operation matrices are unimodular and can be combined to two matrices  $\mathbf{C}$  and  $\mathbf{E}$ .

$$\begin{pmatrix} x & 1 \\ -\sigma y & \rho \end{pmatrix} \begin{pmatrix} r & 0 \\ 0 & q \end{pmatrix} \begin{pmatrix} 1 & -\sigma \\ y & \rho x \end{pmatrix} = \mathbf{C}\mathbf{D}'\mathbf{E} = \mathbf{D} = \begin{pmatrix} d & 0 \\ 0 & q\rho \end{pmatrix}. \quad (\text{A.4})$$

The last equation gives that if  $r$  and  $q$  are relatively prime,  $d = 1$ , the Smith normal form becomes  $\mathbf{D} = \text{diag}(1, q\rho)$  which is unique. In the case where  $r$  and  $q$  are not relatively prime it is unique up to a multiple of the diagonal and the matrix  $\mathbf{A}$ . Equation (A.4) can then be used to find multiple diagonalizations for the same periodicity matrix.

## A.2 Solving the Diophantine Equation

Equation (A.1) is a linear Diophantine equation, these equations are recognized by the fact that they have less equations than unknowns. Since  $g_1$  is the greatest common divisor of  $a$  and  $b$  it can be written on the form

$$\alpha x_0 + \beta y_0 = 1 \quad (\text{A.5})$$

which is the Bézout's identity (Chabert, 1999), where  $x_0$  and  $y_0$  are solutions. It has infinitely many solutions and different choice of solutions will result in different diagonalizations.

An algorithm for finding the greatest common divisor of  $a$  and  $b$ , is the well known Euclidean algorithm. The simplest method is to define  $u = a$  and  $v = b$ , then if  $u > v$  the difference between  $v$  and  $u$  is set to  $u$ . If  $v > u$  the subtraction  $v = v - u$  is done, continuing this until  $u = v$  gives the greatest common divisor,  $\gcd(a, b) = u$ .

To find all the solutions  $(x_0, y_0)$  of equation (A.5), the first step is to define

$$x_0 = \frac{1 - \beta y_0}{\alpha}$$

and then split the fraction in two parts. This will be shown by solving the equation

$$5x + 3y = 1.$$

The solution can be written as

$$x = \frac{1 - 3y}{5} = -y + \frac{1 + 2y}{5} = -y + t \tag{A.6}$$

where

$$t = \frac{1 + 2y}{5} \implies y = 2t + \frac{t - 1}{2} = 2t + u. \tag{A.7}$$

This gives

$$2u = t - 1 \implies t = 2u + 1,$$

which by using equations (A.7) and (A.6) results in all the solutions on the form

$$x_0 = -(1 + 3u) \quad \text{and} \quad y_0 = 5u + 2 \quad \forall u \in \mathbb{Z}.$$

A particular solution is  $x_0 = -1$  and  $y_0 = 2$ , and the solutions of the homogeneous equation is  $x = -3u$  and  $y = 5u$ . This is a general solution of linear equations, and can be compared to solutions of for example linear differential and linear difference equations. The algorithm for solving Diophantine equations equal to the gcd is called the Extended Euclidean algorithm, this gives the particular solutions of the equations. For more details on these algorithms, see Chabert (1999).

### A.3 Diophantine Equations and Smith Normal Form

There are infinitely many solutions to equation (A.1), and the choice of solution will have an impact on the results of the diagonalization. Starting with the periodicity matrix from the example in Section 2.3

$$\mathbf{A} = \begin{pmatrix} 3 & 2 \\ 1 & 4 \end{pmatrix}$$



which gives the first Diophantine equation and solutions

$$3x + y = 1 \implies y = 1 - 3k \quad , \quad x = k \quad \forall k \in \mathbb{Z}.$$

This give the matrix  $\mathbf{P}^{-1}$

$$\mathbf{P}_1^{-1} = \begin{pmatrix} k & 1 - 3k \\ -1 & 3 \end{pmatrix},$$

multiplying with  $\mathbf{A}$  gives

$$\mathbf{P}_1^{-1}\mathbf{A} = \begin{pmatrix} 1 & 4 - 10k \\ 0 & 10 \end{pmatrix}.$$

The next Diophantine equation and solution is then given as

$$s + (4 - 10k)t = 1 \implies s = 1 - (4 - 10k)n, \quad t = n \quad \forall n \in \mathbb{Z}$$

which results in

$$\mathbf{Q}_1^{-1} = \begin{pmatrix} 1 - (4 - 10k)n & 10k - 4 \\ n & 1 \end{pmatrix}.$$

Then multiplication

$$\mathbf{A}\mathbf{Q}_1^{-1} = \begin{pmatrix} 1 & 0 \\ 10n & 10 \end{pmatrix}$$

will give a diagonal matrix after one row operation, written as a matrix

$$\mathbf{P}_2^{-1} = \begin{pmatrix} 1 & 0 \\ -10n & 10 \end{pmatrix}.$$

The Smith normal form is

$$\begin{aligned} \mathbf{D} &= \mathbf{P}_1^{-1}\mathbf{P}_2^{-1}\mathbf{A}\mathbf{Q}_1^{-1} = \begin{pmatrix} k - 10n(1 - 3k) & 1 - 3k \\ -(1 + 30n) & 3 \end{pmatrix} \begin{pmatrix} 3 & 2 \\ 1 & 4 \end{pmatrix} \begin{pmatrix} 1 - (4 - 10k)n & 10k - 4 \\ n & 1 \end{pmatrix} \\ &= \begin{pmatrix} 1 & 0 \\ 0 & 10 \end{pmatrix}. \end{aligned} \tag{A.8}$$

The conclusion is that the choice of  $k$  or  $n$ , hence the solution to the Diophantine equations, has no impact on the final diagonal matrix. But the matrices  $\mathbf{P}$  and  $\mathbf{Q}$  are different and this changes the coordinate transformations  $\Gamma$ , from Section 2.4. Different  $\Gamma$ 's will not make any difference on the final Fourier transformation. For computational speed it would be an advantage to choose  $k$  and  $n$  so the integers of the matrices  $\mathbf{P}$  and  $\mathbf{Q}$  become as small as possible, since the multiplications and modular calculations computed then become smaller.

## A.4 Different Diagonalizations of the Same Matrix

The diagonalization of the matrix  $\mathbf{A}$  from the previous section can be written as

$$\begin{aligned}\mathbf{A} &= \mathbf{PDQ} \\ &= \begin{pmatrix} 3 & -1 \\ 1 & 0 \end{pmatrix} \begin{pmatrix} 1 & 0 \\ 0 & 10 \end{pmatrix} \begin{pmatrix} 1 & 4 \\ 0 & 1 \end{pmatrix} = \begin{pmatrix} 3 & 2 \\ 1 & 4 \end{pmatrix}\end{aligned}\tag{A.9}$$

when  $k = n = 0$ . The periodicity matrix  $\mathbf{A}$  has  $\det(\mathbf{A}) = 10$  sampling points, and the Smith normal form is here given as  $\mathbf{D} = \text{diag}(1, 10)$ . It should be possible to find a diagonalization with  $\mathbf{D}_2 = \text{diag}(2, 5)$ , since  $\det(\mathbf{D}_2) = 10$ . The integers 2 and 5 are not divisors of each other and they are relatively prime,  $\gcd(2, 5) = 1$ . Using equation (A.4) it is possible to find a relationship between these two diagonal matrices. The equation  $2x + 5y = d = 1$  have particular solutions  $x = -2$  and  $y = 1$ , dividing by  $d$  gives  $\rho = 2$  and  $\sigma = 5$ . By direct input to the equation this results in

$$\mathbf{D} = \begin{pmatrix} 1 & 0 \\ 0 & 10 \end{pmatrix} = \begin{pmatrix} -2 & 1 \\ -5 & 2 \end{pmatrix} \begin{pmatrix} 2 & 0 \\ 0 & 5 \end{pmatrix} \begin{pmatrix} 1 & -5 \\ 1 & -4 \end{pmatrix} = \mathbf{CD}_2\mathbf{E}.$$

This and equation (A.9) gives another diagonalization of the same matrix

$$\begin{aligned}\mathbf{A} &= \mathbf{PCD}_2\mathbf{EQ} \\ &= \mathbf{P}_2\mathbf{D}_2\mathbf{Q}_2 \\ &= \begin{pmatrix} -1 & 1 \\ -2 & 1 \end{pmatrix} \begin{pmatrix} 2 & 0 \\ 0 & 5 \end{pmatrix} \begin{pmatrix} 1 & -1 \\ 1 & 0 \end{pmatrix}.\end{aligned}\tag{A.10}$$

This is not Smith normal form, but it can be used as a diagonalization for calculation of the 2D DFT. These are the two diagonal matrices possible for  $\mathbf{A}$ , since  $\det(\mathbf{A}) = 10 = 1 \times 10 = 2 \times 5$ . This method for finding equivalent diagonalizations can only be used when the goal is to find a diagonal matrix which is not of normal form. An example where the method cannot be used, is a matrix with determinant equal to 16, then the possible factors  $1 \times 16 = 2 \times 8 = 4 \times 4$  all give diagonal matrices of normal form.

For the case of calculating 2D DFT these different diagonalizations make no difference on the final result, but it can have an impact on the speed of the computations. If it is possible to find a diagonal matrix which have first entry equal to one, then there is only need for 1D DFT, this could speed up the computations. The coordinate transformations  $\Gamma$  in Section 2.4 should be as small as possible to minimize time used for the operations.

## A.5 The Smith Normal Form in $n$ -Dimensions

As mentioned in Section A.1 the Smith normal form can be found for integer matrices of  $n$  dimensions,  $\mathbf{A} \in M_n(\mathbb{Z})$ . The matrix from the example in Section 2.7,

$$\mathbf{A} = \begin{pmatrix} 3 & 2 & 1 \\ 1 & 4 & 1 \\ 1 & 2 & 3 \end{pmatrix},$$

has Smith normal form

$$\mathbf{D} = \begin{pmatrix} 1 & 0 & 0 \\ 0 & 2 & 0 \\ 0 & 0 & 12 \end{pmatrix},$$

and the unimodular matrices

$$\mathbf{P} = \begin{pmatrix} 3 & 4 & 1 \\ 1 & -5 & -1 \\ 1 & 0 & 0 \end{pmatrix}, \quad \mathbf{Q} = \begin{pmatrix} 1 & 2 & 3 \\ 0 & 1 & 5 \\ 0 & -1 & -4 \end{pmatrix}.$$

By doing the coordinate transform  $\Gamma$  from Section 2.4 the samples are mapped to  $\mathcal{R}(\mathbf{D})$  which is  $\mathbb{Z}_1 \times \mathbb{Z}_2 \times \mathbb{Z}_{12} \cong \mathbb{Z}_2 \times \mathbb{Z}_{12}$  and a 2D FFT is possible. This property is interesting because it can make the Fourier transformation more efficient.

The first step of finding the Smith normal form of a matrix is to reduce it to a diagonal  $\text{diag}(d_1, d_2, \dots, d_n)$  with no specific requirements on the elements. Further it is possible to find the Smith normal form, where the diagonal elements have the property  $d_j | d_{j+1}$  for  $j = 1, \dots, n-1$ . Rayward-Smith (1979) suggests an interesting method for finding the final form. Given an  $n$ -dimensional matrix, the diagonal elements are given as a set  $S = \{d_i\}_{i=1,2,\dots,n}$ , and  $S_k$  is the set of possible  $k$  products in this set. Let  $\text{hcf}(S_k)$  where  $k \leq n$  be the highest common factor of the elements in  $S_k$ , which is the highest number the prime factorisations of each element in  $S_k$  have in common. Then by defining the integers  $\delta_1 = \text{hcf}(S), \delta_2 = \text{hcf}(S_2), \dots, \delta_i = \text{hcf}(S_i)$ , the invariant factors of the smith normal form can be computed as

$$\begin{aligned} s_1 &= \delta_1 \\ s_2 &= \frac{\delta_2}{\delta_1} \\ &\dots \\ s_i &= \frac{\delta_i}{\delta_{i-1}}, \end{aligned} \tag{A.11}$$

and the final matrix becomes  $\mathbf{D} = \text{diag}(s_1, s_2, \dots, s_n)$ .

Starting with the matrix

$$\begin{pmatrix} 3 & 0 & 0 \\ 0 & 14 & 0 \\ 0 & 0 & 9 \end{pmatrix}.$$

which is an example where the diagonal elements do not have the property  $d_j | d_{j+1}$ . The computations become

$$\begin{aligned} \delta_1 &= \text{hcf}(3, 14, 9) = \text{hcf}(1 \times 3, 1 \times 2 \times 7, 1 \times 3 \times 3) = 1 \\ \delta_2 &= \text{hcf}(3 \times 9, 3 \times 14, 9 \times 14) = \text{hcf}(42, 126, 27) = 3 \\ \delta_3 &= \text{hcf}(3 \times 14 \times 9) = 378 \end{aligned}$$

and

$$\begin{aligned} s_1 &= 1 \\ s_2 &= \frac{3}{1} = 3 \\ s_3 &= \frac{378}{3} = 126. \end{aligned}$$

The Smith normal form is  $\text{diag}(1, 3, 126)$ . This shows that the computation of the  $\text{hcf}(\times)$  can be done by prime factor expansion, a computer algorithm for this is given by Rayward-Smith (1979).

This gives an interesting result, the rectangular sampling geometry in  $n$  dimensions are given by a diagonal periodicity matrix which is  $n \times n$ . If the highest common factor of these diagonal elements are one,  $\text{hcf}(d_1, \dots, d_n) = 1$ , the final Smith diagonal form will have the first element equal to 1 and an  $n$ -dimensional Fourier transform can be reduced to  $(n - 1)$ . As before a 2D can be reduced to 1D, and 3D to a 2D. Further if  $\text{hcf}(S_2) = 1$  the Fourier Transform is actually reduced to  $(n - 2)$ -dimensions. An example of this is the lattice generated by the matrix

$$\begin{pmatrix} 3 & 0 & 0 \\ 0 & 5 & 0 \\ 0 & 0 & 7 \end{pmatrix}, \tag{A.12}$$

which will have smith normal form

$$\begin{pmatrix} 1 & 0 & 0 \\ 0 & 1 & 0 \\ 0 & 0 & 105 \end{pmatrix}. \tag{A.13}$$

This is a possibility when all the diagonal entries are relatively prime. An algorithm and a implementation of the Smith normal form for  $n \times n$  matrices is given in Appendix A.7.

## A.6 Bricklaying over Lattices

The Hermite normal form (HNF) of an integer matrix is a matrix on the form

$$\mathbf{H} = \begin{pmatrix} \times & 0 & \cdots & 0 \\ \times & \times & \cdots & 0 \\ \vdots & \vdots & \ddots & \vdots \\ \times & \times & \times & \times \end{pmatrix}, \tag{A.14}$$

which is called lower triangular and the  $\times$  are positive integers. This form is found by doing unimodular matrix column operations, which is adding a multiple of one column to another, changing position of two columns and multiplying a column by  $-1$ . These operations can be written as matrix multiplications, and the HNF of a matrix  $\mathbf{A}$  can be given  $\text{HNF}(\mathbf{A}) = \mathbf{H} =$

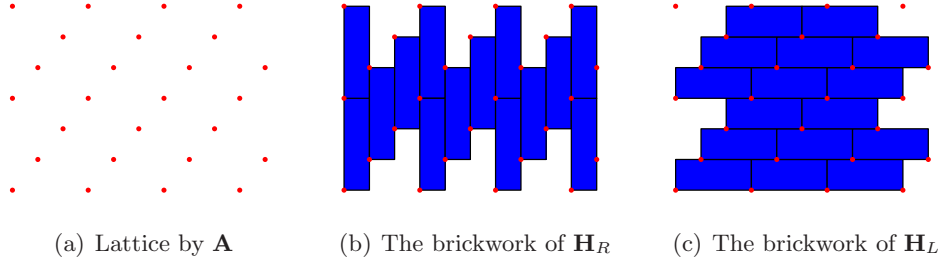


Figure A.1: A geometric interpretation of the Hermite normal form

$\mathbf{A}\mathbf{G}$ , where  $\mathbf{G}$  is unimodular. It is possible to find two forms of the HNF, the left HNF,  $\mathbf{H}_L$ , which is an upper triangular matrix and right HNF,  $\mathbf{H}_R$ , which is lower triangular. Gilbert (1993) presents a geometrical interpretation of matrices on this form.

Let the matrix

$$\mathbf{A} = \begin{pmatrix} 2 & -1 \\ -1 & 2 \end{pmatrix} \quad (\text{A.15})$$

span a sampling lattice, see Figure A.1(a). By doing unimodular column operations

$$\begin{pmatrix} 2 & -1 \\ -1 & 2 \end{pmatrix} \sim \begin{pmatrix} -1 & 2 \\ 2 & -1 \end{pmatrix} \sim \begin{pmatrix} -1 & 0 \\ 2 & 3 \end{pmatrix} \sim \begin{pmatrix} 1 & 0 \\ 1 & 3 \end{pmatrix} \quad (\text{A.16})$$

the right HNF is

$$\mathbf{H}_R = \begin{pmatrix} 1 & 0 \\ 1 & 3 \end{pmatrix}. \quad (\text{A.17})$$

If the first diagonal element represent the length along the first axis and the second element the second axis, the size of the bricks will be the product of these elements. Since all the operations for finding the Hermite normal form is unimodular,  $\det(\mathbf{G}) = \pm 1$ , the area of the bricks are given  $\det(\mathbf{H}_R) = \det(\mathbf{A})$ . The lower left element represents the offset to the next brick along the second coordinate. By these rules the brickwork shown in Figure A.1(b) is generated by the right Hermite normal form of the matrix  $\mathbf{A}$ .

The left Hermite normal form is found by a different set of column operations and becomes

$$\mathbf{H}_L = \begin{pmatrix} 3 & 1 \\ 0 & 1 \end{pmatrix}. \quad (\text{A.18})$$

Using the same approach as for the right Hermite normal form, the resulting brickwork is given in Figure A.1(c). The column operations are in this case also unimodular, so the resulting bricks have the same area. But the complete brickwork becomes different, since the shifting is in the opposite direction.

Gilbert (1993) also presents a geometric representations of the HNF in 3 dimensions. These brickworks becomes somewhat more complicated since then the bricks are translated in two directions.

## A.7 The $n \times n$ Smith Normal Form Algorithm

Many algorithms for fast computations of the Smith normal form of integer matrices are developed. The straight forward implementation will be outlined here, and a MATLAB code is given in A.7.1. This algorithm is given in Rayward-Smith (1979). The algorithm will give an explosive growth in size of the intermediate entries and another method with better performance is presented by Havas and Majewski (1997).

The Smith normal form of a  $n \times n$  matrix  $\mathbf{A}$  is given  $\mathbf{D} = \mathbf{EAH}$  where  $\mathbf{D}$  is diagonal,  $\mathbf{E}$  and  $\mathbf{H}$  are results of respectively elementary unimodular row and column operations. These operations are

- Add or subtract a integer multiple of one row/column to another
- Permute rows and columns
- Multiplying a row/column by  $-1$ .

It can be seen that all operations will have  $\det(\times) = \pm 1$ , which also shows the operations are invertible.

Then the steps in the computation are

1. Permuting rows and columns until the matrix element  $a_{1,1}$  is the smallest one in absolute value, done by the sortmatrix function in A.7.1.
2. If  $a_{1,k}$  for  $k \neq 1$  is a non zero element in the first column, using the division algorithm with respect to the first entry reduces the element to the smallest integer possible. Defining  $q = \lfloor \frac{a_{1,k}}{a_{1,1}} \rfloor$  gives the rest  $r$  of a column operation as  $r = a_{1,k} - a_{1,1}q$ . Then if  $r = 0$ , continue to the next entry, if it is not go back to step 1. This should be done until all the entries of column 1 except for  $a_{1,1}$  is zero. Then the same is done for the first row. These steps are implemented in the MATLAB functions reduceCol and reduceRow.
3. When all the entries of the first row and column are zero, as in equation A.19, the first entry should be a divisor of all the entries which are unequal to zero. If  $a_{j,i}$  is not divisible by  $a_{1,1}$  add the column containing this element to the first column and go back to step 1. Both testing for zero in the first row and column, and if  $a_{1,1}$  is a divisor of the rest of the elements is done by the isdivisorzero.m code.

$$\left( \begin{array}{c|ccc} a_{1,1} & 0 & \cdots & 0 \\ \hline 0 & a_{2,2} & \cdots & a_{2,n} \\ \vdots & \vdots & \ddots & \vdots \\ 0 & a_{n,2} & \cdots & a_{n,n} \end{array} \right) \quad (\text{A.19})$$

4. If the diagonal element is negative, multiply by  $-1$ . Then continue by defining the matrix as in A.20, and go back to step 1.

$$\left( \begin{array}{ccc} a_{2,2} & \cdots & a_{2,n} \\ \vdots & \ddots & \vdots \\ a_{n,2} & \cdots & a_{n,n} \end{array} \right) \quad (\text{A.20})$$

This procedure should be done until all the elements except for the diagonal is zero, the diagonal is positive, and  $d_i|d_{i+1}$ . Then the matrix is on Smith normal form.

The MATLAB script returns the matrices  $\mathbf{A} = \mathbf{PDQ}$ , where  $\mathbf{P} = \mathbf{E}^{-1}$  and  $\mathbf{Q} = \mathbf{H}^{-1}$ , for direct usage with the Fourier calculations in Section 2.4.

### A.7.1 MATLAB codes

#### smithnormalform.m

```

1  %[D,P,Q] = smithnormalform(A)
2  % Finds the smith normal form of a square integer matrix A, returns
3  % unimodular matrices P and Q, such that A = PDQ, (D = EAH), where D is of
4  % smith normal form.
5  % Depends on the functions: reduceRow(), reduceCol(), sortmatrix() and
6  % isdivisorzero()
7  function [D,P,Q] = smithnormalform(A)
8  n =length(A);
9  E = eye(n);
10 H = eye(n);
11 Etemp = eye(n); Htemp = eye(n);
12 i = 1;
13 while i < n %runs untill the matrix A is in Smith Normal Form
14
15     [A1,E1,H1] = sortmatrix(A(i:n,i:n)); %putting the smallest integer to A(i,i)
16     A(i:n,i:n) = A1;
17     Etemp(i:n,i:n) = E1;
18     E = Etemp*E;
19     Htemp(i:n,i:n) = H1;
20     H = H*Htemp;
21     Etemp = eye(n); Htemp = eye(n);
22
23     [A1,E1,H1] = reduceCol(A(i:n,i:n));%Elementary column operations
24     A(i:n,i:n) = A1;
25     Etemp(i:n,i:n) = E1;
26     E = Etemp*E;
27     Htemp(i:n,i:n) = H1;
28     H = H*Htemp;
29     Etemp = eye(n); Htemp = eye(n);
30
31     [A1,E1,H1] = reduceRow(A(i:n,i:n));%Elementary row operations
32     A(i:n,i:n) = A1;
33     Etemp(i:n,i:n) = E1;
34     E = Etemp*E;
35     Htemp(i:n,i:n) = H1;
36     H = H*Htemp;
37     Etemp = eye(n); Htemp = eye(n);
38
39     if A(i,i) <0 % is the diagonal element is negative, multiply by -1
40         H1 = eye(n);
41         H1(i,i) = -1;
42         A = A*H1;
43         H = H*H1;
44     end
45

```

```

46     %Is A(i,i) a divisor and is the first row and colum zero except for
47     %A(i,i).
48     [zero,divisor,column] = isdivisorzero(A(i:n,i:n));
49     if divisor ==1 && zero == 1
50         i = i+1;
51     elseif divisor == 0 && zero == 1
52         Col = eye(n);
53         Col(column,i) = 1;
54         A = A*Col;
55         H = H*Col;
56     end
57 end
58
59 if A(n,n) < 0 % if the last diagonal element is negative, multiply by -1
60     H1 = eye(n);
61     H1(i,i) = -1;
62     A = A*H1;
63     H = H*H1;
64 end
65
66 D=A;
67 P = round(inv(E));
68 Q = round(inv(H));

```

### sortmatrix.m

```

1  %[A,E,H] = sortmatrix(A),
2  % Searches for the smallest integer in a square matrix A, finds unimodular
3  % matrices E and H which moves this number to A(1,1).
4  function [A,E,H] = sortmatrix(A)
5  %Size of the matrix to sort
6  n = length(A);
7  %Permutation matrices
8  Pcol(n,1) = 1; Pcol(:,2:n) = eye(n,n-1);
9  Prow(1,n) = 1; Prow(2:n,:) = eye(n-1,n);
10 ismall = 1; jsmall = 1;
11 for i=1:n
12     for j =1:n
13         if A(ismall,jsmall) == 0 %if the first entry is zero, change the initial point
14             ismall = ismall+1;
15         elseif abs(A(ismall,jsmall)) > abs(A(i,j)) && abs(A(i,j)) > 0
16             ismall = i;
17             jsmall = j;
18         end
19     end
20 end
21 A = Prow^(n-ismall+1) * A * Pcol^(n-jsmall+1);
22 E = Prow^(n-ismall+1);
23 H = Pcol^(n-jsmall+1);

```

### reduceRow.m

```

1  %[A,E,H] = reduceRow(A)

```



```

2 %   reduceRow does elementary unimodular row operations to a square matrix
3 %   A. Returns the reduced matrix and the operations matrices E and H.
4 function [A,E,H] = reduceRow(A)
5 n = length(A);
6 j =2;
7 Row = eye(n);
8 H = eye(n); E = H;
9 while j ≤ n
10     aj1 = A(j,1); a11 = A(1,1);
11     q = floor(aj1/a11);
12     r = aj1 - a11*q;
13     Row(j,1) = -q;
14     A = Row*A;
15     E = Row*E;
16     Row = eye(n);
17
18     [A1,E1,H1] = sortmatrix(A);
19     A = A1;
20     E = E1*E;
21     H = H*H1;
22     if r == 0
23         j = j +1;
24     end
25 end

```

## reduceCol.m

```

1 %[A,E,H] = reduceCol(A)
2 %   reduceCol does elementary unimodular column operations to a square matrix
3 %   A. Returns the reduced matrix and the operations matrices E and H.
4 function [A,E,H] = reduceCol(A)
5 n = length(A);
6 k = 2;
7 Col = eye(n);
8 E = eye(n);
9 H = eye(n);
10 while k ≤ n
11     alk = A(1,k); a11 = A(1,1);
12     q = floor(alk/a11);
13     r = alk - a11*q;
14     Col(1,k) = -q;
15     A = A*Col;
16     H = H*Col;
17     Col = eye(n);
18
19     [A1,E1,H1] = sortmatrix(A);
20     A = A1;
21     E = E1*E;
22     H = H*H1;
23     if r == 0
24         k = k+1;
25     end
26 end

```

## isdivisorzero.m

```
1  %[zero,isdivisor,column] = isdivisorzero(A),
2  %   A is a n x n matrix, isdivisorzero finds if the first row and column
3  %   are zero except for the first entry A(1,1), then returns the boolean
4  %   variable zero = 1 if true and zero = 0 if false. If A(1,1) is divisor
5  %   of all the entrys of the submatrix A(2:n,2:n) then the boolean variable
6  %   isdivisor = 1, if not isdivisor = 0 and column gives the integer number
7  %   of the column which contains the number wich A(1,1) does not divide.
8  function [zero,yes,column] = isdivisorzero(A)
9  n = length(A);
10 yes = 1;
11 column = 0;
12 zero = 0;
13 for i = 2:n
14     for j = 2:n
15         if floor(A(i,j)/A(1,1))  $\neq$  A(i,j)/A(1,1)
16             yes = 0; column = j;
17         end
18     end
19 end
20
21 if A(1,2:n) == zeros(1,n-1)
22     if A(2:n,1) == zeros(n-1,1)
23         zero = 1;
24     end
25 end
```

# Appendix B

## Voronoi Diagrams

Voronoi diagrams have a wide range of applications, for example in anthropology, astronomy, biology, chemistry, physics and geophysics. It will be used here for plotting 2D functions sampled on general sampling grids.

In the 17th century Descartes used Voronoi like diagrams to show the disposition of matter in the solar system. Dirichlet later used it in his studies of positive definite quadric forms in two and three dimensions. It has its name after Georgy Fedoseevich Voronoy (1868 - 1908) which used it for the same application but in  $m$ -dimensions, (Okabe et al., 2009).

Let  $P$  be a set of  $n$  distinct points in the 2D plane,  $P = \{p_1, p_2, \dots, p_n\}$ . The points can be defined as vectors  $\mathbf{x}_i = (x_i, y_i)^T$ , and the distance from a given points  $p$  to  $p_i$  can be given by the Euclidean norm,

$$\|\mathbf{x} - \mathbf{x}_j\| = \sqrt{(x - x_j)^2 + (y - y_j)^2}. \quad (\text{B.1})$$

If the nearest point or one of the nearest points to  $p$  is  $p_i$ , the relation,

$$\|\mathbf{x} - \mathbf{x}_i\| \leq \|\mathbf{x} - \mathbf{x}_j\| \text{ for } i \neq j \text{ where } i, j \in \mathbb{Z}_n \quad (\text{B.2})$$

holds. Then the planar Voronoi polygon to a points  $p_i$  can be given as

$$V(p_i) = \{\mathbf{x} \mid \|\mathbf{x} - \mathbf{x}_i\| \leq \|\mathbf{x} - \mathbf{x}_j\| \text{ for } i \neq j \text{ where } i, j \in \mathbb{Z}_n\}. \quad (\text{B.3})$$

This leads to the definition of the Voronoi diagram for the point set  $P$  in the 2D plane

$$\mathcal{V} = \{V(p_1), \dots, V(p_n)\} \quad (\text{B.4})$$

Okabe et al. (2009). A Voronoi diagram of a random point set is given in Figure B.1.

The Voronoi diagram gives cells that encloses sampling points with the minimum distance. Generally when plotting 2D functions sampled on a non-rectangular lattice interpolation is needed. To avoid interpolation, it could be preferable to fill Voronoi cells with color representing the functions value. Examples of Voronoi diagrams are shown in Section 3.3.1 and 3.3.2. An example of an image by filling these cells are shown in Figure 4.5.

A MATLAB code which generates these plots are given below.

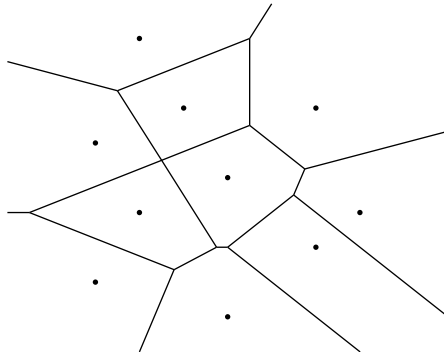


Figure B.1: Example of Voronoi diagram of 10 points

### image\_voronoi.m

```

1  %[] = image_voronoi(eta,dx,dy,fv)
2  %   Finds the voronoi cells for a lattice given by eta, and
3  %   fills these cells with colors from the function fv.
4  %   eta - samplingpoints, column vector
5  %   dx,dy - sampling interval, if integer samplingpoints dx = 1
6  %   fv - the function in a vector corresponding to eta
7  function image_voronoi(eta,dx,dy,fv)
8
9  %first put one row with points over the lattice, so the voronoi diagram converges.
10 max_x_retn = max(eta(:,1));
11 max_y_retn = max(eta(:,2));
12 min_x_retn = min(eta(:,1));
13 min_y_retn = min(eta(:,2));
14 k = 1;
15 [p,q] = size(eta);
16 eta(k*p+1:length(min_x_retn-1:max_x_retn+1)+(k*p),1) = [min_x_retn-1:max_x_retn+1];
17 eta(k*p+1:length(min_x_retn-1:max_x_retn+1)+k*p,2) = ...
18 ones(length(k*p+1:length(min_x_retn-1:max_x_retn+1)+k*p),1)*(min_y_retn-1);
19 %under the lattice.
20 k = 2;
21 eta(k*p+1:length(min_x_retn-1:max_x_retn+1)+(k*p),1) = [min_x_retn-1:max_x_retn+1];
22 eta(k*p+1:length(min_x_retn-1:max_x_retn+1)+k*p,2) = ...
23 ones(length(k*p+1:length(min_x_retn-1:max_x_retn+1)+k*p),1)*(max_y_retn+1);
24 [v,c]=voronoi(eta,{'Qbb'});
25 for i = 1:length(c)
26 if all(c{i}~=1) && i <= p      %If one of the indices is 1 the region is open,
27                               % i <= p Fill cells only for the sampling
28                               % points.
29 o = patch(v(c{i},1),v(c{i},2),fv(i)); % use color i.
30 set(o,'edgecolor','none')
31 end
32 end
33 hold on, axis([min_x_retn max_x_retn min_y_retn max_y_retn])
34 return

```

## Appendix C

# Interpolation

There are many interpolation methods in the literature, and to compare the quality of the different methods it is important to analyze the Fourier spectrum, (Maeland, 1988).

Generally interpolation is a result of the Nyquist-Shannon sampling theorem, any bandlimited function  $f(t)$  can be written as the convolution

$$f(t) = \sum_{-\infty}^{\infty} f_n \text{sinc}(\pi(t - t_n)/\Delta t) \quad \text{for} \quad \Delta t = \frac{\pi}{\Omega}, \quad (\text{C.1})$$

where  $\Omega$  is the bandwidth. The sinc function (Cardinal Sine) is defined on an unlimited aperture. Hence, in general the interpolation from discrete sequences to new sampling points are given

$$f(t) = \sum_{n=0}^{N-1} f_n u(t - n\Delta t) = f_n * u, \quad (\text{C.2})$$

where  $N$  is the number of sampling points,  $\Delta t$  the original sampling interval and  $u = u(t)$  is the interpolation kernel. There are many possibilities for choosing the interpolation kernel. For example, linear interpolation, which is the midpoint between two values, has kernel

$$u_b(t) = \begin{cases} 1 - |t|/\Delta t & \text{for } |t| \leq \Delta t \\ 0 & \text{otherwise} \end{cases}, \quad (\text{C.3})$$

which is the Bartlett window. Another example is the cubic spline which are constructed with the Parzen window,

$$u_p(t) = \begin{cases} (A + 2)|t/\Delta t|^3 - (A + 3)|t/\Delta t|^2 + 1 & \text{for } 0 \leq |t/\Delta t| \leq 1 \\ A(|t/\Delta t|^3 - 5|t/\Delta t|^2 + 8|t/\Delta t| - 4) & \text{for } 1 \leq |t/\Delta t| \leq 2 \\ 0 & \text{otherwise} \end{cases} \quad (\text{C.4})$$

where  $A$  is a free parameter. Maeland (1988) shows that the general interpolation kernel is a low pass filter in Fourier domain.

The resampling of data on a rectangular lattice to a hexagonal is generally a downsampling. There are many techniques for this operation, there are developed special interpolation kernels for given lattices. Ville et al. (2002) presents a spline model for both rectangular and hexagonal lattices, a least squares resampling technique between regular lattices. This is beyond the scope of this work, and 2D resampling, both upsampling and downsampling, are done by MATLABs implementation of the biharmonic spline interpolation (Sandwell, 1987) when needed.

In Section C.2 there is presented an example where the interpolation kernel is the Dirichlet kernel, often referred to as the discrete sinc function. Using this allows full bandwidth in Fourier domain, which is an advantage when interpolation of seismic which are often approximated by Fourier waves.

## C.1 Fourier Interpolation

One of the simplest interpolation methods of a discrete signal  $f_n$  is filling in  $(M - 1)N$  zeros after the signal in Fourier domain. If the signal is real, Fourier domain is Hermite, the zeros have to be placed in the middle of Fourier domain to keep the symmetry, and a real signal after inverse DFT. The signal then have a total of  $(M - 1)N$  interpolated values.

A discrete signal can be written with the DFT

$$f_n = \sum_{k=0}^{N-1} F_k e^{2\pi i k n / N}, \quad (\text{C.5})$$

and by defining  $\tilde{n} = n + \alpha$ , where  $0 \leq \alpha < 1$ , it is possible to define the signal

$$f_{n+\alpha} = \sum_{k=0}^{N-1} [F_k e^{2\pi i k \alpha / N}] e^{2\pi i k n / N}. \quad (\text{C.6})$$

Here  $G_k(\alpha) = e^{2\pi i k \alpha / N}$  is a interpolation filter which gives the functions values at the new points  $n + \alpha$ . The filter  $G_k$  is generally not Hermitian,  $G_{N-k} \neq G_k^*$ , since

$$G_{N-k} = e^{2\pi i (N-k) \alpha / N} = e^{2\pi i \alpha} G_k^*. \quad (\text{C.7})$$

To get real values from the interpolation, the filter have to be Hermitian. Letting

$$\hat{n} = \text{mod}(n + \lfloor N/2 \rfloor, N) - \lfloor N/2 \rfloor, \quad (\text{C.8})$$

which are the sampling points symmetric about the origin, results in a Hermitian filter if  $N$  is odd. If  $N$  is a even number,  $\lfloor N/2 \rfloor = \lceil N/2 \rceil$ , the filter at the Nyquist number becomes

$$G_{N/2}(\alpha) = e^{\pi i \alpha} = \cos(\pi \alpha) + i \sin(\pi \alpha) \quad (\text{C.9})$$

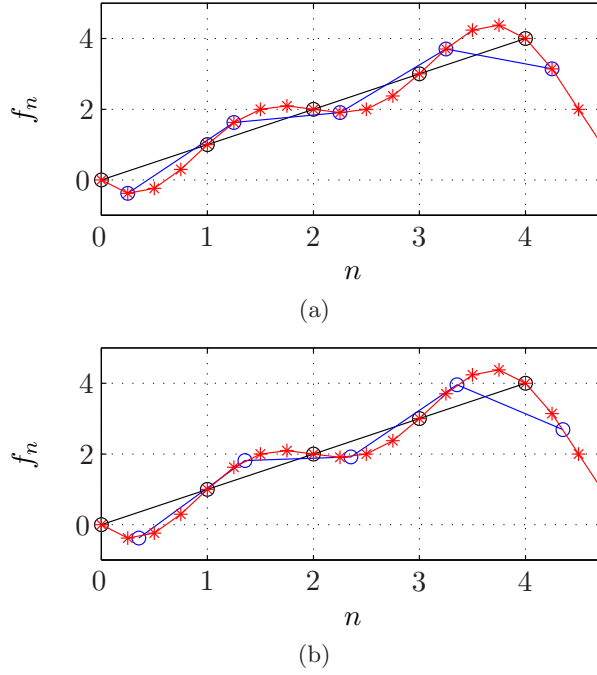


Figure C.1: Interpolation of a step function

and  $G_k$  is not Hermitian. This is solved by defining the value at the Nyquist number as the real part

$$G_{N/2}(\alpha) = \Re(e^{\pi i \alpha}) = \cos(\pi \alpha). \quad (\text{C.10})$$

The interpolation algorithm is to Fourier transform the data, multiply with the filter  $G_k(\alpha)$  and an inverse Fourier transform.

An example of this interpolation is given in Figure C.1(a), a signal  $f_n = n$  for  $n = 0, 1, 2, 3, 4$  is given (black curve), and the Fourier interpolated  $h_n$  for  $M = 4$  in red. The filtering is done with  $\alpha = 1/4$  these are shown in blue, the interpolated points hit the same as the points from the interpolation by filling in zeros, since  $M\alpha$  is an integer.

Choosing  $\alpha = \sqrt{2}/4$ , Figure C.1(b), results in another picture, the points naturally does not hit the red curve. Finding interpolated values for points where  $\alpha$  is irrational is one advantage of this filtering, these values can never be found by filling in zeros. The algorithm does not contain the heavy convolutions, as in the regular interpolation routines, just fast FFTs.

This algorithm can also be used for upsampling of functions, for example choosing  $\alpha = 1/2$  will give sampling between the original sampling points. An example of this is given in Figure C.2. Starting with the Hilbert transformation of a Ricker wavelet

$$s(t) = \mathcal{H}[r(t)], \quad (\text{C.11})$$

where

$$r(t) = -2\lambda(2\lambda t^2 - 1)e^{-\lambda t^2}, \quad (\text{C.12})$$

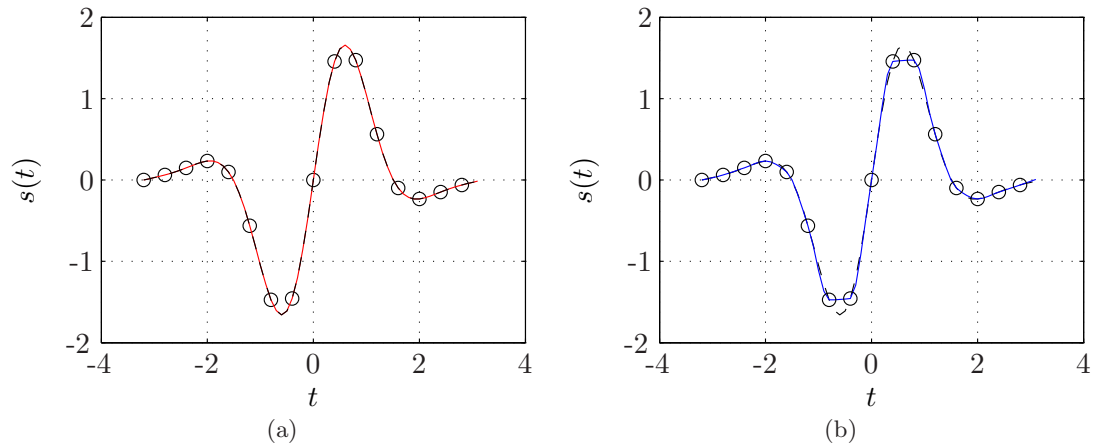


Figure C.2: Interpolation of the function  $s(t) = \mathcal{H}[r(t)]$ , where  $\lambda = 1$

The signal  $s(t)$  is sampled with  $\Delta t = 0.4$  and  $N = 16$  sampling points, represented by the black circles in Figure C.2(a). To upsample this function 4 times, new sampling interval  $\Delta t = 0.1$ , the filtering is calculated for  $\alpha = 1/4, 2/4, 3/4$ , red curve in Figure C.2(a). This interpolation is equivalent to filling in zeros  $M = 4$ . The same interpolation is done with MATLAB's implemented cubic spline, blue curve in Figure C.2(b). The black dashed curve in both figures are the signal  $s(t)$  sampled on the resulting points. Comparing with this the observation is that interpolation in Fourier domain gives better result than the one interpolated with cubic spline. This is probably due to the Ricker wavelet being an exponential function. This shows that when processing Fourier waves it would be preferable to do interpolation with the Fourier transform.

A MATLAB implementation of the filtering interpolation is given below.

### filterinterp.m

```

1 function [fint,nny] = filterinterp(f,alpha)
2 %Finds interpolated values in the points n + alpha, where 0 < alpha < 1
3 N = length(f);
4 n = 0:N-1;
5 nny = n + alpha;
6 m = mod(n + floor(N/2),N) - floor(N/2);
7 F = fft(f);
8 if floor(N/2) == ceil(N/2)%even sampling
9     J = exp(2*pi*1i*m*alpha/N);
10    J(N/2+1) = cos(pi*alpha);
11 else%odd sampling
12    J = exp(2*pi*1i*m*alpha/N);
13 end
14
15 fint = ifft(F.*J);
16 return

```



## C.2 Dirichlet Kernel

Using convolution it is possible to get interpolated values of a function  $f_n$  at sampling points  $t_n$  which are not necessarily equidistant. Defining a time sequence  $f_n \in \mathbb{R}$  for  $n = 0, 1, 2, \dots, 2N + 1$ , with Fourier domain  $F_k$  for  $k = -N, \dots, 0, \dots, N$ . The Fourier spectrum will be hermitian since  $f_n$  is real. The  $Z$  transformation gives

$$g(Z) = \sum_{k=-N}^N F_k Z^k, \quad (\text{C.13})$$

By defining  $E = \exp(-2\pi i/N)$  and Fourier Transforming

$$g(Z) = \frac{1}{N} \sum_{k=-N}^N \left[ \sum_{n=0}^{2N+1} f_n E^{nk} \right] Z^k, \quad (\text{C.14})$$

changing the order of summation

$$g(Z) = \frac{1}{N} \sum_{n=0}^{2N+1} f_n \left[ \sum_{k=-N}^N Z^k E^{nk} \right], \quad (\text{C.15})$$

the last sum is a geometric series and

$$g(Z) = \frac{1}{N} \sum_{n=0}^{2N+1} f_n \left[ (ZE^n)^{-N} \frac{1 - (ZE^n)^{2N+1}}{1 - ZE^n} \right]. \quad (\text{C.16})$$

Defining  $Z = \exp(2\pi t \Delta\omega)$  gives  $ZE^n = \exp(i2\pi(t - t_n)/T)$  for  $t_n = n\Delta t$  and  $\Delta\omega = 2\pi/T$ . This gives the cyclic convolution

$$g(t) = \sum_{n=0}^{2N+1} f_n w(t - t_n), \quad (\text{C.17})$$

where

$$w(t) = \frac{\sin(\pi(t)(2N + 1)/T)}{N \sin(\pi(t)/T)}, \quad (\text{C.18})$$

is the Dirichlet kernel, the discrete equivalent to cardinal sine, equation (C.1). This interpolation kernel is periodic which gives that the resulting time sequence  $g$  also is periodic. This will be an advantage when interpolating seismic waves. The interpolation result  $g(t)$  can now be evaluated in any discrete points  $t$ .

A MATLAB implementation of this is given below.

## direcletinterp.m

```
1 %direcletinterp Interpolation with the Direclet kernel.
2 %   f_new = direcletinterp(t,f,t_new,dt)
3 %   t - original time sampling
4 %   f - original function
5 %   t_new - new samplingpoints
6 %   dt - equidistant original sampling interval
7 function [f_new] = direcletinterp(t,f,t_new,dt)
8 N = length(t);
9 for n=1:length(t_new)
10     w = diric(2*pi*(t_new(n)-t)/(N*dt),N);
11     f_new(n) =sum(f.*w);
12 end
13 return
```

# Bibliography

- Bardan, V., 1989, Sampling two-dimensional seismic data and their Radon transforms: *Geophysics*, **54**, 1318.
- , 1997, A hexagonal sampling grid for 3D recording and processing of 3D seismic data: *Geophysical Prospecting*, **45**, 819–830.
- , 2008, The Petersen-Middleton theorem and sampling of seismic data: *Geophysical Prospecting*, **57**, 823–834.
- Baysal, E., D. Kosloff, and J. Sherwood, 1983, Reverse time migration: *Geophysics*, **48**, 1514–1524.
- Bernardini, R., and R. Manduchi, 1994, On the reduction of multidimensional DFT to separable DFT by Smith normal form theorem(discrete Fourier transform): *European Transactions on Telecommunications and Related Technologies*, **5**, 377–380.
- Berryhill, J. R., 1979, Wave-equation datuming: *Geophysics*, **44**, 1329–1344.
- Beylkin, G., 1987, Discrete Radon Transform: *IEEE Transactions on Acoustics Speech and Signal Processing*, **35**, 162–172.
- Chabert, J., 1999, *A history of algorithms: from the pebble to the microchip*: Springer.
- Chang, W., and G. McMechan, 1990, 3D acoustic prestack reverse-time migration: *Geophysical Prospecting*, **38**, 737–755.
- Deans, S., 1983, *The Radon transform and some applications*: John Wiley, New York.
- Du, X., J. Bancroft, and L. Lines, 2007, Anisotropic reverse-time migration for tilted TI media: *Geophysical Prospecting*, **55**, 853–870.
- Dudgeon, D., and R. Mersereau, 1990, *Multidimensional digital signal processing*: Prentice Hall Professional Technical Reference.
- Ehrhardt, J., 1993, Hexagonal fast Fourier transform with rectangular output: *IEEE Transactions on signal processing*, **41**, 1469–1472.
- Evans, B., R. Bamberger, and J. McClellan, 1994, Rules for multidimensional multirate structures: *IEEE Transactions on Signal Processing*, **42**, 762–771.
- Folland, G., 2009, *Fourier analysis and its applications*: AMS Bookstore.
- Fraleigh, J., 2003, *A first course in abstract algebra*: Addison-Wesley Reading, Mass.
- Gazdag, J., 1978, Wave equation migration with the phase-shift method: *Geophysics*, **43**, 1342.
- , 1980, Wave equation migration with the accurate space derivative method: *Geophys. Prosp.*, **28**, 60–70.
- , 1981, Modeling of the acoustic wave equation with transform methods.
- Gesbert, S., C. Haneveld, and S. Saleh, 2007, 3D” hexagonal” prestack depth migration of seismic data: *The Leading Edge*, **26**, 1262.
- Gilbert, W., 1993, *Bricklaying and the Hermite Normal Form*: American Mathematical

- Monthly, 242–245.
- Guessoum, A., and R. Mersereau, 1986, Fast algorithms for the multidimensional discrete Fourier transform: *IEEE Transactions on Acoustics, Speech and Signal Processing*, **34**, 937–943.
- Guizar-Sicairos, M., and J. Gutierrez-Vega, 2004, Two-dimensional Fourier transform of scaled Dirac delta curves: *Journal of the Optical Society of America A*, **21**, 1682–1688.
- Havas, G., and B. Majewski, 1997, Integer matrix diagonalization: *Journal of Symbolic Computation*, **24**, 399–408.
- Jain, A., 1989, *Fundamentals of digital image processing*: Prentice-Hall, Inc. Upper Saddle River, NJ, USA.
- Loewenthal, D., and I. Mufti, 1983, Reversed time migration in spatial frequency domain: *Geophysics*, **48**, 627.
- Maeland, E., 1988, On the comparison of interpolation methods: *IEEE transactions on medical imaging*, **7**, 213–217.
- , 1994, On the evaluation of explicit 2-D extrapolation operators: *Geophysical Journal International*, **116**, 85–94.
- McMechan, G., 1982, Determination of source parameters by wavefield extrapolation: *Geophysical Journal International*, **71**, 613–628.
- , 1983, Migration by extrapolation of time-dependent boundary values: *Geophysical Prospecting*, **31**, 413–420.
- Mersereau, R., 1979, The processing of hexagonally sampled two-dimensional signals: *Proceedings of the IEEE*, **67**, 930–949.
- Mersereau, R., and T. Speake, 1983, The processing of periodically sampled multidimensional signals: *IEEE Transactions on Acoustics, Speech and Signal Processing*, **31**, 188–194.
- Morandi, P. J., 2005, The smith normal form of a matrix. <http://sierra.nmsu.edu/morandi/notes/SmithNormalForm.pdf>.
- Murphy, P., and N. Gallagher, 1982, Hexagonal sampling techniques applied to Fourier and Fresnel digital holograms: *J. Opt. Soc. Am*, **72**, 929–937.
- Okabe, A., B. Boots, K. Sugihara, and S. Chiu, 2009, *Spatial tessellations: Concepts and applications of Voronoi diagrams (POD): européen des systèmes automatisés*, **43**.
- Rathey, P., and A. Lindgren, 1981, Sampling the 2-D Radon transform: *IEEE Transactions on Acoustics, Speech and Signal Processing*, **29**, 994–1002.
- Rayward-Smith, V., 1979, On computing the Smith normal form of an integer matrix: *ACM Transactions on Mathematical Software*, **5**, 451–456.
- Sandwell, D., 1987, Biharmonic spline interpolation of GEOS-3 and SEASAT altimeter data: *Geophysical Research Letters*, **14**, 139–142.
- Schultz, P., and J. Claerbout, 1978, Velocity estimation and downward continuation by wavefront synthesis: *Geophysics*, **43**, 691.
- Stolt, R., and A. Benson, 1986, *Seismic migration: Theory and practice*: Pergamon.
- Ville, D. V. D., W. Philips, and I. Lemahieu, 2002, Least-squares spline resampling to a hexagonal lattice: *Signal Processing: Image Communication*, **17**, 393 – 408.
- Woodward, M., 1986, Three-pass 3-d migration on a hexagonal grid: Stanford Exploration Project, SEP-50.
- Woodward, M., and F. Muir, 1984a, Hexagonal finite difference operators and 3-d wave equation migration: Stanford Exploration Project, SEP-38.
- , 1984b, Hexagonal sampling: Stanford Exploration Project, SEP-38.
- Yilmaz, O., and S. Doherty, 2001, *Seismic data analysis: Society of Exploration Geophysicists*

Tulsa.

Yilmaz, O., and M. T. Taner, 1994, Discrete plane-wave decomposition by least-mean-square-error method: *Geophysics*, **59**, 973–982.